1-1-2012

Factors Governing the Performance and Stability of Solid Oxide Fuel Cell Cathodes Prepared by Infiltration

Rainer Küngas
University of Pennsylvania, rainerkungas@gmail.com

Factors Governing the Performance and Stability of Solid Oxide Fuel Cell Cathodes Prepared by Infiltration

Abstract
Infiltration method, developed at the University of Pennsylvania, is a unique analytical platform for investigating the effect of material properties and electrode microstructure on the performance of solid oxide fuel cell (SOFC) electrodes. During cell fabrication by infiltration, the ion-conducting electrolyte phase is sintered first, followed by the addition of the catalytically active perovskite phase into the pores of the electrolyte. The use of separate sintering steps for the electrolyte and the active phase gives one a high degree of control over the microstructure of both phases, unattainable with traditional fabrication methods. In this thesis, the infiltration approach has been used to conduct a systematic investigation into the factors that govern the performance and stability of solid oxide fuel cell cathodes. As a result, a number of microstructural and material properties, crucial for obtaining high electrode activity, were identified. In particular, the effect of varying the ionic conductivity of the porous electrolyte, the specific surface area of the perovskite as well as the specific surface area of the porous electrolyte, and the effect of solid-state reactions between the two phases were studied and were found to significantly affect performance. The experimental findings agreed well with the predictions of a mathematical model that was developed to describe the electrochemical characteristics of SOFC composite cathodes.

Both theoretical and experimental evidence suggests the performance of SOFC cathodes prepared by infiltration is limited by slow oxygen adsorption on the perovskite surface. The chemical composition of the perovskite surface therefore plays an important role in determining the overall performance of the electrode. The last chapter of this thesis introduces a novel method that may allow one to characterize the active sites on the perovskite surface under SOFC cathode operating conditions (600-700Â°C, ambient air atmosphere, polarization), unattainable with traditional surface characterization techniques.

Degree Type
Dissertation

Degree Name
Doctor of Philosophy (PhD)

Graduate Group
Chemical and Biomolecular Engineering

First Advisor
Raymond J. Gorte

Second Advisor
John M. Vohs

Keywords
cathode, infiltration, microstructure, perovskite, solid oxide fuel cells, YSZ

FACTORS GOVERNING THE PERFORMANCE AND STABILITY OF SOLID OXIDE FUEL CELL CATHODES PREPARED BY INFILTRATION

Rainer Küngas

A DISSERTATION

in

Chemical and Biomolecular Engineering

Presented to the Faculties of the University of Pennsylvania

in Partial Fulfillment of the Requirements for the

Degree of Doctor of Philosophy

2012

Supervisor of Dissertation

_____

Raymond J. Gorte, Professor, CBE

Graduate Group Chairperson

Co-Supervisor of Dissertation

_____

John M. Vohs, Professor,CBE

_____

Raymond J. Gorte, Professor, Chemical and Biomolecular Engineering

Dissertation Committee

Daeyeon Lee, Assistant Professor, Chemical and Biomolecular Engineering

Steven J. May, Assistant Professor, Materials Science and Engineering, Drexel U.

To my parents

Acknowledgements

First, I would like to thank my advisor, prof. Ray Gorte, for his guidance throughout my studies. It is largely due to his teachings in the lab as well as in class that I learnt how to think like an engineer. I also wish to thank prof. John Vohs, my co-advisor, for helpful discussions and encouragement.

Life in graduate school would not have been the same without my colleagues and friends. I particularly wish to thank Lawrence for always being there for discussions, Kwadwo, for being my number one partner on the squash court, and Andrea, for introducing me the Philadelphia art scene. I am very grateful to Fred who taught me the techniques in the lab that I ended up using throughout my studies.

In addition, I wish to thank the Fulbright Science and Technology Award and the US Department of State for giving me the opportunity to spend time among some of the brightest brains on the planet.

Finally, I would like to thank my parents, my brother, and Annika for their continuous support over all these years.

ABSTRACT

FACTORS GOVERNING THE PERFORMANCE AND STABILITY OF SOLID OXIDE FUEL CELL CATHODES PREPARED BY INFILTRATION

Rainer Küngas

Raymond J. Gorte, John M. Vohs

Infiltration method, developed at the University of Pennsylvania, is a unique analytical platform for investigating the effect of material properties and electrode microstructure on the performance of solid oxide fuel cell (SOFC) electrodes. During cell fabrication by infiltration, the ion-conducting electrolyte phase is sintered first, followed by the addition of the catalytically active perovskite phase into the pores of the electrolyte. The use of separate sintering steps for the electrolyte and the active phase gives one a high degree of control over the microstructure of both phases, unattainable with traditional fabrication methods. In this thesis, the infiltration approach has been used to conduct a systematic investigation into the factors that govern the performance and stability of solid oxide fuel cell cathodes. As a result, a number of microstructural and material properties, crucial for obtaining high electrode activity, were identified. In particular, the effect of varying the ionic conductivity of the porous electrolyte, the specific surface area of the perovskite as well as the specific surface area of the porous

electrolyte, and the effect of solid-state reactions between the two phases were studied and were found to significantly affect performance. The experimental findings agreed well with the predictions of a mathematical model that was developed to describe the electrochemical characteristics of SOFC composite cathodes.

Both theoretical and experimental evidence suggests the performance of SOFC cathodes prepared by infiltration is limited by slow oxygen adsorption on the perovskite surface. The chemical composition of the perovskite surface therefore plays an important role in determining the overall performance of the electrode. The last chapter of this thesis introduces a novel method that may allow one to characterize the active sites on the perovskite surface under SOFC cathode operating conditions (600-700°C, ambient air atmosphere, polarization), unattainable with traditional surface characterization techniques.

Table of Contents

List of Tables

List of Figures

Chapter 1. Introduction

1.1 Motivation

In contrast to the tremendous pace of technological change in fields like computing, biotechnology and health care, the technology of power generation has remained largely unchanged over the last 50 years. Today, most of the electricity is still generated in large thermal power plants, where heat from the combustion of fuel is converted into mechanical energy, which is subsequently converted to electrical energy. In a typical power plant, almost ⅔ of the energy in the fuel remains unused and is lost as waste heat. Only an incremental 2% improvement in thermal power generation efficiency (from 32% to 34%) was achieved worldwide from 1990 to 2008 [1].

Rising environmental concerns have spurred the search and development of new, cleaner power generation technology. Fuel cells is one such technology. Unlike heat engines, fuel cells are able to convert chemical energy directly into electrical energy, and are therefore not constrained by the Carnot efficiency. As a result, fuel cells are generally significantly (10 to 20%) more efficient than combustion engines, even at very small system sizes.

Furthermore, for fuel cells operating at high temperatures (between 700°C and 1000°C), additional energy gain can be achieved by incorporating a steam turbine cycle to recover heat from the hot gas leaving the cell. The overall efficiency of such a combined heat and power (CHP) generation system can be as high as 75% [2]. High efficiencies lead to significant reductions in carbon dioxide emissions in comparison

with conventional systems. Due to low operating pressures, fuel cells deliver negligible NO_x and SO_x emissions. When hydrogen is used as fuel, power generation with zero (local) emissions is possible.

1.2 Solid Oxide Fuel Cells

All fuel cells consist of at least three components: the anode, the cathode and the electrolyte. Electrochemically, the anode facilitates the oxidation of fuel, while the cathode catalyzes the reduction of an oxidizing species (typically oxygen in the form of air). Direct combustion of the fuel is prevented by separating the two electrodes by an electrolyte membrane that is impermeable to gases and electronic current, but allows for ionic transport from one electrode to the other (Fig. 1.1).

A number of different fuel cell types have been developed based on various material systems. Typically, the operating temperature and general properties of a fuel cell are determined by the chemical nature of the electrolyte material used. Accordingly, polymer electrolyte membrane fuel cells (PEMFCs) employ electrolytes that consist of hydrated proton-conducting polymers, which limit their operation to below 100°C. Solid oxide fuel cells (SOFCs), where ceramic materials are used as electrolytes, lie at the other end of the temperature spectrum, and operate typically at temperatures above 600°C. Many other fuel cell systems, such as alkaline fuel cells (AFCs), phosphoric acid fuel cells (PAFCs), and molten carbonate fuel cells (MCFCs) exist and are being commercialized [2,3].

An SOFC is an all-solid-state energy conversion device that produces electricity by electrochemically combining fuel and oxidant gases across an ionically conducting ceramic membrane. An SOFC consists of two electrodes (the anode and the cathode) separated by a solid electrolyte (Fig. 1.1). Oxidant (air) is fed to the cathode where it is electrochemically reduced by electrons from the external circuit:

$$O_2(g) + 4e^- \rightarrow 2O^{2-}. \qquad \text{Equation 1.1}$$

Fuel (H_2, CO, CH_4, etc.) is fed to the anode, where it undergoes an oxidation reaction and releases electrons to the external circuit:

$$H_2(g) + O^{2-} \rightarrow H_2O\,(g) + 2e^-, \qquad \text{Equation 1.2}$$

$$CO(g) + O^{2-} \rightarrow CO_2\,(g) + 2e^-, \qquad \text{Equation 1.3}$$

or, in the case of hydrocarbon fuels,

$$C_nH_{2n+2} + (3n+1)\,O^{2-} \rightarrow n\,CO_2\,(g) + (n+1)\,H_2O + 2\cdot(3n+1)\,e^-. \qquad \text{Equation 1.4}$$

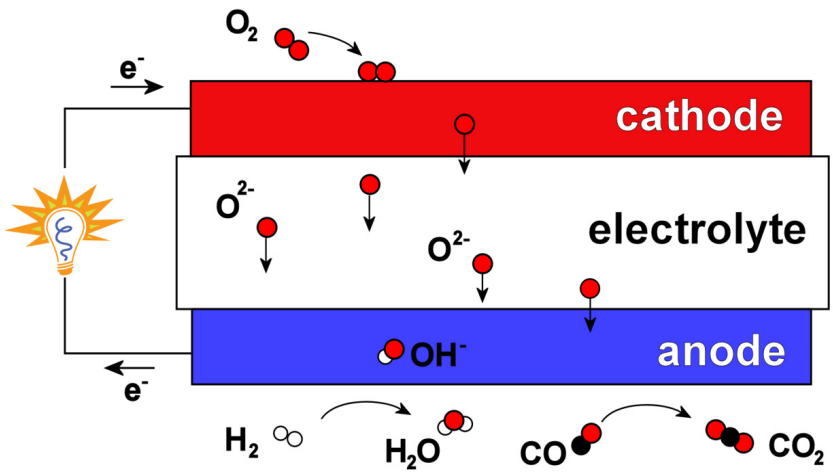

Figure 1.1 The operating principle of a solid oxide fuel cell.

When a constant flow of reactants is maintained to the electrodes, the SOFC generates direct electronic current from the anode to the cathode, which can be used to drive an external load. Multiple SOFC units can be connected in series in order to increase the voltage and power output of the system.

The key advantage of SOFCs over other types of fuel cells lies in their inherent fuel flexibility. In low-temperature fuel cells (PEMFC, AFC, PAFC), the fuel fed into the system is the source of the ionic charge carriers (either H^+ or OH^-). This and susceptibility to poisoning (CO and sulfur poisoning in PEMFCs and PAFCs, CO_2 poisoning in AFCs) severely limits the number of fuels suitable for long-term operation. In all cases, the use of highly pure H_2 is the preferred, although operation on methanol is possible in some PEMFCs [3].

In SOFCs, ionic charge carriers (O^{2-} anions) originate from air and the reaction between O^{2-} and the fuel occurs on the anode side of the electrolyte. In contrast to PEMFCs, where even ppm levels of CO in the fuel dramatically affect performance, SOFCs can operate with 100% CO or syngas as fuel [2-4]. Furthermore, the high operating temperatures of SOFCs allow for internal reforming of hydrocarbon fuels, such as methane, natural gas, landfill gas, etc [2-6]. In prior work from the University of Pennsylvania, researchers have demonstrated stable SOFC operation on liquid fuels such as ethane, 1-butene, n-butane, toluene [7], and even on diesel [8,9]. Recently, SOFCs utilizing solid fuels, such as carbon, coal, and pyrolyzed biomass have been developed [10,11].

1.3 Traditional SOFC materials

The first generation of SOFCs operated at temperatures close to 1000°C [2,4,12,13]. Typically, these cells employed a fairly thick dense electrolyte, which acted as a mechanical support for the electrodes (Fig. 1.2a). Due to its chemical stability and relatively high oxygen ion conductivity, almost all of these devices employed yttria-stabilized zirconia (YSZ) as the electrolyte. A cermet of Ni and YSZ (in some early examples, metallic Pt) was used as the anode material, while a perovskite ceramic, Sr-doped $LaMnO_3$ (LSM) was used almost exclusively as the cathode material [2,4,12-14].

1.3.1 Yttria-stabilized zirconia

Pure ZrO_2 is an insulator with a dielectric constant of 25 [15]. Upon doping with trivalent metal oxides (e.g. Y_2O_3), oxygen vacancies (one per every two Y^{3+} ions) are formed in the ZrO_2 lattice. At high temperatures, these vacancies become mobile and can hop from one lattice site to the next, giving rise to oxygen ion conductivity in the material. At low doping levels (less than 8 mol% Y_2O_3 in ZrO_2), the ionically conducting cubic phase is not stable at SOFC operating temperatures. For example, for pure ZrO_2, cubic phase only exists above 2340°C [16]. Between 1170°C and 1700°C, ZrO_2 exists in tetragonal phase, and transforms into monoclinic phase below 1170°C [16]. Such phase transitions are undesirable as they are accompanied by changes in material dimensions (the volume change associated with the tetragonal to monoclinic phase transformation is 3-5 vol% [4,16]), which can result in large mechanical stresses in the system and ultimately lead to cell failure.

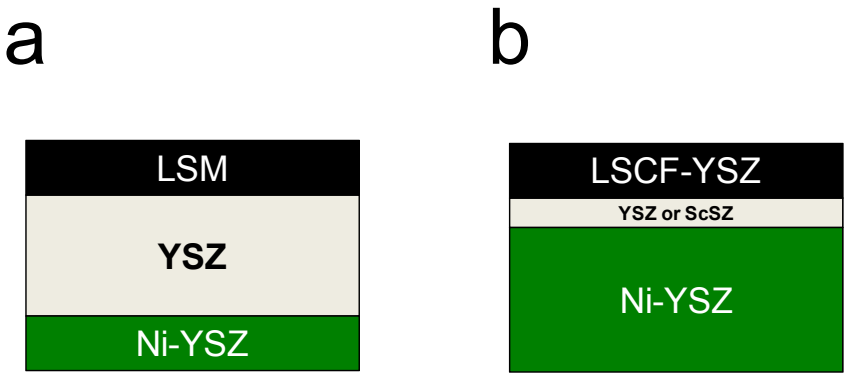

Figure 1.2 Schematic representations of a) an electrolyte-supported high-temperature SOFC ('first-generation SOFC'), b) an anode-supported intermediate temperature SOFC ('second-generation SOFC'). LSM – Sr-doped $LaMnO_3$, YSZ – yttria-stabilized zirconia, ScSZ – scandia-stabilized zirconia, LSCF – Sr-doped $LaCo_yFe_{1-y}O_3$.

At high doping levels (9 mol% Y_2O_3 or more), increased defect concentration leads to electrostatic interactions between the vacancies and the dopants, resulting in a reduction in oxygen ion mobility [3,4]. A composition of 8 mol% Y_2O_3 in ZrO_2, sometimes abbreviated as 8YSZ, is therefore almost always used, because it offers both maximum ionic conductivity (0.01 S/cm at 1000°C [4]) as well as phase stability over the entire range of SOFC operating and manufacturing temperatures. However, it should be noted that the mechanical strength of YSZ decreases with increasing Y^{3+} doping, which is the reason why some SOFC manufacturers have chosen to base their cell design on partially stabilized YSZ instead [2,4]. Importantly, the electronic conductivity of YSZ is negligible: the electronic transference number (the probability that a charge carrier transported through the material is an electron, not an ion) has a value of 10^{-8} … 10^{-9} over a wide range of oxygen partial pressures [4,17].

1.3.2 Ni/YSZ

Metallic nickel is a good catalyst for methane steam reforming. It also serves as a good hydrogen oxidation catalyst and provides electronic pathways from the reaction zone to the external circuit. It has been established that the anode reaction occurs preferentially at the three-phase boundary (TPB) sites, where an electronic conductor (Ni), an oxygen-ion conductor (YSZ) and gaseous fuel are all present at the same time [2-4,18-21]. To maximize the number of TPB sites, the particle size of Ni in the electrode active layer should be as small as possible. Unfortunately, Ni nanoparticles undergo rapid coarsening at SOFC temperatures due to Ostwald ripening [22]. Ni/YSZ anodes are also very sensitive to impurities in the fuel (S, As, Sb, Cl, etc) [23-26] and degrade catastrophically when subject to oxidation / re-reduction (redox) cycles [27,28]. Ni nanoparticles are the catalyst of choice for carbon nanotube synthesis [29-31]. Unfortunately, this also means that SOFCs with Ni anodes must be operated at high steam to carbon ratios to avoid cell failure due to coking [32].

1.3.3 Sr-doped $LaMnO_3$

Sr-doped $LaMnO_3$ ($La_{1-x}Sr_xMnO_3$, LSM) has a perovskite structure (the structure and properties of perovskite materials will be discussed in more detail in Chapter 1.5). It is the most commonly used cathode material for high-temperature SOFCs due to its good physical and chemical compatibility with YSZ (no solid-state reactions up to 1200°C [4,32]), high electronic conductivity (~300 S/cm at 1000°C [3,4]) and activity towards the oxygen reduction reaction [3,4,33,34]. The ionic conductivity of LSM is very low

($4 \cdot 10^{-8}$ S/cm at 800°C [34]), therefore composites with YSZ must be used to increase the number of TPBs and extend the electrode active region from the immediate vicinity of the cathode|electrolyte interface to the bulk of the electrode.

1.3.4 Current collector materials

The standard potential of the methane oxidation reaction is 1.04 V at 1000°C [35]. In order to achieve higher output voltage, several SOFC single cells (membrane-electrode assemblies) must be connected in series. The electrical connection between the anode and the cathode is made by using interconnects. The interconnect materials must be stable (and electronically conducting) at high temperatures in both oxidizing and in reducing environments (in the presence of steam). At 1000°C, only ceramic conductors, such as Ca- or Sr-doped $LaCrO_3$, are able to maintain conductivity over the required $p(O_2)$ range [2-4]. However, $LaCrO_3$-based materials are difficult to sinter to full density, making the fabrication very expensive.

1.4 State-of-the-art

In the mid-1990s, in an attempt to drive down materials and cell fabrication costs, the attention of the SOFC community shifted from developing high-temperature systems to lowering the operating temperature of SOFCs [36]. Temperature reduction from 1000°C to between 600°C and 800°C greatly enhances the long-term stability of SOFC systems, as the rates of electrochemical corrosion and material interdiffusion decrease exponentially with temperature. Equally importantly, lower operating temperatures allow

cheaper materials, such as various stainless steels, to be employed as interconnect materials. The issue of finding suitable sealing materials also becomes less severe as fewer restrictions are imposed on the thermal expansion match between different components of the cell [37].

At 1000°C, the ohmic resistance associated with a 100-μm 8YSZ electrolyte is approximately 0.1 Ω cm^2 [4,38]. In order to achieve the same resistance at 700°C, the thickness of the electrolyte must be decreased to just 18 μm [38]. Such thin electrolyte layers do not possess enough mechanical strength to support the electrodes; therefore an electrode-supported (typically anode-supported) cell configuration (Fig. 1.2b) must be employed. Other, more conducting electrolytes, such as Sc_2O_3-stabilized ZrO_2 (ScSZ) and various doped CeO_2 materials (e.g. Sm-doped CeO_2, SDC) may be used instead of YSZ to reduce ohmic losses [38-40].

Despite its several shortcomings, Ni is still the most commonly used active material for SOFC anodes. However, a number of conducting ceramic anode materials, such as La-doped $SrTiO_3$ (LST) [41,42], Sr-doped $LaCr_{0.5}Mn_{0.5}O_3$ (LSCM) [41,43-45], Sr-doped rare-earth vanadates [46,47], and various tungsten bronzes [41,48] have been proposed as promising alternatives to Ni. Ceramic anodes are thermally more stable and exhibit potentially better tolerance towards sulfur and redox cycling. To the author's knowledge, none of these materials are used in commercial SOFC systems today, but it is likely that this will change in the future.

As the operating temperature of SOFCs is reduced and the sources of other losses minimized (e.g. by decreasing the thickness of the solid electrolyte), the cathode

contribution to the overall impedance becomes increasingly important [49]. In one example, reducing the operating temperature of an SOFC from 1000°C to 500°C increased the polarization resistance of an LSM-based cathode from <1 Ω cm^2 to 2000 Ω cm^2 [14]. Cathodes with increased activity towards oxygen reduction reaction must therefore be developed. Activity can be tailored by 1) altering the physical properties of electrode materials (Chapter 1.5) or 2) by changing the microstructure of the electrodes (Chapter 1.6).

The aim of this thesis is to elucidate the relative importance of both various physical properties (ionic and electronic conductivity, perovskite surface composition, etc.) as well as microstructural properties (specific surface area, perovskite particle size) on the performance of composite cathodes for SOFCs operating between 600°C and 800°C. All experiments presented here have been performed on electrodes prepared by infiltration (see Chapter 1.6), a cell fabrication technique that allows for very precise control of the microstructure of each component in an electrode [49].

The author hopes that the systematic approach taken here will help to identify the key factors that are currently limiting the performance in the state-of-the-art SOFC systems, and that based on the conclusions of this work, future investigators will be able to directly address these most critical problems. Through the development of better and more stable SOFC cathodes, the ultimate goal of SOFC research – the widespread adoption of the technology – may become a reality.

1.5 Perovskite cathode materials

Perovskite oxide materials with a general formula ABO_3, containing La and Sr on the A-site and transition metals on the B-site, are important materials for SOFC cathodes. Most SOFC cathodes are based on Sr-doped lanthanum manganites, cobaltites, or ferrites, i.e. materials like Sr-doped $LaMnO_3$ (LSM), Sr-doped $LaCoO_3$ (LSCo), Sr-doped $LaFeO_3$ (LSF), or Sr-doped $LaCo_{1-y}Fe_yO_3$ (LSCF) [49].

The example of Sr-doped $LaFeO_3$ ($La_{1-x}Sr_xFeO_{3-\delta}$, LSF) is used here to illustrate the effect of A-site doping on the properties of $LaFeO_3$ (Fig. 1.3). Stoichiometric $LaFeO_3$ (Fig. 1.3a) is a relatively poor electronic conductor (0.4 S/cm at 700°C in air) with negligible ionic conductivity [50]. The oxygen atoms in the perovskite structure surround the B-site cation in the shape of an octahedron. Upon Sr-doping, some of the La^{3+} on the A-site of the $LaFeO_3$ lattice is substituted with divalent Sr^{2+}.

The defect equilibrium is established through two processes: 1) by the oxidation of Fe^{3+} on the B-site to Fe^{4+}, 2) by the creation of oxygen vacancies, V_O^{2-}, one per every two Sr^{2+} atoms (Fig. 1.3b). Note: only a simplified picture is given here, a more rigorous approach employing Kröger-Vink notations can be found in [51]. Combining the results of the two reactions above, the doping process can be summarized as:

$$LaFeO_3 \xrightarrow{SrO} La^{3+}_{1-x}Sr^{2+}_x Fe^{3+}_{(1-x)+2\delta} Fe^{4+}_{x-2\delta} O_{3-\delta}, \qquad \text{Equation 1.5}$$

where x is the Sr-doping level and δ is the oxygen non-stoichiometry.

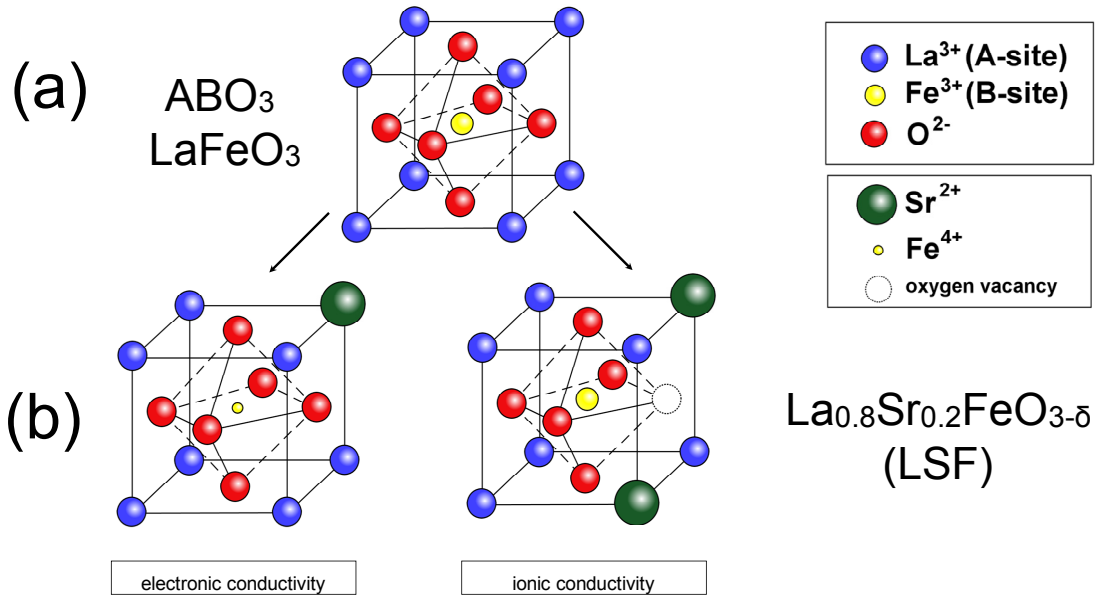

Figure 1.3 The unit cell of a) undoped $LaFeO_3$ with a perovskite structure, and b) Sr-doped $LaFeO_3$.

The oxidation of Fe^{3+} to Fe^{4+} increases the electronic conductivity of the LSF through the creation of Fe^{3+}-O-Fe^{4+} bridges [52], while the creation of oxygen vacancies in the lattice results in O^{2-} ion conductivity. Just 1 mol% of Sr doping increases the electronic conductivity to 2 S/cm [50], while the electronic conductivity of 20 mol% Sr-substituted $LaFeO_3$ (i.e. $La_{0.8}Sr_{0.2}FeO_3$) is ~80 S/cm at 700°C in air [51]. Additionally, $La_{0.8}Sr_{0.2}FeO_3$ also possesses significant levels of ionic conductivity (~$1.5 \cdot 10^{-4}$ S/cm at 700°C in air) [53].

In contrast to LSM, LSF is therefore a mixed ionic and electronic conductor (MIEC). In cathodes based on MIECs, oxygen adsorption and reduction is no longer spatially confined to the immediate vicinity of the TPB sites, but extends into the perovskite bulk [3,49,54,55]. This results in a significant increase in the effective active surface area of the electrode. However, the ionic conductivity of MIECs is usually still much lower than that of YSZ ($\sigma_{i,YSZ} = 1.8 \cdot 10^{-2}$ S/cm at 700°C [38]). Therefore, using a composite of an MIEC perovskite and YSZ (or another electrolyte material) can significantly improve the performance of SOFC cathodes compared to using the perovskite alone [56]. Electrodes based on MIEC-YSZ composites demonstrate excellent activity towards the oxygen reduction reaction even at temperatures 600…800°C (Fig. 1.2b). For example, the non-ohmic impedance associated with a $La_{0.8}Sr_{0.2}CoO_3$ (LSCo)-YSZ composite electrode prepared by infiltration is about 30 mΩ cm^2 at 700°C (see Chapter 5).

The thickness of the electrochemically active region can be estimated from mathematical models, such as the one proposed by Bidrawn, Küngas *et al.* [57]. The

model assumes that the structure of an SOFC composite cathode can be approximated to an array of uniform YSZ fins, covered with a thin perovskite film (e.g. LSM, LSF, or LSCo). According to the model, 90% of the electrochemical activity in an LSF-YSZ composite electrode, operating at 700°C with a non-ohmic impedance of 0.3 Ω cm^2, is confined to the first 7 μm of the electrode [57], while a typical electrode is about 50 μm in thickness. An LSCo-YSZ electrode operating at the same temperature has an active region thickness of about 70 μm. A more detailed description of the model will be given in Chapter 4.

1.6 The effect of microstructure

It is generally accepted that the performance of a fuel cell is determined to a high degree by the microstructure of the electrodes. For example, in a 1995 study, Østergård *et al*. demonstrated that the non-ohmic impedance of pure LSM cathodes could be decreased from 19.8 Ω cm^2 to 7.5 Ω cm^2 (at 1000°C) as the coarse-grained LSM starting powder was changed for a more finely grained powder [56]. A further two- to three-fold decrease in impedance was observed when some YSZ powder was added to the LSM prior to cell fabrication, effectively increasing the number of TPB sites in the cathode [56].

In the study by Østergård *et al*., LSM-YSZ cathodes were prepared using the traditional methods for electrode manufacture. In this approach, a mixture of LSM and YSZ is screen-printed onto a dense YSZ substrate and fired to 1200…1300°C. This temperature is a compromise, high enough to form good ion-conducting channels (by

sintering the YSZ particles in the electrode to the electrolyte) but low enough to avoid excessive coarsening of the perovskite and prevent solid-state reactions between the perovskite and the YSZ [49].

An alternative method of cell fabrication, called infiltration, has been developed at the University of Pennsylvania [7,33,40,47-49,58-62]. In this approach, slurries consisting of the YSZ powder, a polymeric binder, dispersant, plasticizers, and solvent are tape-cast (Fig. 1.4) to form the green YSZ dense film. When graphite or other carbonaceous pore formers are added to the slurry, green porous YSZ tapes can be cast [63]. The tapes are then laminated together and fired to 1500°C to form a porous-dense-porous YSZ structure. Electrode active materials can subsequently be added into the pores of the electrode by infiltrating the YSZ structure with nitrate solutions. For example, in order to infiltrate $La_{0.8}Sr_{0.2}FeO_3$, a solution of $La(NO_3)_3 \cdot 6H_2O$, $Sr(NO_3)_2$, and $Fe(NO_3)_3 \cdot 9H_2O$ at a molar ratio of La : Sr : Fe = 0.8 : 0.2 : 1 should be used. Citric acid or other chelating agents are normally also added to the solution in a 1:1 ratio to the metal cations in order to assist the formation of the perovskite phase at lower temperatures [64,65]. Upon heating to 700°C…850°C, the nitrates decompose to form the desired perovskite phase.

Composites prepared by infiltration have a number of advantages over composites prepared using the traditional method. First, the sintering temperature for the YSZ component of the composite can be much higher than the sintering temperature used for the perovskite. Because the porous YSZ scaffold is sintered to the electrolyte at very high temperatures, the ion-conducting channels from the electrolyte into the

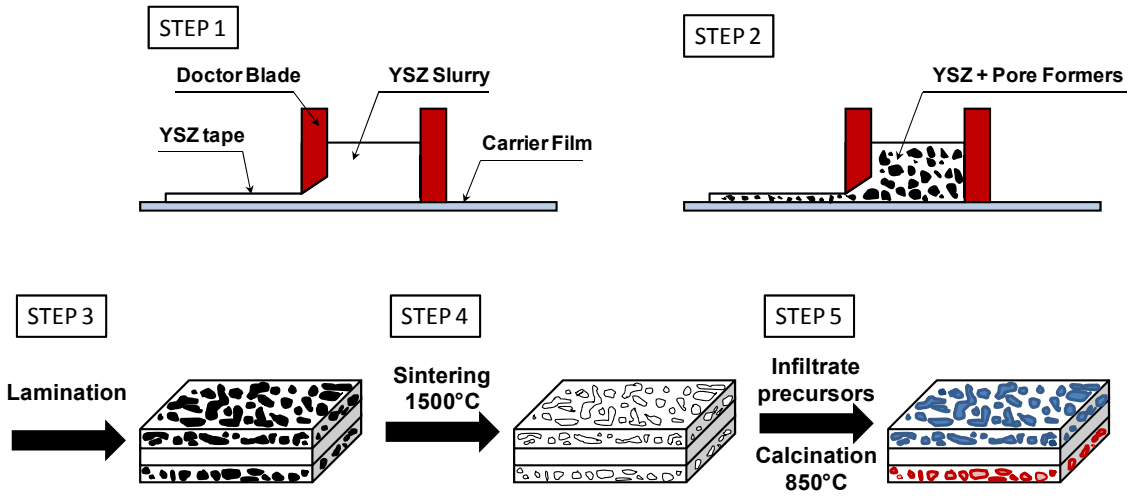

Figure 1.4 Cell fabrication by tape-casting and infiltration.

electrode are well established and delamination of electrodes is typically not a problem. The fact that the two sintering steps are separated in time allows for precise control of both the microstructure of the electrolyte scaffold and that of the active phase – a property of the infiltration method that will be used extensively throughout this thesis.

Secondly, because the conducting phase is added into an existing YSZ scaffold, the composites formed by infiltration are not random. One implication of this is that sufficient conductivity can be achieved using perovskite loadings below the normal percolation threshold of 30-vol% [49,58]. The non-random structure also causes the coefficient of thermal expansion (CTE) of the composite to be closer to that of YSZ scaffold than to the weighted average of the components [49,59].

Compared to the traditional approach, the electrode active materials do not normally have to be subjected to temperatures >850°C during electrode preparation by infiltration. At these relatively low temperatures, solid-state reactions between the YSZ and the perovskite are rarely an issue (an important exception here is the LSCo-YSZ system, which will be discussed in Chapter 5). This means that a large number of materials that were considered unsuitable for SOFC applications due to their reactivity with YSZ at temperatures employed in traditional SOFC manufacturing process, can be used as electrode materials when the infiltration approach is employed for cell fabrication [7-9,46-49,61,65].

Huang *et al*. demonstrated that LSM-YSZ electrodes, which are normally operated at 1000°C to achieve sufficient activity towards the oxygen reduction reaction, can be operated at 700°C with an acceptable non-ohmic impedance of 0.45 Ω cm^2 in air,

if the electrodes are prepared by infiltration [33]. However, a tenfold increase in impedance was observed when the nanoparticulate LSM phase was heated to 1100°C [33]. The effect of the surface area of the porous electrolyte scaffold will be discussed in more detail in Chapter 3, while Chapter 4 will examine the effect of changing the surface area and particle size of the perovskite.

1.7. Surface exchange versus bulk diffusion limitation

Mixed ionic and electronic conducting perovskites (such as LSF, LSCo, LSCF) are commonly used SOFC cathode materials. The rate of oxygen transport in these materials is governed by the kinetics of oxygen exchange on the perovskite surface and by the kinetics of oxygen anion diffusion in the perovskite bulk [66-71]. In ion-conducting membrane systems, the relative importance of the two processes is determined by the thickness. For thick membranes, oxygen transport is dominated by diffusion, and the overall rate depends on the value of the diffusion coefficient, D (cm^2/s), of O^{2-} ions in the perovskite. As the thickness of the membrane is decreased, transport rates become increasingly dependent on the rate of oxygen incorporation on the perovskite surface, a process which is characterized by the surface exchange coefficient, k (cm/s) [66,67,69].

The critical thicknesses, L_c, defined as $L_c = D/k$, for perovskite materials that are being considered for SOFC and ion-transport membrane (ITM) applications, lie between 30 μm and 300 μm at 700°C [69]. In SOFC cathodes, the characteristic length scale for

the perovskite phase is usually less than 1 μm [49,57,64], suggesting that oxygen transport in these systems should be limited by *k* (the surface), rather than *D* (the bulk).

It is perhaps not surprising then that a growing number of research groups have recently been converging on the idea that the kinetics of oxygen reduction on SOFC cathodes are limited by the availability of reaction sites on the perovskite surface. For example, Endo *et al.* showed that for dense $La_{0.6}Sr_{0.4}CoO_3$ (LSCo) electrodes deposited on Sm-doped ceria, electrochemical resistance exhibited no dependence on the thickness of the perovskite film, indicating surface limitation, while the impedance of dense $La_{0.81}Sr_{0.19}MnO_3$ (LSM) electrodes was inversely proportional to film thickness, indicating diffusion limitation [72]. A different approach was taken by Boukamp *et al.*, who showed that the addition of a thin dense layer of $La_{0.6}Sr_{0.4}Co_{0.2}Fe_{0.8}O_{3-\delta}$ (LSCF) between the electrolyte and porous LSCF electrode can significantly *improve* performance – a clear sign that diffusion through thin perovskite layers is facile under SOFC cathode operating conditions [73]. Adler found that the impedance response of low surface area LSCo electrodes on doped CeO_2 substrate was semicircular and followed the predictions of a model that assumed surface exchange limitation. High surface area LSCo electrodes were found to be co-limited by oxygen chemical exchange and transport [74].

Very elegant work demonstrating the importance of oxygen surface exchange has been done by Maier *et al*. [75], who observed a correlation between oxygen exchange coefficients and bulk oxygen vacancy concentration for a series of doped strontium ferrate materials. This phenomenon is demonstrated in Figure 1.5.

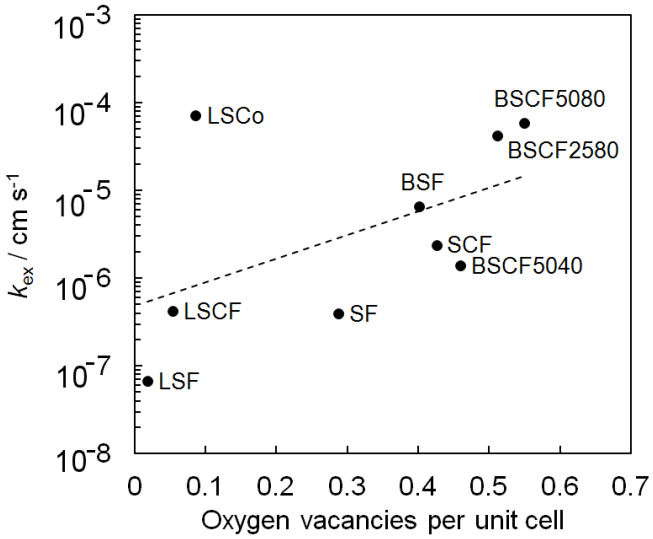

Figure 1.5 Effective oxygen exchange rate constant k at 700°C, $p(O_2)$ = 0.2 bar, measured on thin film electrodes with different compositions, plotted as a function of the bulk oxygen vacancy concentration. Data compiled from [75] $Ba_{0.5}Sr_{0.5}FeO_{3-\delta}$ (BSF), $SrCo_{0.8}Fe_{0.2}O_{3-\delta}$ (SCF), $Ba_{0.5}Sr_{0.5}Co_{0.4}Fe_{0.6}O_{3-\delta}$ (BSCF5040), $Ba_{0.25}Sr_{0.75}Co_{0.8}Fe_{0.2}O_{3-\delta}$ (BSCF2580), $Ba_{0.5}Sr_{0.5}Co_{0.8}Fe_{0.2}O_{3-\delta}$ (BSCF5080), [76] $SrFeO_{3-\delta}$ (SF), [66] $(La_{0.6}Sr_{0.4})_{0.99}FeO_{3-\delta}$ (LSF), [77,78] $La_{0.6}Sr_{0.4}Co_{0.8}Fe_{0.2}O_{3-\delta}$ (LSCF), [78,79] $La_{0.6}Sr_{0.4}CoO_{3-\delta}$ (LSCo).

In addition to the impedance spectroscopy studies above, a variety of other experimental techniques seem to point toward similar conclusions. In the electrical conductivity relaxation (ECR) method, the changes in the conductivity of the sample are measured as a function of time, in response to a step change in oxygen partial pressure [66,80-82]. Using this method, Mosleh *et al*. recently proposed that the vacancies are the active sites of adsorption of molecular oxygen in Sr-doped $LaFeO_3$ thin films and that the rate determining step for the exchange reaction is splitting of the adsorbed oxygen [66]. While inherently a very simple technique, obtaining meaningful results is non-trivial with ECR, as has been demonstrated in e.g. Ref. 82.

Interesting work using oxygen isotope exchange from the groups of Wachsman and Bouwmeester also suggests oxygen exchange is rate-limiting [67,83,84]. In one example, the atmosphere surrounding an LSCF sample was switched from $^{16}O_2$ to $^{18}O_2$ [83]. A lag in the production of the scrambled product, $^{16}O^{18}O$, assumed to occur only on the sample surface, was observed, demonstrating that the labeled oxygen does not displace the original surface species right away, but must gradually accumulate, consistent with a hypothesis of slow surface exchange and fast diffusion [83].

Secondary Ion Mass Spectrometry (SIMS) is another well-established experimental technique for studying oxygen surface exchange [70,71,85-87]. The values of k^* and D^* obtained from a SIMS experiment describe the rate of isotope exchange and diffusion in the sample, and are not equivalent to the values of k and D from ECR and isotope exchange experiments. Using the data obtained by SIMS, Kilner *et al*. drew attention to the remarkable correlation $k^* \sim (D^*)^{0.5}$ over a wide range of perovskite structures, and hypothesized that both parameters intrinsically depend on the vacancy concentration in the perovskite [71]. In fact, using SIMS, Yasuda *et al*. obtained a result very similar to that in Figure 1.5 for Ca-doped $LaCrO_{3-\delta}$ [87].

Recent findings reported by the University of Pennsylvania group complement in many ways the results presented above. Surface exchange limitation implies that maximizing the ionic conductivity of the perovskite in the SOFC composite cathode may not be necessary, as long as the conductivity exceeds a certain threshold value. The validity of this claim has been verified experimentally for differently doped $LaFeO_3$-YSZ cathodes prepared by infiltration in Ref. 88. Bidrawn *et al*. demonstrated that

cathodes infiltrated with Sr-, Ca-, or Ba-doped $LaFeO_3$ exhibited very similar impedance responses irrespective of the fact that the ionic conductivity of these materials differs by a factor of 60 [88]. In good agreement with the hypothesis of surface area limitation, the electrode performance has been found to be a strong function of the microstructure of the perovskite phase [33,53,59-62,88,89].

In case the surface reaction is rate-limiting, increasing the surface area of the electrode (e.g. by infiltration of nanoparticles) should result in enhanced performance. In Ref. 89, Bidrawn *et al*. added different species, such as YSZ, Pd, Sm-doped CeO_2, CaO, or K_2O into either LSF-YSZ or LSM-YSZ composite electrodes prepared by infiltration. Little or no change in electrode performance was observed when the additional species were infiltrated to electrodes that already had a relatively high surface area (1.8 m^2/g). In contrast, significant reduction in impedance values was observed when the same species were infiltrated into low-surface area (0.3 m^2/g) electrodes, regardless of the chemical nature of the dopant [89]. Intuitively, the effect of CaO on the catalytic, electronic, or ionic-conduction properties of the electrode should be minimal, while K_2O should have an outright negative effect. Surprisingly, both species were found to improve performance instead, suggesting that the lack of (purely geometric) surface area may be the rate-limiting factor for oxygen reduction [89].

A recently developed model of SOFC cathode performance, in which the O_2 adsorption rate was treated as proportional to the surface flux of O_2 from the kinetic theory of gases, the equilibrium oxygen vacancy concentration, and a sticking coefficient for dissociative adsorption onto these vacancy sites, provides additional support to the

hypothesis of surface area limitation [57]. The model was able to achieve a good match with experimental impedances using a reasonable value of the sticking coefficient onto the vacancy sites of 10^{-3} at 700°C. When diffusion-limitation was used as the rate-limiting step in the model, only very poor agreement with experimental results could be obtained [57].

Another implication of surface exchange limitation is that the chemical composition of the perovskite surface is likely to play an important role in determining the overall performance of the fuel cell. From a practical point of view, identifying the chemical nature and concentration of catalytically active sites on perovskite surfaces thus becomes highly important. Probing perovskite surfaces under operating conditions with surface-sensitive techniques (e.g. XPS) is very difficult due to the high temperatures and oxygen partial pressures involved.

An entirely different approach is presented in Chapter 6 of this thesis. It will be demonstrated how the activity of a perovskite surface can be modified through a conformal oxide coating prepared by atomic layer deposition (ALD). ALD is a sequential chemical vapor deposition (CVD) technique where evaporated precursors are alternatively pulsed into the deposition chamber, allowing the deposition of one atomic layer after another of conformal, homogeneous (sub-)nanometer thin films [90-93]. In contrast to traditional CVD, reactions in ALD are self-terminating, i.e. once the precursor has reacted with the substrate surface, further deposition is impossible. The self-terminating nature of ALD provides an exceptionally high level of control over the

thickness of the deposited layers, even when deposition is carried out in a porous medium [93].

Al_2O_3 deposition with trimethyl-aluminum (TMA) and water is probably the most well-known and thoroughly characterized ALD process [86,93]. The steps involved in the TMA-water deposition process are shown schematically in Fig. 1.6. First, the substrate (e.g. a perovskite surface) is subjected to a pulse of the alumina precursor, TMA. TMA reacts with the hydroxyl groups on the substrate surface, until all accessible hydroxyl groups have been consumed. The methyl-terminated groups on the substrate surface prevent further reaction (the reaction has reached self-termination) (Fig. 1.6, step 3). Upon the introduction of water, the surface methyl groups react to form methane and create new hydroxyl groups on the alumina surface. This proceeds until the entire surface has been oxidized (Fig. 1.6, step 6). The ALD cycle is repeated until an alumina layer with a desired thickness is achieved. Details about the effects of such coatings will be presented in Chapter 6.

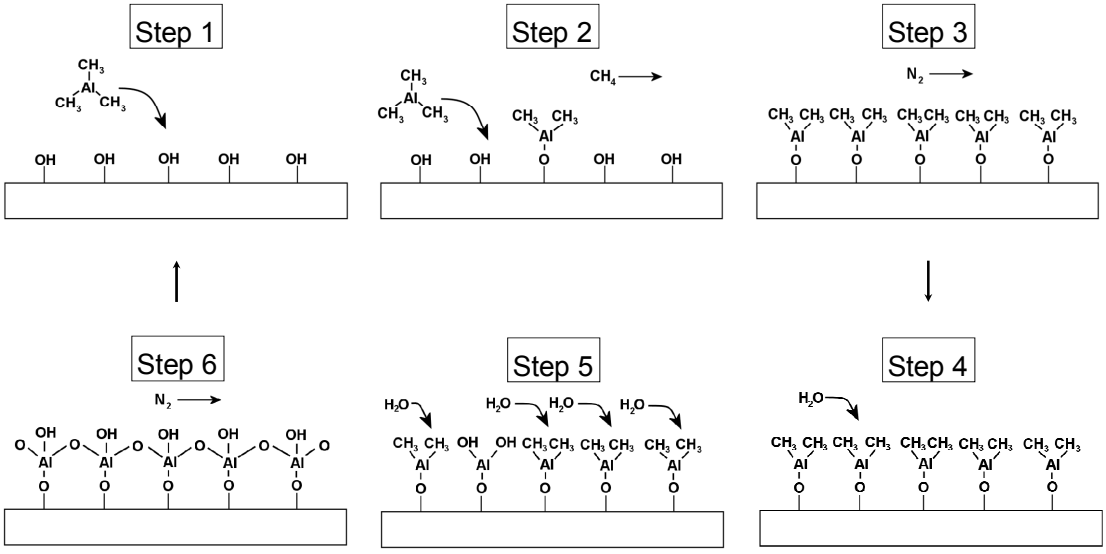

Figure 1.6 Atomic layer deposition: steps in the TMA/water process.

References

1. *Energy Efficiency: A Recipe for Success*, World Energy Council Report, London, 2010.
2. S. Singhal and K. Kendall (Eds.), *High temperature solid oxide fuel cells: fundamentals, design and applications*, Elsevier, Oxford, 2003.
3. R. O'Hayre, S.-W. Cha, W. Collela, and F. B. Prinz, *Fuel Cell Fundamentals*, 2nd Ed., Wiley, Hoboken, 2009.
4. N. G. Minh and T. Takahashi (Eds.), *Science and technology of ceramic fuel cells*, Elsevier, Amsterdam, 1995.
5. R. Bove and P. Lunghi, Electric power generation from landfill gas using traditional and innovative technologies, *Energy Conv. Manag.*, **47**, 1391 (2006).
6. J. Pusz, R. Bove, and N. M. Sammes, Landfill gas energy recovery based on micro-tubular solid oxide fuel cells, *Proceedings of the Ninth Symposium on Solid Oxide Fuel Cells (SOFC-IX)*, Quebec City, Canada, p. 277 (2005).
7. S. Park, J. M. Vohs, and R. J. Gorte, Direct oxidation of hydrocarbons in a solid-oxide fuel cell*, Nature*, **404**, 265 (2000).
8. H. Kim, S. Park, J. M. Vohs, and R. J. Gorte, Direct oxidation of liquid fuels in a solid oxide fuel cell, *J. Electrochem. Soc.*, **148**(7), A693 (2001).
9. S. McIntosh and R. J. Gorte, Direct hydrocarbon solid oxide fuel cells, *Chem. Rev.*, **104**, 4845 (2004).

10. A. Jayakumar, R. Küngas, S. Roy, A. Javadekar, D. J. Buttrey, J. M. Vohs, and R. J. Gorte, A direct carbon fuel cell with a molten antimony anode, *Energy Environ. Sci.*, **4**, 4133 (2011).
11. H. Abernathy, R. Gemmen, K. Gerdes, M. Koslowske, and T. Tao, Basic properties of a liquid tin anode solid oxide fuel cell, *J. Power Sources*, **196** 4564 (2011).
12. N. G. Minh, Ceramic fuel cells, *J. Am. Ceram. Soc.*, **76**[3], 563 (1993).
13. M. J. Jørgensen, S. Primdahl, C. Bagger, and M. Mogensen, Effect of sintering temperature on microstructure and performance of LSM–YSZ composite cathodes, *Solid State Ionics*, **139**, 1 (2001).
14. A. J. Jacobsen, Materials for solid oxide fuel cells, *Chem. Mater.*, **22**, 660, (2010).
15. J. Robertson, High dielectric constant gate oxides for metal oxide Si transistors, *Rep. Prog. Phys.*, **69**, 327 (2006).
16. H. G. Scott, Phase relationships in the zirconia-yttria system, *J. Mater. Sci.*, **10**, 1527 (1975).
17. A. V. Virkar, Mechanism of oxygen electrode delamination in solid oxide electrolyzer cells, *Int. J. Hydrogen Energy*, **35**, 9527 (2010).
18. B. de Boer, M. Gonzalez, and H. J. M Bouwmeester, and H. Verweij, The effect of the presence of fine YSZ particles on the performance of porous nickel electrodes, *Solid State Ionics*, **127**[3-4], 269 (2000).
19. A. Bieberle and L. J. Gauckler, Reaction mechanism of Ni pattern anodes for solid oxide fuel cells, *Solid State Ionics*, **135**[1-4], 337 (2000).

20. M. Mogensen, K. V. Jensen, M. J. Jørgensen, and S. Primdahl, Progress in understanding SOFC electrodes, *Solid State Ionics*, **150**[1-2], 123 (2002).
21. D. Kanno, N. Shikazono, N. Takagi, K. Matsuzaki, and N. Kasagi, Evaluation of SOFC anode polarization simulation using three-dimensional microstructures reconstructed by FIB tomography, *Electrochim. Acta*, **56**, 4015 (2011).
22. T. Klemensø, K.Thydén, M. Chen, and H.-J. Wang, Stability of Ni-yttria stabilized zirconia anodes based on Ni-impregnation, *J. Electrochem. Soc.*, **152**, A2186 (2005).
23. O. A. Marina, L. R. Pederson, C. A. Coyle, E. C. Thomsen, P. Nachimuthu, and D. J. Edwards, Electrochemical, structural and surface characterization of nickel/zirconia solid oxide fuel cell anodes in coal gas containing antimony, *J. Power Sources*, **196**, 4911 (2011).
24. O. A. Marina, C. A. Coyle, E. C. Thomsen, D. J. Edwards, C. W. Coffey, and L. R. Pederson, Degradation mechanism of SOFC anodes in coal gas containing phosphorus, *Solid State Ionics*, **181**, 401 (2010).
25. G. Nurk, P. Holtappels, R. Figi, J. Wochele, M. Wellinger, A. Braun, and T. Graule, A versatile salt evaporation reactor system for SOFC operando studies on anode contamination and degradation with impedance spectroscopy, *J. Power Sources*, **196**[6], 3134 (2011).
26. Y. Matsuzaki and I. Yasuda, The poisoning effect of sulfur-containing impurity gas on a SOFC anode: Part I. Dependence on temperature, time, and impurity concentration, *Solid State Ionics*, **132**[3-4], 261 (2000).

27. M. Pihlatie, A. Kaiser, P. H. Larsen, and M. Mogensen, Dimensional Behavior of Ni–YSZ Composites during Redox Cycling, *J. Electrochem. Soc.*, **156**, B322 (2009).
28. T. Klemensø, C. Chung, P. H. Larsen, and M. Mogensen, The mechanism behind redox instability of anodes in high-temperature SOFCs, *J. Electrochem. Soc*., **152**, A2186 (2005).
29. M. L. Toebes, J. H. Bitter, A. J. van Dillen, and K. P. de Jong, Impact of the structure and reactivity of nickel particles on the catalytic growth of carbon nanofibers, *Catal. Today*, **76**, 33 (2002).
30. S. Helveg, C. López-Cartes, J. Sehested, P. L. Hansen, B. S. Clausen, J. R. Rostrup-Nielsen, F. Abild-Pedersen, and J. K. Nørskov, Atomic-scale imaging of carbon nanofibre growth, *Nature*, **427**, 426 (2004).
31. B. O. Boskovic, V. Stolojan, R. U.A. Khan, S. Haq, and S. R. P. Silva, Large-area synthesis of carbon nanofibres at room temperature, *Nature Mat.*, **1**, 165 (2002).
32. J.-H. Koh, B.-S. Kang, H. C. Lim, and Y.-S. Yoo, Thermodynamic analysis of carbon deposition and electrochemical oxidation of methane for SOFC anodes, *Electrochem. Solid State Lett.*, **4**[2], A12 (2001).
33. Y. Huang, J. M. Vohs, and R. J. Gorte, Characterization of LSM-YSZ Composites Prepared by Impregnation Methods, *J. Electrochem. Soc.,* **152**[7] A1347 (2005).
34. Y. Ji, J. A. Kilner, and M. F. Carolan, Electrical properties and oxygen diffusion in yttria-stabilised zirconia (YSZ)–$La_{0.8}Sr_{0.2}MnO_{3\pm\delta}$ (LSM) composites, *Solid State Ionics*, **176**, 937 (2005).

35. H. Y. Afeefy, J. F. Liebman, and S. E. Stein, *Neutral Thermochemical Data* in *NIST Chemistry WebBook*, Eds. P.J. Linstrom and W.G. Mallard, http://webbook.nist.gov, (retrieved March 4, 2012).

36. V. A. C. Haanappel, N. Jordan, A. Mai, J. Mertens, J. M. Serra, F. Tietz, S. Uhlenbruck, I. C. Vinke, M. J. Smith, L. G. J. de Haart, Advances in research, development, and testing of single cells at Forschungzentrum Jülich, *J. Fuel Cell Sci. Tech.*, **6**, 021302 (2009).

37. Q. Zhu, L. Peng, and T. Zhang in *Fuel cell electronics packaging*, K. Kuang, K. Easler (Eds.), Springer, New York, p33 (2007).

38. V. V. Kharton, F. M. B. Marques, and A. Atkinson, Transport properties of solid oxide electrolyte ceramics: a brief review, *Solid State Ionics*, **174**, 135 (2004).

39. B. C. H. Steele, Appraisal of $Ce_{1-y}Gd_yO_{2-y/2}$ electrolytes for IT-SOFC operation at 500°C, *Solid State Ionics*, **129**, 95 (2000).

40. R. Küngas, J. M. Vohs, and R. J. Gorte, Effect of ionic conductivity of the electrolyte in composite SOFC cathodes, *J. Electrochem. Soc*, **158**[6], B743 (2011).

41. P. I. Cowin, C. T. G. Petit, R. Lan, J. T. S. Irvine, and S. Tao, Recent progress in the development of anode materials for solid oxide fuel cells, *Advanced Energy Mater.*, **1**, 314 (2011).

42. S. Lee, G. Kim, J. M. Vohs, and R. J. Gorte, SOFC anodes based on infiltration of $La_{0.3}Sr_{0.7}TiO_3$, *J. Electrochem. Soc.,* **155**[11], B1179 (2008).

43. S. Tao and J. T. S. Irvine, A redox-stable efficient anode for solid oxide fuel cells, *Nature Mater.*, **2**, 320 (2003).

44. G. Kim, G. Corre, J. T. S. Irvine, J. M. Vohs, and R. J. Gorte, Engineering composite oxide SOFC anodes for efficient oxidation of methane, *Electrochem. Solid-State Lett.,* **11**[2], B16 (2008).

45. G. Kim, S. Lee, J. Y. Shin, G. Corre, J. T. S. Irvine, J. M. Vohs, and R. J. Gorte, Investigation of the structural and catalytic requirements for high-performance SOFC anodes formed by infiltration of LSCM, *Electrochem. Solid-State Lett.,* **12**[3], B48 (2009).

46. J.-S. Park, I. D. Hasson, M. D. Gross, C. Chen, J. M. Vohs, and R. J. Gorte, A high-performance solid oxide fuel cell anode based on lanthanum strontium vanadate, *J. Power Sources*, **196**, 7488 (2011).

47. L. Adijanto, V. B. Padmanabhan, K. Holmes, R. J. Gorte, and J. M. Vohs, Physical and electrochemical properties of alkaline earth doped, rare earth vanadates, *J. Solid State Chem.*, in press, doi:10.1016/j.jssc.2012.01.065.

48. L. Adijanto, R. Küngas, J. Park, J. M. Vohs, and R. J. Gorte, SOFC anodes based on infiltration of tungsten bronzes, *Int. J. Hydrogen Energy*, **36**, 15722, (2011).

49. J. M. Vohs and R. J. Gorte, High-performance SOFC cathodes prepared by infiltration, *Adv. Mat.,* **21**[9], 943 (2009).

50. I. Wærnhus, T. Grande, and K. Wiik, Electronic properties of polycrystalline $LaFeO_3$. Part II: Defect modelling including Schottky defects, *Solid State Ionics*, **176**[35-36], 2609 (2005).

51. M. Søgaard, P. V. Hendriksen, and M. Mogensen, Oxygen nonstoichiometry and transport properties of strontium substituted lanthanum ferrite, *J. Solid State Chem.*, **180**, 1489 (2007).

52. T. Montini, M. Bevilacqua, E. Fonda, M. F. Casula, S. Lee, C. Tavagnacco, R. J. Gorte, and P. Fornasiero, Relationship between electrical behavior and structural characteristics in Sr-doped $LaNi_{0.6}Fe_{0.4}O_{3-\delta}$ mixed oxides, *Chem. Mater.*, **21**, 1768 (2009).

53. Y. Ren, R. Küngas, R. J. Gorte, and C. Deng, The effect of A-site cation (Ln = La, Pr, Sm) on the crystal structure, conductivity and oxygen reduction properties of Sr-doped ferrite perovskites, *Solid State Ionics*, **212**, 47 (2012).

54. C. W. Tanner, K.-Z. Fung, and A. V. Virkar, The effect of porous composite electrode structure on solid oxide fuel cell performance: Part I - theoretical analysis, *J. Electrochem. Soc.*, **144**, 21 (1997).

55. S. B. Adler, Factors governing oxygen reduction in solid oxide fuel cell cathodes, *Chem. Rev.*, **104**, 4791 (2004).

56. M. J. L. Østergård, C. Clausen, C. Bagger and M. Mogensen, Manganite-zirconia composite cathode for SOFC: influence of structure and composition, *Electrochim. Acta*, **40**[12], 1971 (1995).

57. F. Bidrawn, R. Küngas, J. M. Vohs, and R. J. Gorte, Modeling impedance response of SOFC cathodes prepared by infiltration, *J. Electrochem. Soc.*, **158**[5], B514 (2011).

58. H. He, Y. Huang, J. Regal, M. Boaro, J. M. Vohs, and R. J. Gorte, Low-temperature fabrication of oxide composites for solid-oxide fuel cells, *J. Am. Ceram. Soc.,* **87**[3], 331 (2004).

59. Y. Huang, J. M. Vohs, and R. J. Gorte, Fabrication of Sr-doped $LaFeO_3$ YSZ composite cathodes, *J. Electrochem. Soc.,* **151**[4], A646 (2004).

60. Y. Huang, J. M. Vohs, and R. J. Gorte, SOFC cathodes prepared by infiltration with various LSM precursors, *Electrochem. Solid-State Lett.,* **9**[5], A237 (2006).

61. Y. Huang, K. Ahn, J. M. Vohs, and R. J. Gorte, Characterization of Sr-doped $LaCoO_3$-YSZ composites prepared by impregnation methods, *J. Electrochem. Soc.,* **151**[10], A1592 (2004).

62. W. Wang, M. D. Gross, J. M. Vohs, and R. J. Gorte, The stability of LSF-YSZ electrodes prepared by infiltration, *J. Electrochem. Soc.*, **154**[5], B439 (2007).

63. R. E. Mistler and E. R. Twiname, *Tape casting: theory and practice*, pp. 298. The American Ceramic Society: Westerville, OH, (2000).

64. R. Küngas, J.-S. Kim, J. M. Vohs, and R. J. Gorte, Restructuring porous YSZ by treatment in hydrofluoric acid for use in SOFC cathodes, *J. Am. Ceram. Soc*, **94**[7], 2220 (2011).

65. R. Küngas, F. Bidrawn, J. M. Vohs, and R. J. Gorte, Doped-ceria diffusion barriers prepared by infiltration for solid oxide fuel cells, *Electrochem. Solid-State Lett.*, **13**, B87 (2010).

66. M. Mosleh, M. Søgaard, and P. V. Hendriksen, Kinetics and mechanisms of oxygen surface exchange on $La_{0.6}Sr_{0.4}FeO_{3-\delta}$ thin films, *J. Electrochem. Soc.*, **156**[4], B441 (2009).

67. E. N. Armstrong, K. L. Duncan, D. J. Oh, J. F. Weaver, and E. D. Wachsman, Determination of surface exchange coefficients of LSM, LSCF, YSZ, GDC constituent materials in composite SOFC cathodes, *J. Electrochem. Soc.*, **158**[5], B492 (2011).

68. W. Sitte, E. Bucher, and W. Preis, Nonstoichiometry and transport properties of strontium-substituted lanthanum cobaltites, *Solid State Ionics*, **154-155**, 517 (2002).

69. H. J. M. Bouwmeester, H. Kruidhof, and A. J. Burggraaf, Importance of the surface exchange kinetics as rate limiting step in oxygen permeation through mixed-conducting oxides, *Solid State Ionics*, **72**, 185 (1994).

70. A. V. Berenov A. Atkinson, J. A. Kilner, E. Bucher, and W. Sitte, Oxygen tracer diffusion and surface exchange kinetics in $La_{0.6}Sr_{0.4}CoO_{3-\delta}$, *Solid State Ionics*, **181**, 819 (2010).

71. J. A. Kilner, R. A. De Souza, and I. C. Fullarton, Surface exchange of oxygen in mixed conducting perovskite oxides, *Solid State Ionics*, **86-88**, 703 (1996).

72. A. Endo, H. Fukunaga, C. Wen, and K. Yamada, Cathodic reaction mechanism of dense $La_{0.6}Sr_{0.4}CoO_3$ and $La_{0.81}Sr_{0.09}MnO_3$ electrodes for solid oxide fuel cells, *Solid State Ionics*, **135**, 353 (2000).

73. N. Hildenbrand, B. A. Boukamp, and P. Nammensma, D. H. A. Blank, Improved cathode/electrolyte interface of SOFC, *Solid State Ionics*, **192**, 12 (2011).

74. S. B. Adler, Mechanism and kinetics of oxygen reduction on porous $La_{1-x}Sr_xCoO_{3-\delta}$ electrodes, *Solid State Ionics*, **111**, 125 (1998).

75. L. Wang, R. Merkle, and J. Maier, Surface kinetics and mechanism of oxygen incorporation into $Ba_{1-x}Sr_xCo_yFe_{1-y}O_{3-\delta}$ SOFC microelectrodes, *J. Electrochem. Soc.*, **157**, B1802 (2010).

76. J. Mizusaki, M. Okayasu, S. Yamauchi, and K. Fueki, Nonstoichiometry and phase relationship of the $SrFeO_{2.5}$-$SrFeO_3$ system at high temperature, *J. Solid State Chem*., **99**, 166 (1992).

77. F. S. Baumann, J. Fleig, H.-U. Habermeier, and J. Maier, Impedance spectroscopic study on well-defined $(La,Sr)(Co,Fe)O_{3-\delta}$ model electrodes, *Solid State Ionics*, **177**, 1071 (2006).

78. S. Hashimoto, Y. Fukuda, M. Kuhn, K.Sato, K. Yashiro, and J. Mizusaki, Oxygen nonstoichiometry and thermo-chemical stability of $La_{0.6}Sr_{0.4}Co_{1-y}Fe_yO_{3-\delta}$ (y=0.2, 0.4, 0.6, 0.8), *Solid State Ionics*, **181**, 1713 (2010).

79. M. Søgaard, P. V. Hendriksen, M. Mogensen, F. W. Poulsen, and E. Skou, Oxygen nonstoichiometry and transport properties of strontium substituted lanthanum cobaltite, *Solid State Ionics*, **177**, 3285 (2006).

80. I. Yasuda and M. Hishinuma, Electrical conductivity and chemical diffusion coefficient of Sr-doped lanthanum chromites, *Solid State Ionics*, **80**, 141 (1995).

81. R. Ganeshananthan and A. V. Virkar, Measurement of surface exchange coefficient on porous $La_{0.6}Sr_{0.4}CoO_{3-\delta}$ samples by conductivity relaxation, *J. Electrochem. Soc.*, **152**[8], A1620 (2005).

82. R. A. Cox-Galhotra and S. McIntosh, Unreliability of simultaneously determining k_{chem} and D_{chem} via conductivity relaxation for surface-modified $La_{0.6}Sr_{0.4}Co_{0.2}Fe_{0.8}O_{3-\delta}$, *Solid State Ionics*, **181**, 1429 (2010).

83. C. C. Kan, H. H. Kan, F. M. Van Assche IV, E. N. Armstrong, and E. D. Wachsman, Investigating oxygen surface exchange kinetics of $La_{0.8}Sr_{0.2}MnO_{3-\delta}$ and $La_{0.6}Sr_{0.4}Co_{0.2}Fe_{0.8}O_{3-\delta}$ using an isotopic tracer, *J. Electrochem. Soc.*, **155**[10], B985 (2008).

84. H. J. M. Bouwmeester, C. Song, J. Zhu, J. Yi, M. van Sint Annaland, and B. A. Boukamp, A novel pulse isotopic exchange technique for rapid determination of the oxygen surface exchange rate of oxide ion conductors, *Phys. Chem. Chem. Phys.*, **11**, 9640 (2009).

85. E. J. Opila, H. L. Tuller, B. J. Wuensch, and J. Maier, Oxygen tracer diffusion in $La_{2-x}Sr_xCuO_{4-y}$ single crystals, *J. Am. Ceram. Soc.*, **76**[9], 2363 (1993).

86. J. A. Kilner, S. J. Skinner, H. H. Bronnersma, The isotope exchange depth profiling (IEDP) technique using SIMS and LEIS, *J. Solid State Electrochem.*, **15**[5], 861 (2011).

87. I. Yasuda and T. Hikita, Precise Determination of the chemical diffusion coefficient of calcium-doped lanthanum chromites by means of electrical conductivity relaxation *J. Electrochem. Soc.*, **141**, 1268 (1994).

88. F. Bidrawn, S. Lee, J. M. Vohs, and R. J. Gorte, The effect of Ca, Sr, and Ba doping on the ionic conductivity and cathode performance of $LaFeO_3$, *J. Electrochem. Soc.,* **155**[7], B660 (2008).

89. F. Bidrawn, G. Kim, N. Aramrueang, J. M. Vohs, and R. J. Gorte, Dopants to enhance SOFC cathodes based on Sr-doped $LaFeO_3$ and $LaMnO_3$, *J. Power Sources,* **195**[3], 720 (2010).

90. R. A. Wind and S. M. George, Quartz crystal microbalance studies of Al_2O_3 atomic layer deposition using trimethylaluminum and water at 125 °C, *J. Phys. Chem. A*, **114**, 1281 (2010).

91. T. Suntola, Atomic layer epitaxy, *Thin Solid Films*, **216**, 84 (1992).

92. M. Cassir, A. Ringuedé, and L. Niinistö, Input of atomic layer deposition for solid oxide fuel cell applications, *J. Mater. Chem.*, **20**, 8987 (2010).

93. R. L. Puurunen, Surface chemistry of atomic layer deposition: A case study for the trimethylaluminum/water process, *J. Appl. Phys.*, **97**, 121301 (2005).

Chapter 2. Effect of the Ionic Conductivity of the Electrolyte in Composite SOFC Cathodes*

Summary

Solid oxide fuel cell (SOFC) cathodes were prepared by infiltration of 35-wt% $La_{0.8}Sr_{0.2}FeO_3$ (LSF) into porous scaffolds of three, zirconia-based electrolytes in order to determine the effect of the ionic conductivity of the electrolyte material on cathode impedances. The electrolyte scaffolds were 10 mol.% Sc_2O_3-stabilized zirconia (ScSZ), 8 mol.% Y_2O_3-stabilized zirconia (YSZ), and 3 mol.% Y_2O_3, 20 mol.% Al_2O_3-codoped zirconia (YAZ), prepared by tape casting with graphite pore formers. Each electrolyte scaffold was 65% porous, with identical pore structures as determined by scanning electron microscopy (SEM). Both symmetric cells and fuel cells were prepared and tested between 873 and 1073 K, using LSF composites that had been calcined to 1123 or 1373 K. Literature values for the electrolyte conductivities were confirmed using the ohmic losses from the impedance spectra. The electrode impedances decreased with increasing electrolyte conductivity, with the dependence being between to the power of 0.5 and 1.0, depending on the operating temperature and LSF calcination temperature.

2.1 Introduction

The performance of solid oxide fuel cells (SOFCs) is often limited by the slow kinetics of the oxygen reduction reaction at the cathode. An ideal SOFC cathode material

* This chapter was published as a research paper in the Journal of the Electrochemical Society, 158(6) (2011) B743.

would have excellent catalytic activity, together with high electronic conductivity (to provide electrons for the oxygen reduction reaction) and ionic conductivity (to transport the oxygen ions from the cathode into the electrolyte) [1-3]. The material most commonly used in SOFC cathodes is LSM ($La_{1-x}Sr_xMnO_3$), which satisfies the conditions of catalytic activity and electronic conductivity, but has a very low ionic conductivity ($\sigma_{i,LSM} = 4 \cdot 10^{-8}$ S/cm at 1073 K [4]). When pure LSM is used as the cathode, its low ionic conductivity results in the active zone of the cathode being limited to the three-phase boundary (TPB) line in the immediate vicinity of the electrolyte. In order to extend the reaction zone further into the cathode bulk, LSM is usually mixed with a good ionic conductor, most commonly the electrolyte material (e.g. YSZ, yttria-stabilized zirconia) to form a composite [3,5-12]. Such composites combine the best of the properties of both components, resulting in a material that simultaneously meets all the requirements for SOFC cathodes. In addition to providing more TPB sites, the use of composites is also advantageous for mechanical stability, since it alleviates the problem of thermal expansion coefficient mismatch between the electrolyte and electronic conductor [13-15].

Alternative perovskites with mixed ionic and electronic conductivity (MIEC), such as LSF ($La_{1-x}Sr_xFeO_3$) or LSCF ($La_{1-x}Sr_xCo_{1-y}Fe_yO_3$) have also been proposed as cathode materials for SOFCs, especially for operation at lower temperatures, 873 to 1073 K [16-25]. The ionic conductivity of LSF is significantly higher than that of LSM ($\sigma_{i,LSF} = 1.5 \cdot 10^{-5}$ S/cm at 973 K [26]), so that oxygen adsorption and reduction do not have to be spatially confined to the TPB sites [3,15,27]. However, the ionic conductivity of

MIECs is still much lower than that of the YSZ ($\sigma_{i,YSZ} = 1.8 \cdot 10^{-2}$ S/cm at 973 K [28]). Therefore, using a composite of an MIEC perovskite and YSZ can significantly improve the performance of SOFC cathodes compared to using the perovskite alone.

The motivation of the present study was to better understand the effect of the ionic conductivity of the electrolyte in composite cathodes. Although numerous studies, both experimental and theoretical, suggest that the ionic conductivity of the electrolyte within composite SOFC electrodes can be very important for electrode performance, we are unaware of any systematic investigations on this topic. For example, while it has been demonstrated that the substitution of YSZ in Ni-YSZ anodes with doped ceria results in performance enhancement [29-32], it remains uncertain whether this is due to the higher ionic conductivity of ceria or due to the fact that ceria possesses significant catalytic activity for the electrode reaction. That catalytic activity may be responsible is suggested from the results of Sumi, *et al*. who compared the performance of Ni-YSZ and Ni-ScSZ (scandia-doped zirconia) anodes [33]. While the ionic conductivity of ScSZ is significantly higher than that of YSZ, the authors found negligible differences in performance for Ni-YSZ and Ni-ScSZ electrodes, with YSZ-based cells even outperforming the ScSZ-cells under some conditions [33].

The situation is similarly uncertain for SOFC composite cathodes. Perry Murray and Barnett observed significantly lower polarization resistances for composites of LSM with Gd-doped ceria compared to that of LSM-YSZ [34] and Yamahara *et al*. reported improved performance of LSM-SYSZ (SYSZ = $(Sc_2O_3)_{0.1}(Y_2O_3)_{0.01}(ZrO_2)_{0.89}$) electrodes compared to LSM-YSZ due to the higher ionic conductivity of SYSZ [12], However,

Wang *et al*. reported that the polarization resistance of LSM-ScCeSZ (scandia-ceria stabilized zirconia) composite cathodes decreased with ceria content, in the direction opposite to increasing ionic conductivity [35]. Finally, modeling studies by Tanner *et al*. [3], and Bidrawn *et al*. [36] suggest that the polarization resistance of composite electrodes should have an inverse square-root dependence on the ionic conductivity of the electrolyte, provided all other parameters are held constant.

Unfortunately, it is very difficult to ensure that only one parameter is varied at a time when traditional cell preparation techniques are used. For example, it is often necessary to change the preparation conditions, such as the sintering temperature, when using different electrolytes, so that the microstructure of the electrode could change with the electrolyte conductivity. This is the case with doped ceria electrolytes, for which the sintering temperatures are typically higher than corresponding temperatures for stabilized zirconia electrolytes. Indeed, Yamahara *et al*. recently expressed doubts whether the high ionic conductivities of the electrolyte materials used in composite electrodes are the dominant factor responsible for the comparative enhancements seen in cathode activity [11]. As pointed out earlier for SOFC anodes, enhanced performance with cathode composites prepared from doped ceria may be due to enhanced catalytic activity [37-40].

In this study, infiltration methods were used to prepare the electrode composites because they offer a number of advantages relative to traditional fabrication methods [41,42]. First, the electrolyte scaffold is calcined separately at high temperatures, prior to the addition of the perovskite, so that there is good connectivity in the electrolyte phase

and no solid-state reactions between the two phases of the composite. Furthermore, by using tape casting with the same pore formers, the structure of the electrolyte scaffold can be prepared identical for different electrolytes. In order to vary other materials properties of the electrolyte phase (e.g. surface energy, reducibility, chemical stability, activity as catalyst, etc.) as little as possible, we chose to compare three zirconia-based materials with very different ionic conductivies: 8 mol.% Y_2O_3-stabilized zirconia (YSZ), 10 mol.% Sc_2O_3-stabilized zirconia (ScSZ), and 3 mol.% Y_2O_3-20 mol.% Al_2O_3-doped zirconia (YAZ) [43]. We will demonstrate that the ionic conductivity of the electrolyte phase is very important in determining the cathode performance.

2.2 Experimental

Identical tape-casting procedures, described in more detail elsewhere [10,41,42,44], were used to prepare porous-dense-porous structures from the three electrolyte materials. The three electrolytes that were used were 8 mol.% yttria-stabilized zirconia (TZ-8Y, Tosoh), 10 mol.% scandia-stabilized zirconia (Sc10SZ-TC, Fuel Cell Materials) or 20 mol.% alumina, 3 mol.% yttria co-doped zirconia (TZ-3Y20A, Tosoh). Tape-casting slurries for the dense layers were prepared by mixing 30 g of either YSZ, ScSZ, or YAZ with 13.5 g of distilled water, 0.8 g dispersant (D3005, Rohm & Haas), 5 g of binder HA12 (Rohm & Haas), and 6.5 g of binder B1000 (Rohm & Haas) in a beaker. Similarly, slurries for porous tapes were prepared by mixing 10 g of the ceramic material with 20 g of water 1.8 g of D3005, 4.8 g HA12, 7.2 g B1000, and 10 g of carbonaceous pore former (graphite, synthetic, <20 μm, Sigma Aldrich).

The green tapes were cut into the desired size and laminated into a porous-dense-porous YSZ trilayer structure. These structures were then fired to 1773 K for YSZ and ScSZ, and to 1823 K for YAZ for 4 h. For each of the trilayer structures, the porous layers were 50 μm in thickness and 65% porous, while the thicknesses of the dense layers were 100 μm for YSZ and ScSZ and 115 μm for YAZ. The diameter of the dense electrolytes was 1 cm, while the porous layers on opposite sides of the electrolyte were 0.67 cm in diameter.

All of the electrodes in the tested cells were produced by infiltration using aqueous nitrate solutions. For LSZ–YSZ, LSF–ScSZ, and LSF–YAZ symmetric cells, both of the porous scaffolds were infiltrated with an aqueous solution consisting of $La(NO_3)_3 \cdot 6\ H_2O$ (Alfa Aesar, 99.9%), $Sr(NO_3)_2$ (Alfa Aesar, 99%), and $Fe(NO_3)_3 \cdot 6\ H_2O$ (Fisher Scientific 98.4%) at a molar ratio of La : Sr : Fe = 0.8 : 0.2 : 1. Citric acid, in a 1 : 1 ratio with the metal cations, was used as a complexing agent to form the perovskite at lower temperatures. Each infiltration step was followed by heat treatment in air at 723 K. Multiple infiltration steps were needed to reach the final loading of 35 wt % (~20 vol%). In order to form the desired perovskite structure, the cells were heated in air to either 1123 K or 1373 K for 4 hours prior to applying Ag paste (SPI Supplies) for current collection.

To produce the fuel cells, the anode side was first infiltrated with a solution of $La(NO_3)_3 \cdot 6\ H_2O$, $Sr(NO_3)_2$, $Cr(NO_3)_3 \cdot 9\ H_2O$ (Acros Organics, 99%), $Mn(NO_3)_2 \cdot 6\ H_2O$ (Alfa Aesar, 99.98%), and citric acid at a molar ratio of La : Sr : Cr : Mn : citric acid = 0.8 : 0.2 : 0.5 : 0.5 : 2. Once a 45 wt% loading of $La_{0.8}Sr_{0.2}Cr_{0.5}Mn_{0.5}O_3$ (LSCM)

was achieved, the composite was fired to 1473 K for 4 hours, followed by the infiltration of the LSF cathode. Finally, 5 wt% of CeO_2 (added as $Ce(NO_3)_3$, Alfa Aesar, 99.5%) and 0.5 wt% Pd (tetraamminepalladium(II) nitrate solution, Alfa Aesar, 99.9%) were added to the anode by infiltration for enhanced catalytic activity, followed by heat treatment at 723 K and the application of Ag current collector paste.

The fuel cells were attached to an alumina tube using a ceramic adhesive (Aremco, Ceramabond 552) so that the fuel (97% H_2-3% H_2O) could be introduced to the anode. Electrochemical impedance spectra were recorded using a Gamry Instruments potentiostat in the frequency range of 0.1 Hz to 100 kHz. All symmetric cell impedances in this paper have been divided by two to account for there being two identical electrodes.

2.3 Results

SEM micrographs of the porous scaffolds prepared from each of the three electrolyte materials are shown in Figure 2.1. The microstructure of the porous YSZ scaffold, Figure 2.1a) was in a good agreement with previous results from our laboratory [10,42,43,45]. The porosity was 65%, as measured by the weight of water uptake, with the structure made up of ~1 μm pores [46]. Using the same recipe for the tape-casting procedure, porous scaffolds of ScSZ and YAZ, with very similar microstructures, were prepared. These are shown in Figure 2.1b) and c). Figure 2.2a) through c) show SEM of the same structures after infiltration of LSF with calcination to 1123 K. The composites are again nearly identical in appearance, with small LSF nanoparticles (~50 nm in diameter) deposited on the scaffold walls. After calcination to 1373 K, Fig. d) through e),

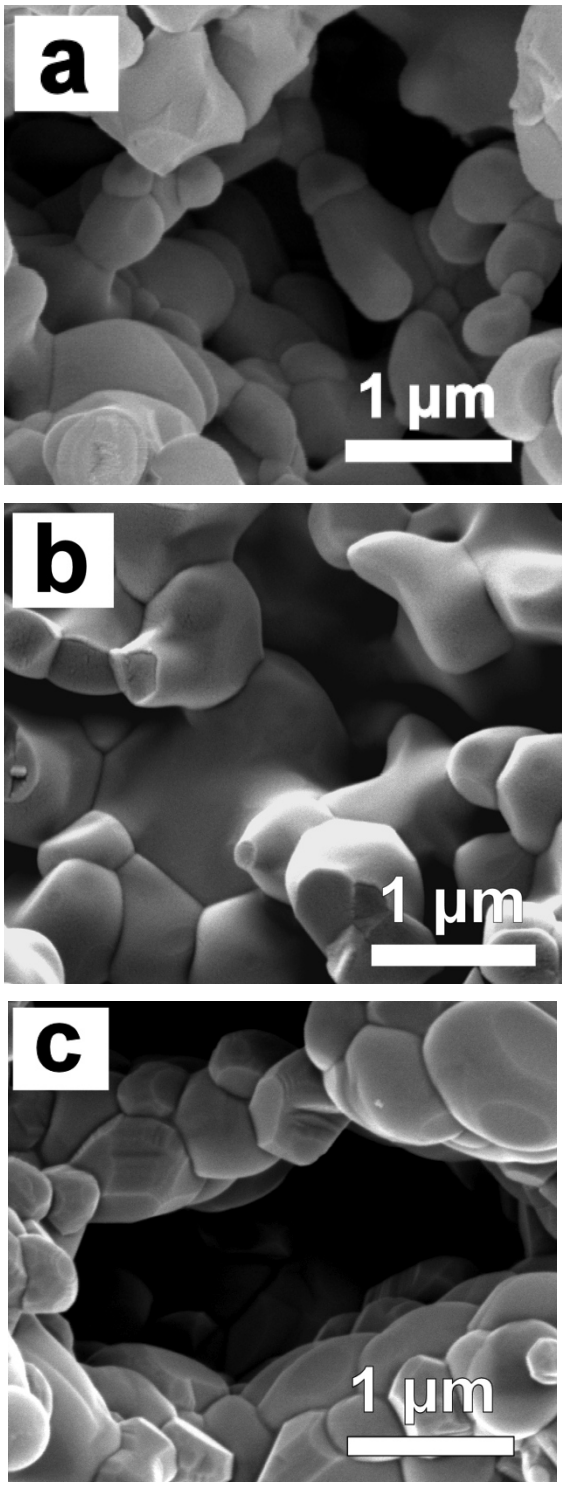

Figure 2.1 SEM images of porous stabilized zirconia scaffolds: (a) YSZ, (b) ScSZ, and (c) YAZ.

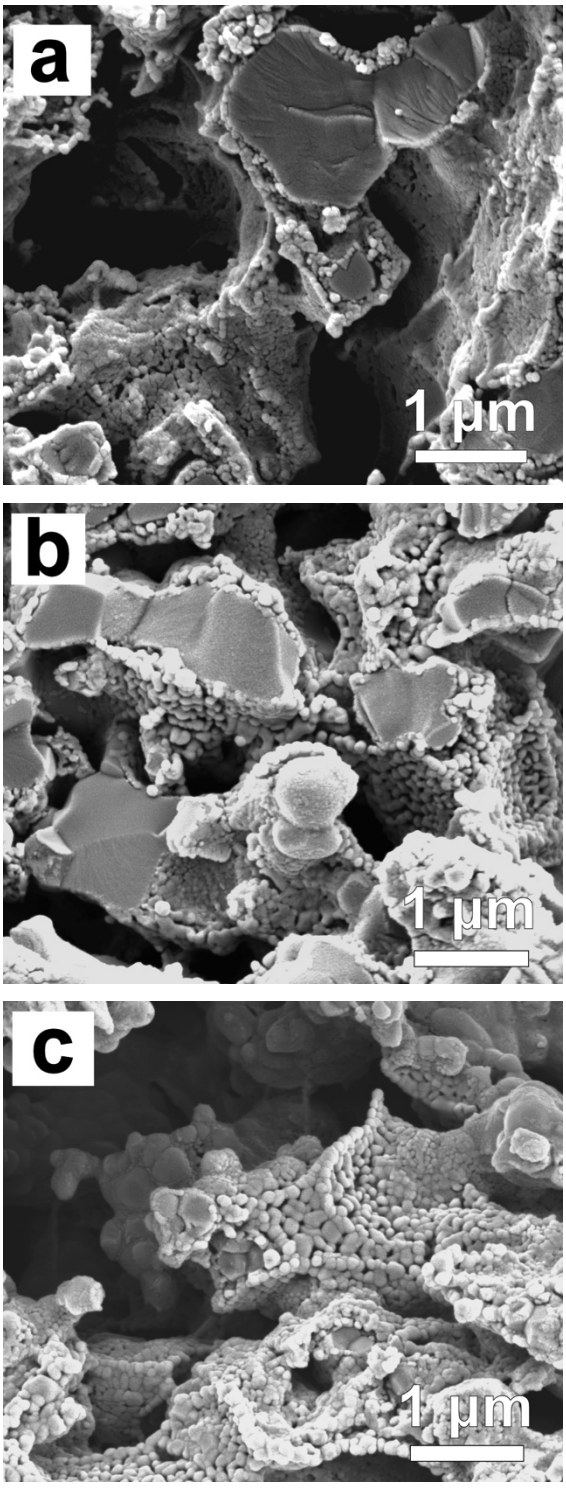

Figure 2.2a-c SEM images of porous 35-wt% LSF-SZ scaffolds calcined to 1123 K: (a) LSF-ScSZ, (b) LSF-YSZ, and (c) LSF-YAZ.

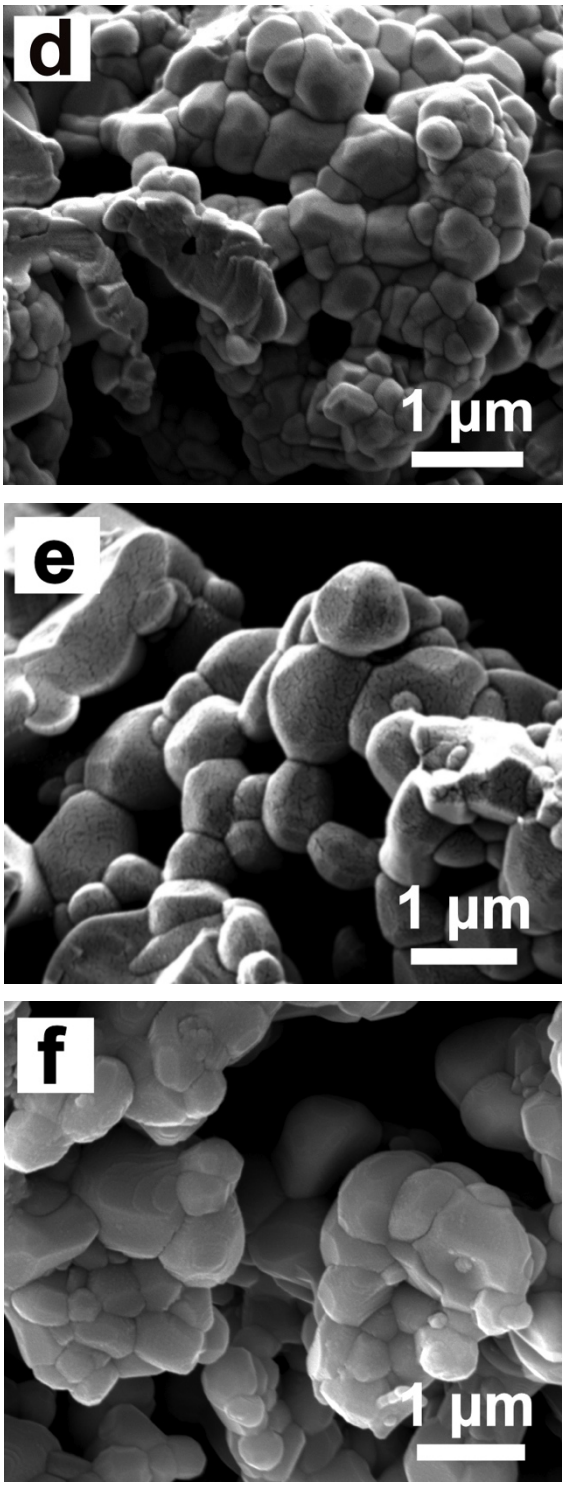

Figure 2.2d-f SEM images of porous 35-wt% LSF-SZ scaffolds calcined to 1373 K: (d) LSF-ScSZ, (e) LSF-YSZ, and (f) LSF-YAZ.

the LSF particles are no longer easily distinguishable from the electrolyte scaffold, appearing to form a dense film of LSF over the scaffolds. Qualitatively, there were no significant differences in the nature of the LSF particles in the three electrolyte scaffolds and the interactions between LSF and the three electrolyte materials were very similar.

Figure 2.3 shows *i-V* polarization curves measured at 973 K for fuel cells made from each of the electrolytes, operating on 97% H_2-3% H_2O at the anode and air at the cathode. The LSF composites in each of the cells had been calcined to 1123 K. The open circuit voltage (OCV) was above 1.05 V in each case, close to the Nernst Potential. However, the effect of electrolyte on the maximum power densities in these three cells is large, the YAZ cell exhibiting a maximum power density of 90 mW/cm^2, the YSZ cell 280 mW/cm^2, and the ScSZ cell 790 mW/cm^2. The *i-V* curves were also reasonably linear, implying that the impedance of cells was nearly independent of the applied load, so that impedance spectra measured at open circuit should provide a good measure of electrode performance. Based on the average slopes of *i-V* curves, the values of overall cell resistances were 0.36 Ω cm^2, 1.1 Ω cm^2, and 3.1 Ω cm^2 for cells based on ScSZ, YSZ, and YAZ, respectively.

The corresponding open-circuit impedance spectra for the three cells shown in Figure 2.4, allow separation of the electrode and electrolyte losses. Based on the impedance spectra, the total cell resistances, determined from the zero-frequency intercept with the real axis in the spectra of Figure 2.4, were 0.28 Ω cm^2 for the ScSZ cell, 0.84 Ω cm^2 for the YSZ cell, and 3.12 Ω cm^2 for the YAZ cell, in reasonable agreement with the average slopes determined from Figure 2.3. The electrolyte losses, calculated from the

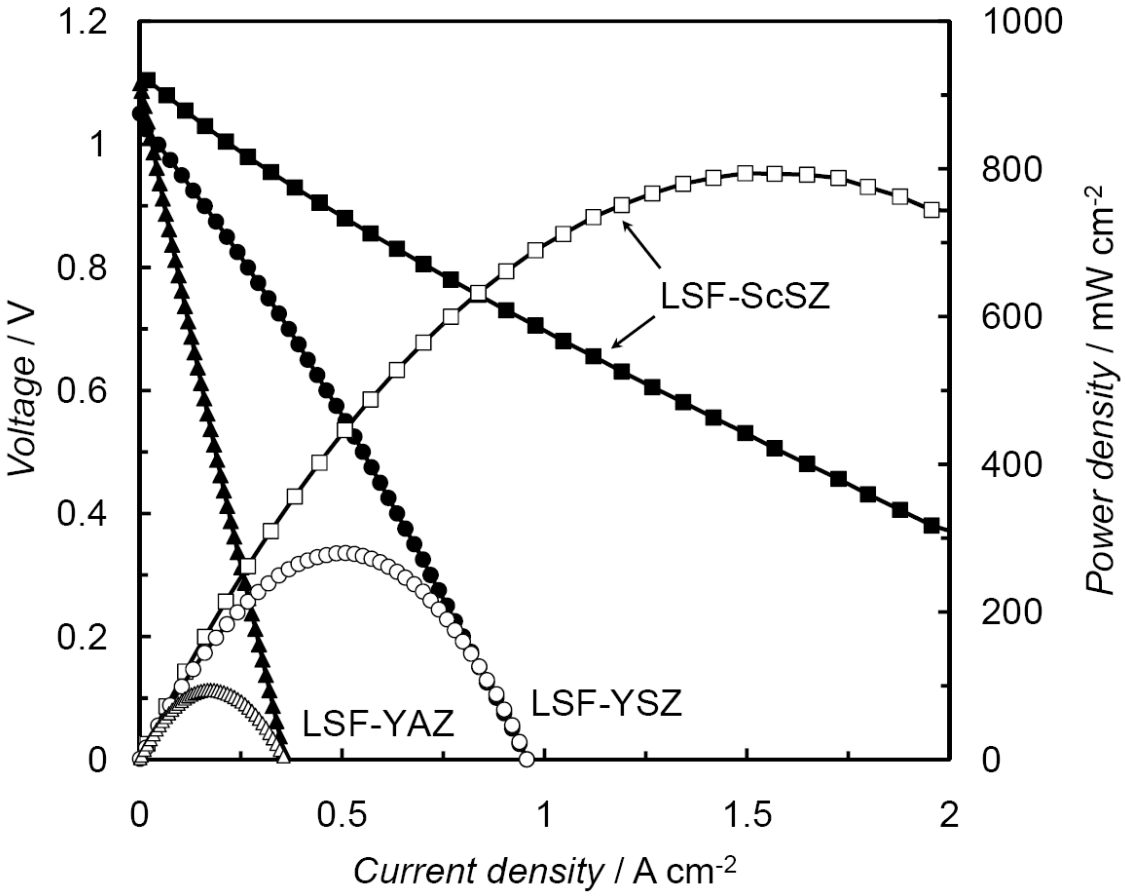

Figure 2.3 Polarization *i-V* curves for of LSF-SZ-LSCM,CeO_2,Pd fuel cell single cells with different electrolyte scaffolds after calcination to 1123 K, measured at 973 K. The cathode was subject to ambient air whereas 3% humidified H_2 was pumped onto the anode side. Closed symbols – voltage, open symbols – power density.

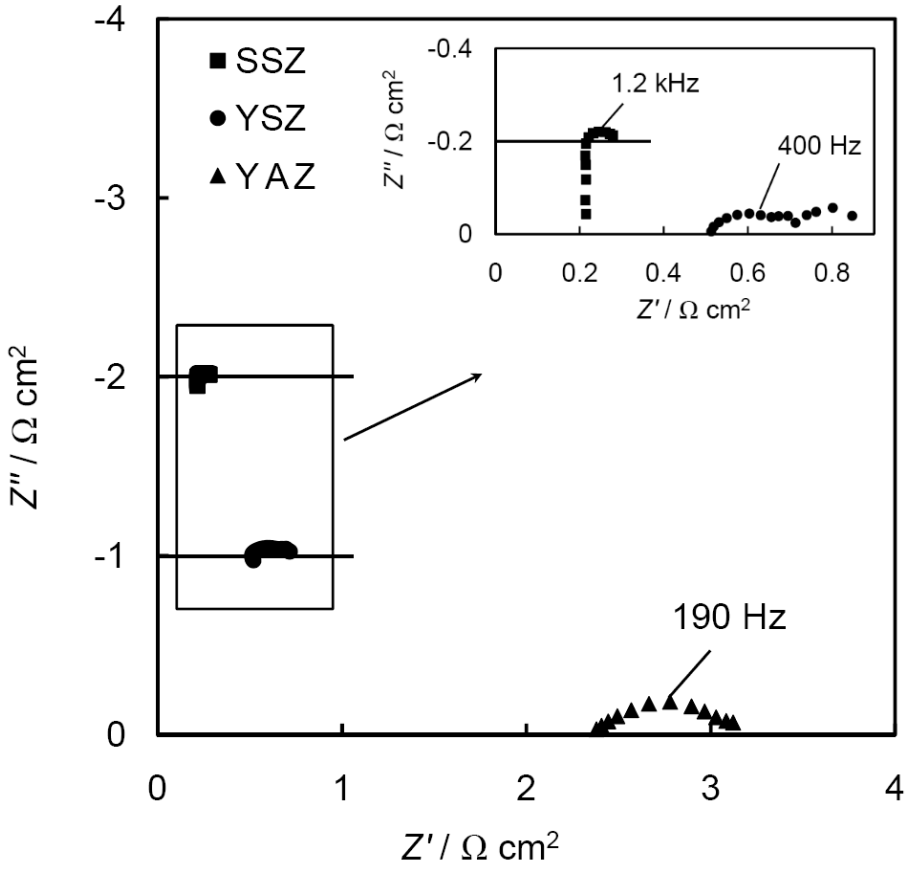

Figure 2.4 Electrochemical impedance spectra of LSF-SZ-LSCM, CeO_2, Pd fuel cell single cells with different electrolyte scaffolds after calcination to 1123 K, measured at 973 K in ambient air and open circuit conditions. Squares – ScSZ, circles – YSZ, triangles – YAZ.

high-frequency intercept with the real axis in the impedance spectra, were a large fraction of the losses in each cell. At 973 K, the ohmic contribution to the cells was 0.22 Ω cm^2 for the ScSZ cell, 0.51 Ω cm^2 for the YSZ cell, and 2.37 Ω cm^2 for the YAZ cell. When these losses are subtracted off from the total cell losses, the polarization losses associated with the electrodes are obtained, 0.06 Ω cm^2, 0.33 Ω cm^2, and 1.16 Ω cm^2 for LSF composites with ScSZ, YSZ, and YAZ, respectively. These data indicate that electrode losses depend strongly on the ionic conductivity of the electrolyte scaffold. However, because there are contributions from both the anode and cathode in these measurements, it is difficult to quantify the effect of the electrolyte from Figure 2.4.

Since the ohmic contributions to the cell performance should not be affected by the electrodes, data like that in Figure 2.4 can be used to measure the ionic conductivities of the three electrolytes and therefore provide a consistency check for the materials that we used. Therefore, impedance spectra were measured between 873 K and 1073 K on each of the cells and the ohmic losses were used to calculate the ionic conductivities from the known electrolyte thicknesses. (The ionic conductivity, σ_i, is related to the ohmic resistance, R_Ω, and the thickness of the electrolyte, l, by $\sigma_i = l / R_\Omega$.) The ionic conductivities determined from this are plotted in Fig. 2.5 along with literature data for each of the three electrolytes [28,43,46]. With the possible exception of the conductivity of ScSZ at 873 K, all of the experimental data agree with the literature values within the uncertainty of the measurements.

In order to isolate the effect of varying the electrolyte material on the electrochemical activity of the composite cathodes, symmetric cells were prepared in

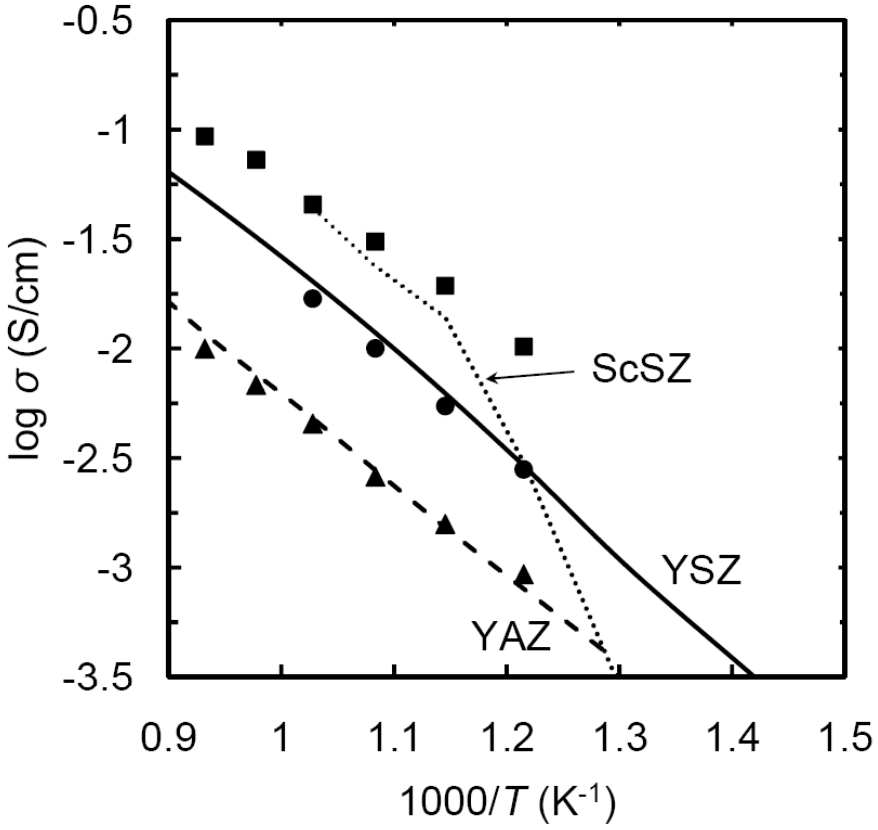

Figure 2.5 Comparison of experimental data (symbols), calculated from the high-frequency intercepts of fuel cell Cole-Cole plots, and literature values for the conductivity of the three electrolyte materials studied. References: ScSZ [46]; YSZ [28], YAZ [43].

which LSF was infiltrated into both sides of the porous-dense-porous stabilized-zirconia structures. Impedance spectra were then measured in air over the temperature range from 873 to 973 K, the spectra obtained at 973 K shown in Figure 2.6 for cells in which the LSF was calcined at 1123 K. The ohmic losses have been subtracted from the Cole-Cole plots and the values divided by two to account for the there being two electrodes. In agreement with the fuel cell data, the polarization resistances, R_p, increased with decreasing conductivity, with R_p being the smallest for ScSZ and the largest for YAZ. The values obtained from Figure 2.6 for R_p at 973 K were 0.06 Ω cm^2 on the ScSZ cell, 0.14 Ω cm^2 on the YSZ cell, and 0.72 Ω cm^2 on the YAZ cell. These values are consistent with the impedances measured on the fuel cells in Figure 2.3. Since the *V*-*i* polarization results in Figure 2.3 indicated that the impedances should be nearly independent of current, we also performed impedance measurements as a function of voltage on these cells and again found the results to be almost independent of the applied voltage over the range from -1 V to 1 V.

Because the performance of infiltrated electrodes depends on the calcination temperature [42,47,48], symmetric cells were also prepared with the LSF calcined to 1373 K for 4 h. Impedance spectra were again obtained in air from 873 to 973 K, with the spectra at 973 K shown in Figure 2.7. Although the impedances on each of these cells were significantly higher, the relative performance as a function of the electrolyte was the same, with the ScSZ cell being the best with an R_p of 0.54 Ω cm^2, while the YSZ and YAZ cells showed significantly higher R_p of 0.91 Ω cm^2 and 2.67 Ω cm^2, respectively.

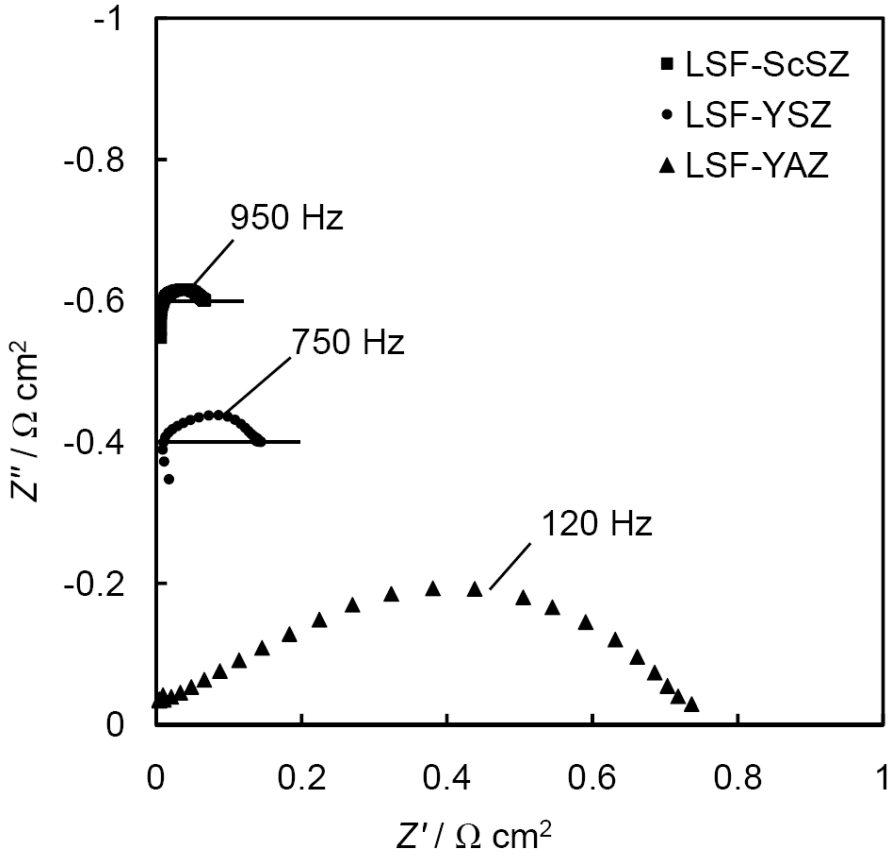

Figure 2.6 Electrochemical impedance spectra of LSF-SZ symmetric cells with different electrolyte scaffolds after calcination to 1123 K, measured at 973 K in ambient air and open circuit conditions. Squares – ScSZ, circles – YSZ, triangles –YAZ.

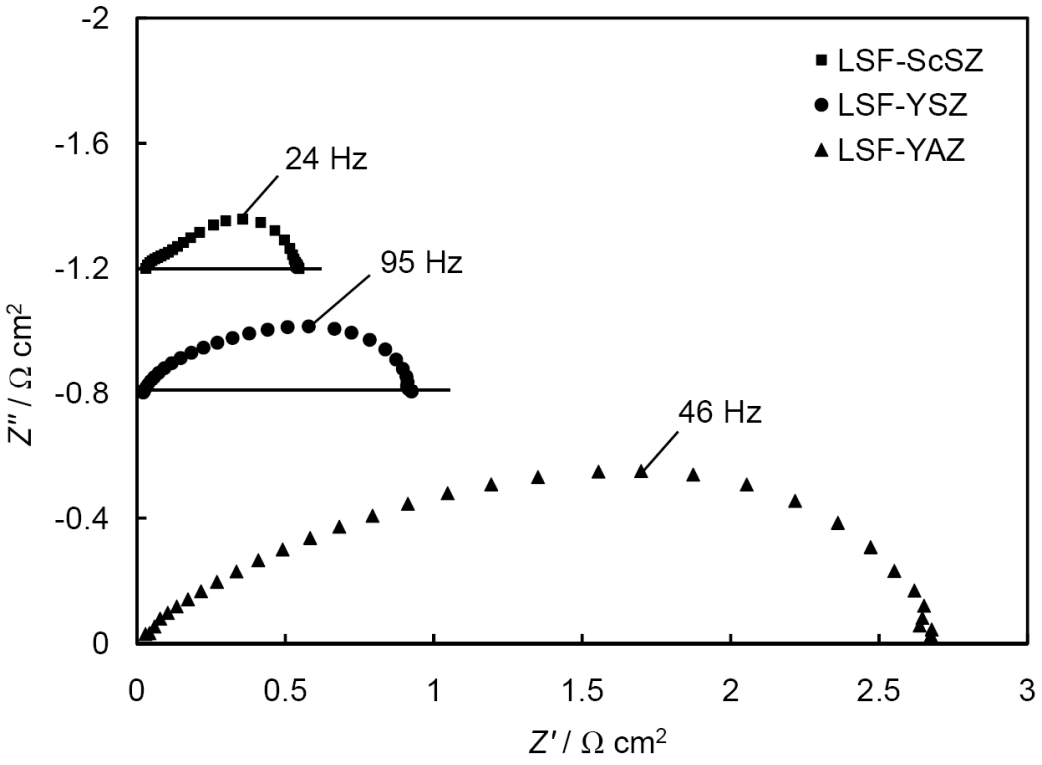

Figure 2.7 Electrochemical impedance spectra of symmetric cells with different electrolyte scaffolds after calcination to 1373 K, measured at 973 K in ambient air and open circuit conditions. Squares – ScSZ, circles – YSZ, triangles – YAZ.

Two modeling studies have predicted that the polarization resistance of composite cathode should vary as the inverse square-root of the ionic conductivity of the electrolyte material [3,36]. Therefore, we have plotted the values of R_p that were obtained from the symmetric cells as a function of the ionic conductivity, with the results at 873 K, 923 K, and 973 K shown in Figures 2.8a)-c). For the LSF cells calcined at 1373 K, the dependence of R_p on ionic conductivity was very close to the expected inverse square-root value. There does not seem to be a need to invoke other factors, such as differences in catalytic activity, to explain the relative performance of the cells made with these three electrolytes. However, for the LSF electrodes that were calcined at 1123 K, the electrode resistances varied with an almost inverse, first-order dependence on the ionic conductivity of the scaffold at each of the three temperatures. This result is perhaps biased by the poor performance of the cell made from YAZ. If factors in addition to ionic conductivity caused the performance of this cell to be worse, the dependence of R_p on ionic conductivity would be weaker. It is also possible that the electrode kinetics are not completely independent of the electrolyte material for cells heated to 1123 K.

It is interesting to consider the characteristic frequencies, ν_{char}, for the impedance data in Figures 2.4, 2.6, and 2.7. For the cells calcined at 1123 K, ν_{char} increases in the order YAZ < YSZ < ScSZ. For example, for the fuel cell data shown in Fig. 2.4, the characteristic frequency of the YAZ cell was 190 Hz, while those of the YSZ and ScSZ cells were 400 Hz and 1.2 kHz, respectively. A similar trend can be seen in Fig. 2.6 for the corresponding symmetric cells. While models, such as the Tanner-Virkar model [3] and the ALS model [27], did not calculate the effect of the electrolyte conductivity on

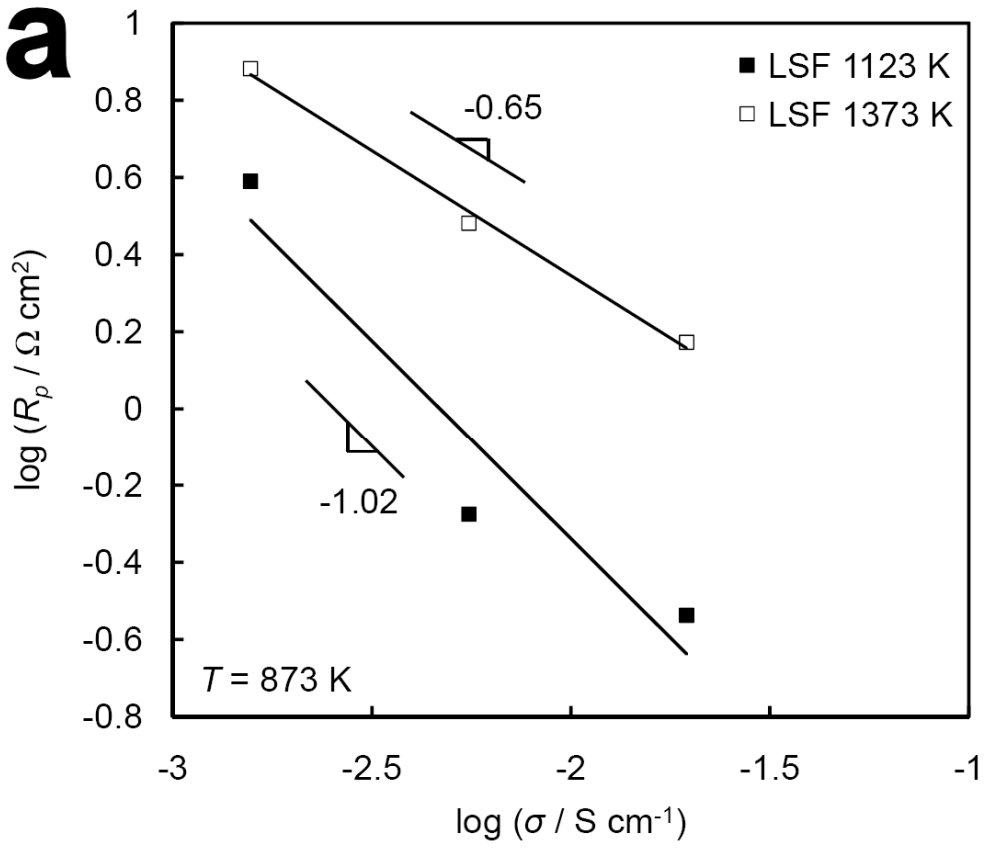

Figure 2.8a Log-log plot of the ionic conductivity of the electrolyte material vs the polarization resistance of the cathode symmetric cells calcined to either 1123 K (closed symbols) or 1373 K (open symbols) tested at open circuit conditions at 873 K.

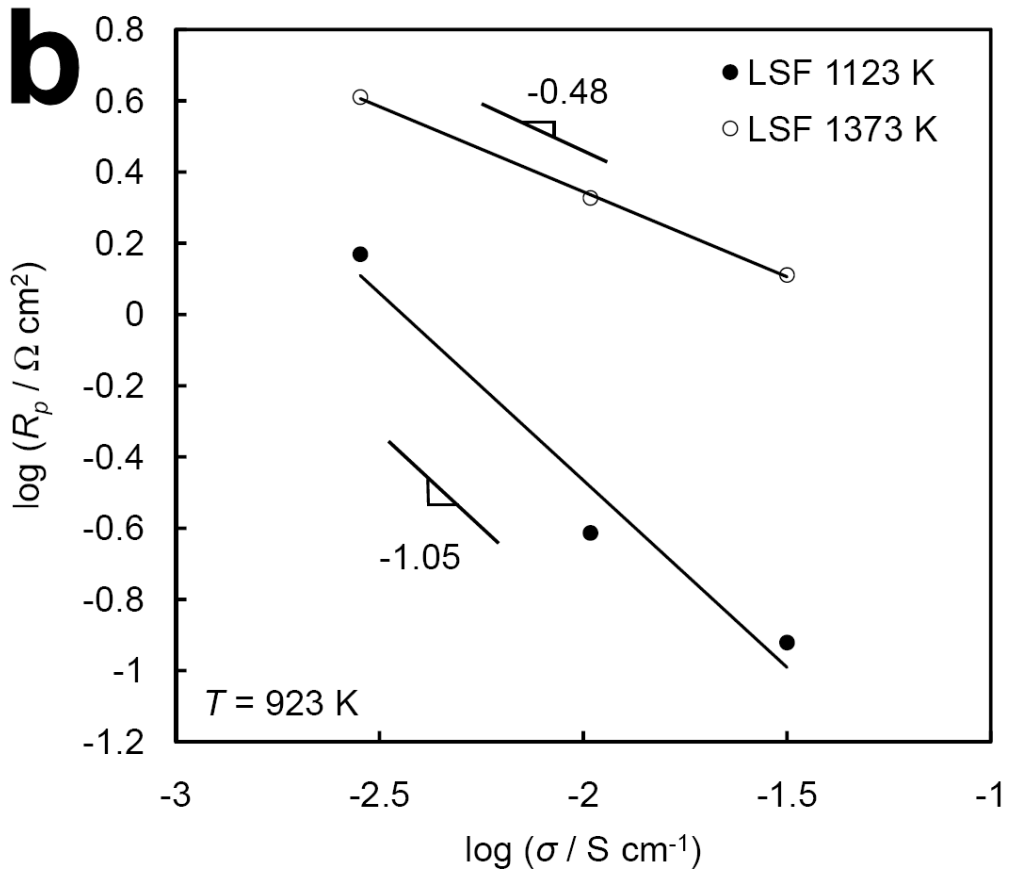

Figure 2.8b Log-log plot of the ionic conductivity of the electrolyte material vs the polarization resistance of the cathode symmetric cells calcined to either 1123 K (closed symbols) or 1373 K (open symbols) tested at open circuit conditions at 923 K.

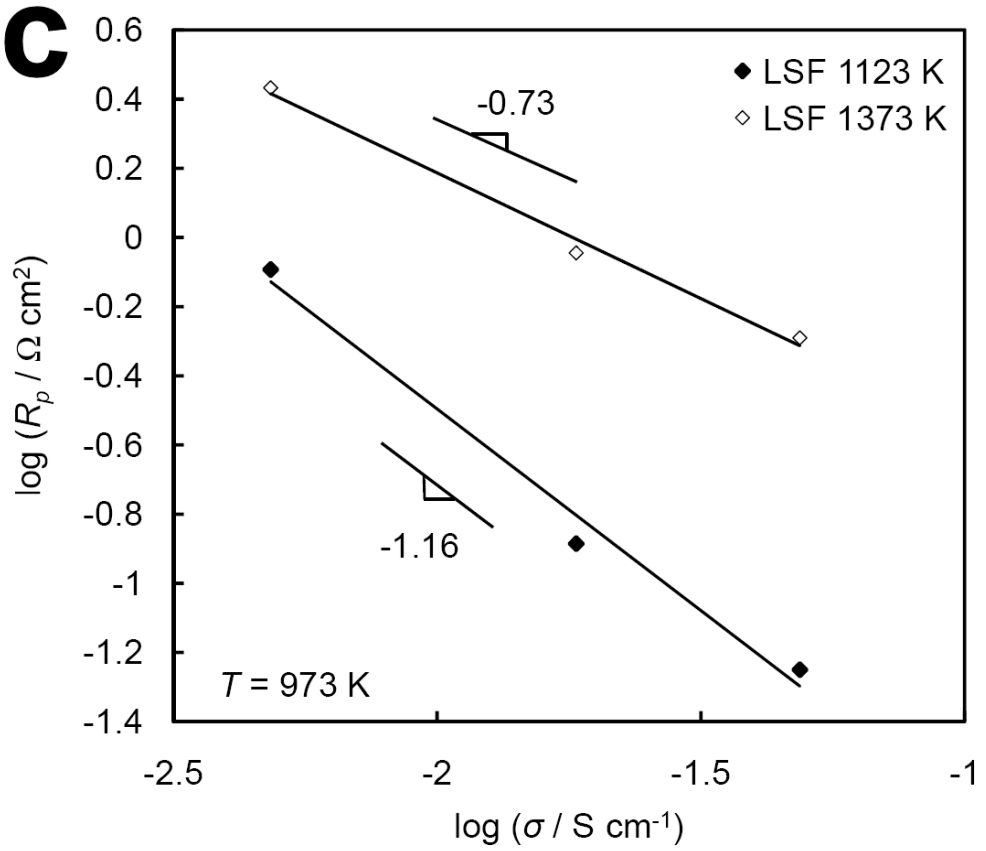

Figure 2.8c Log-log plot of the ionic conductivity of the electrolyte material vs the polarization resistance of the cathode symmetric cells calcined to either 1123 K (closed symbols) or 1373 K (open symbols) tested at open circuit conditions at 973 K.

the characteristic frequency, Bidrawn, *et al.* did show that v_{char} increased with decreasing R_p for electrodes with structures similar to those we have examined [36]. Although v_{char} for cells calcined to 1373 K (Fig. 2.7) did not show a uniform trend with the ionic conductivity of the electrolyte, the strong current dependence of the electrode impedances after high-temperature calcination makes interpretation of these results more difficult.

2.4 Discussion

The key finding of this study is that the ionic conductivity of the electrolyte used in composite cathodes has a large impact on the performance of these electrodes. More specifically, we have shown that the polarization resistance of composite electrodes decreases as the ionic conductivity of the electrolyte used in the composite increases, when all other materials properties (such as the catalytic activity, microstructure, reducibility, surface energy, etc.) are held constant. In contrast to doped ceria, none of the three electrolyte materials in this study is likely to possess significant activity towards oxygen reduction reaction, thus eliminating the possibility of electrode performance enhancement due to catalytic activity.

One implication of the finding that the performance scales with the ionic conductivity is that at least some of the enhancement observed when substituting YSZ with doped ceria in electrode composites arises from the increased ionic conductivity of the doped ceria. Of course, using a ceria-based composite can be advantageous in other ways. For example, doped ceria can prevent solid-state reactions between YSZ and

LSCo ($La_{1-x}Sr_xCoO_3$) [42,49-51]. Ceria could also enhance performance through enhanced catalytic activity, since it is known to be a very good oxidation catalyst [52,53].

Another implication of our results is related to low-temperature SOFCs. ScSZ is often proposed as a promising electrolyte material for anode-supported thin-electrolyte fuel cells operating at temperatures below 873 K [12,54]. The results of the present study demonstrate that a significant fraction of the enhanced performance of cells based on ScSZ could be due to enhanced performance of composite electrodes made from ScSZ. For very thin electrolytes, electrode losses frequently dominate. Improved ionic conductivity of the electrolyte within the composite electrodes could still affect the overall cell performance.

While all of the data in the present study was taken on composites of LSF and the electrolyte material, it is likely that the conclusions will be general for any perovskite so long as its ionic conductivity is less than that of the electrolyte. If electronically conductive materials could be found with ionic conductivities that were higher than that of the electrolyte, there would be no need for ionic conduction within the electrolyte phase. A corollary of this is that one should expect enhanced electrode performance following the addition of any material with high ionic conductivity to a composite cathode. Obviously, the structure of the composite is still important and one can only take advantage of a materials ionic conductivity if it is possible for that material to transport ions to the electrolyte [48].

2.5 Conclusions

The performance of SOFC composite cathodes made from an electronically conductive perovskite and the electrolyte material is shown to depend on the ionic conductivity of the electrolyte. The dependence of the electrode resistance on the ionic conductivity of the electrolyte phase was found to be between to the power of -0.5 and -1. The results suggest that enhanced electrode performance can be achieved by incorporating a material with high ionic conductivity within composite electrodes.

2.6 References

1. S. Singhal and K. Kendall (Eds.), *High temperature solid oxide fuel cells: fundamentals, design and applications*, Elsevier, Oxford (2003).
2. N.G. Minh and T. Takahashi (Eds.), *Science and technology of ceramic fuel cells*, Elsevier, Amsterdam (1995).
3. C. W. Tanner, K.-Z. Fung, and A. V. Virkar, The effect of porous composite electrode structure on solid oxide fuel cell performance: Part I - theoretical analysis, *J. Electrochem. Soc.*, **144**, 21 (1997).
4. Y. Ji, J. A. Kilner and M. F. Carolan, Electrical properties and oxygen diffusion in yttria-stabilised zirconia (YSZ)-$La_{0.8}Sr_{0.2}MnO_{3\pm\delta}$ (LSM) composites, *Solid State Ionics*, **176**, 937 (2005).
5. T. Suzuki, M. Awano, P. Jasinski, V. Petrovsky, and H. U. Anderson, Composite (La, Sr)MnO_3–YSZ cathode for SOFC, *Solid State Ionics,* **177**, 2071 (2006).

6. M. J. L. Østergård, C. Clausen, C. Bagger and M. Mogensen, Manganite-zirconia composite cathode for SOFC: influence of structure and composition, *Electrochim. Acta*, **40**[12], 1971 (1995).
7. M. J. Jørgensen, S. Primdahl, C. Bagger, and M. Mogensen, Effect of sintering temperature on microstructure and performance of LSM–YSZ composite cathodes, *Solid State Ionics,* **139**, 1 (2001).
8. M. J. Jørgensen and M. Mogensen, Impedance of solid oxide fuel cell LSM/YSZ composite cathodes, *J. Electrochem. Soc.,* **148**, A433-A442 (2001).
9. J. Mertens, V. A. C. Haanappel, C. Wedershoven, and H. P. Buchkremer, Sintering behavior of (La, Sr)MnO_3 type cathodes for planar anode-supported SOFCs, *J. Fuel Cell Sci. Technol.,* **3**[4], 415 (2006)
10. Y. Huang, K. Ahn, J. M. Vohs, and R. J. Gorte, Characterization of Sr-doped $LaCoO_3$-YSZ composites prepared by impregnation methods, *J. Electrochem. Soc.,* **151**[10], A1592 (2004).
11. K. Yamahara, T. Z. Sholklapper, C. P. Jacobson, S. J. Visco, and L. C. De Jonghe, Ionic conductivity of stabilized zirconia networks in composite SOFC electrodes, *Solid State Ionics*, **176**, 1359 (2005).
12. K. Yamahara, C. P. Jacobson, S. J. Visco, and L. C. De Jonghe, Thin film SOFCs with cobalt-infiltrated cathodes, *Solid State Ionics,* **176**, 275 (2005).
13. A. Selimovic, M. Kemm, T. Torisson, and M. Assadi, Steady state and transient thermal stress analysis in planar solid oxide fuel cells, *J. Power Sources,* **145**, 463 (2005).

14. G. Anandakumar, N. Li, A. Verma, P. Singh, and J.-H. Kim, Thermal stress and probability of failure analyses of functionally graded solid oxide fuel cells, *J. Power Sources,* **195**, 6659 (2010).

15. E. Ivers-Tiffée, A. Weber, and D. Herbstritt, Materials and technologies for SOFC-components, *J. Eur. Ceram. Soc.,* **21**, 1805 (2001).

16. S. P. Simner, J. F. Bonnett, N. L. Canfield, K. D. Meinhardt, J. P. Shelton, V. L. Sprenkle, and J. W. Stevenson, Development of lanthanum ferrite SOFC cathodes, *J. Power Sources,* **113**, 1 (2003).

17. M. Søgaard, P. V. Hendriksen, and M. Mogensen, Oxygen nonstoichiometry and transport properties of strontium substituted lanthanum ferrite*, J. Solid State Chem., **180**[4], 1489 (2007).*

18. J. Mizusaki, M. Yoshihiro, S. Yamauchi, and K. Fueki, Nonstoichiometry and defect structure of the perovskite-type oxides $La_{1-x}Sr_xFeO_{3-\delta}$, *J. Solid State Chem.,* **58**, 257 (1985).

19. Y. Huang, J. M. Vohs, and R. J. Gorte Fabrication of Sr-doped $LaFeO_3$ YSZ composite cathodes, *J. Electrochem. Soc.,* **151**[4], A646 (2004).

20. Z. Lu, J. Hardy, J. Templeton, and J. Stevenson, New insights in the polarization resistance of anode-supported solid oxide fuel cells with $La_{0.6}Sr_{0.4}Co_{0.2}Fe_{0.8}O_3$ cathodes, *J. Power Sources,* **196**, 39 (2011).

21. W. G. Wang and M. Mogensen, High-performance lanthanum-ferrite-based cathode for SOFC, *Solid State Ionics,* **176**, 457 (2005).

22. A. Mai, V. A. C. Haanappel, S. Uhlenbruck, F. Tietz, and D. Stöver, Ferrite-based perovskites as cathode materials for anode-supported solid oxide fuel cells: Part I. Variation of composition, *Solid State Ionics,* **176**[15-16], 1341 (2005).

23. S. P. Jiang, A comparison of O_2 reduction reactions on porous (La,Sr)MnO_3 and (La,Sr)(Co,Fe)O_3 electrodes, *Solid State Ionics*, **146**, 1 (2002).

24. J. M. Serra, V. B. Vert, M. Betz, V. A. C. Haanappel, W. A. Meulenberg, and F. Tietz, Screening of A-Substitution in the system $A_{0.68}Sr_{0.3}Fe_{0.8}Co_{0.2}O_{3-\delta}$ for SOFC cathodes, *J. Electrochem. Soc.*, **155**, B207 (2008).

25. M. Shah and S.A. Barnett, Solid oxide fuel cell cathodes by infiltration of $La_{0.6}Sr_{0.4}Co_{0.2}Fe_{0.8}O_{3-\delta}$ into Gd-doped ceria, *Solid State Ionics,* **179**[35-36], 2059 (2008).

26. Y. Ren, R. Küngas, R. J. Gorte, and C. Deng, The effect of A-site cation (Ln = La, Pr, Sm) on the crystal structure, conductivity and oxygen reduction properties of Sr-doped ferrite perovskites, *Solid State Ionics*, **212**, 47 (2012).

27. S. B. Adler, J. A. Lane, and B. C. H. Steele, Electrode kinetics of porous mixed-conducting oxygen electrodes, *J. Electrochem. Soc*., **143**, 3554 (1996).

28. V. V. Kharton, F. M. B. Marques, and A. Atkinson, Transport properties of solid oxide electrolyte ceramics: a brief review, *Solid State Ionics*, **174**, 135 (2004).

29. A. Atkinson, S. Barnett, R. J. Gorte, J. T. S. Irvine, A. J. McEvoy, M. Mogensen, S. C. Singhal, and J. Vohs, Advanced anodes for high-temperature fuel cells, *Nature Materials*, **3**, 17 (2004).

30. H. Timmermann, D. Fouquet, A.Weber, E. Ivers-Tiffée, U. Hennings, and R. Reimert, Internal Reforming of Methane at Ni/YSZ and Ni/CGO SOFC Cermet Anodes, *Fuel Cells*, **6**, 307 (2006).

31. M. Cimenti, V. Alzate-Restrepo, and J. M. Hill, Direct utilization of methanol on impregnated Ni/YSZ and Ni–$Zr_{0.35}Ce_{0.65}O_2$/YSZ anodes for solid oxide fuel cells, *J. Power Sources*, **195**, 4002 (2010).

32. C. Lu, S. An , W.L. Worrell, J.M. Vohs, and R.J. Gorte, Characterization of Cu-CeO_2 direct hydrocarbon anodes in a solid oxide fuel cell with lanthanum gallate electrolyte, *Solid State Ionics,* **175**, 47 (2004).

33. H. Sumi, K. Ukai, Y. Mizutani, H. Mori, C.-J. Wen, H. Takahashi, and O. Yamamoto, Performance of nickel-scandia-stabilized zirconia cermet anodes for SOFCs in 3% H_2O-CH_4, *Solid State Ionics*, **174**, 151 (2004).

34. E. Perry Murray and S.A. Barnett, (La,Sr)MnO_3-(Ce,Gd)O_{2-x} composite cathodes for solid oxide fuel cells, *Solid State Ionics,* **143**, 265 (2001).

35. Z. Wang, M. Cheng, Y. Dong, M. Zhang, and H. Zhang, Investigation of $LSM_{1.1}$–ScSZ composite cathodes for anode-supported solid oxide fuel cells, *Solid State Ionics*, **176**, 2555 (2005).

36. F. Bidrawn, R. Küngas, J. M. Vohs, and R. J. Gorte, Modeling impedance response of SOFC cathodes prepared by infiltration, *J. Electrochem. Soc.*, **158**[5], B514 (2011).

37. G. Zhou, P. R. Shah, T. Montini, P. Fornasiero, and R. J. Gorte, Oxidation enthalpies for reduction of ceria surfaces, *Surface Sci.,* **601**, 2512 (2007).

38. S. Hilaire, X. Wang, T. Luo, R. J. Gorte, and J. Wagner, A comparative study of water-gas-shift reaction over ceria supported metallic catalysts, *Appl. Cat. A* **258**, 271 (2004).

39. J.-S. Kim, V. V. Nair, J. M. Vohs and R. J. Gorte, A study of the methane tolerance of LSCM–YSZ composite anodes with Pt, Ni, Pd and ceria catalysts, *Scripta Mat.,* **65**, 90 (2011).

40. E. Aneggi, M. Boaro, C. de Leitenburg, G. Dolcetti, and A Trovarelli, Insights into the redox properties of ceria-based oxides and their implications in catalysis, *J. Alloys Comp.*, **408–412**, 1096 (2006).

41. J. M. Vohs and R. J. Gorte, High-performance SOFC cathodes prepared by infiltration, *Adv. Mat.,* **21**[9], 943 (2009).

42. R. Küngas, F. Bidrawn, J. M. Vohs, and R. J. Gorte, Doped-ceria diffusion barriers prepared by infiltration for solid oxide fuel cells, *Electrochem. Solid-State Lett.,* **13**, B87 (2010).

43. O. Yamamoto, T. Kawahara, K. Kohno, Y. Takeda, and N. Imanshi, in *Solid State Materials*, S. Radhakrishna and A. Daud, (Eds,), p. 372, Narosa Publishing House, New Delhi (1991).

44. M. Boaro, J. M. Vohs, and R. J. Gorte, Synthesis of highly porous yttria-stabilized zirconia by tape-casting methods, *J. Am. Ceram. Soc.,* **86**[3], 395 (2003).

45. H. Kim, C. da Rosa, M. Boaro, J. M. Vohs, and R. J. Gorte, Fabrication of highly porous yttria-stabilized zirconia by acid leaching nickel from a nickel-yttria-stabilized zirconia cermet, *J. Am. Ceram. Soc.*, **85**, 1473 (2002).

46. J. H. Joo, G. M. Choi, Electrical conductivity of scandia-stabilized zirconia thin film, *Solid State Ionics*, **179**, 1209 (2008).

47. F. Bidrawn, G. Kim, N. Aramrueang, J. M. Vohs, and R. J. Gorte, Dopants to enhance SOFC cathodes based on Sr-doped $LaFeO_3$ and $LaMnO_3$, *J. Power Sources,* **195**[3], 720 (2010).

48. W. Wang, M. D. Gross, J. M. Vohs, and R. J. Gorte, The stability of LSF–YSZ electrodes prepared by infiltration, *J. Electrochem. Soc.,* **154**[5], B439 (2007).

49. M. Shiono, K. Kobayashi, T. L. Nguyen, K. Hosoda, T. Kato, K. Ota, and M. Dokiya, Effect of CeO_2 interlayer on ZrO_2 electrolyte/$La(Sr)CoO_3$ cathode for low-temperature SOFCs, *Solid State Ionics*, **170**, 1 (2004).

50. C. Rossignol, J. M. Ralph, J.-M. Bae, and J. T. Vaughey, $Ln_{1-x}Sr_xCoO_3$ (Ln=Gd, Pr) as a cathode for intermediate-temperature solid oxide fuel cells, *Solid State Ionics*, **175**, 59 (2004).

51. S. Uhlenbruck, T. Moskalewicz, N. Jordan, H.-J. Penkalla, and H. P. Buchkremer, Element interdiffusion at electrolyte–cathode interfaces in ceramic high-temperature fuel cells, *Solid State Ionics*, **180**, 418 (2009).

52. A. Trovarelli, *Catalysis by Ceria and Related Materials*, Imperial College Press, London (2002).

53. R. J. Gorte, Ceria in catalysis: from automotive applications to the water-gas shift reaction, *AIChE Journal*, **56**, 1126 (2010).

54. T. Suzuki, Z. Hasan, Y. Funahashi, T. Yamaguchi, Y. Fujishiro, and M. Awano, Impact of anode microstructure on solid oxide fuel cells, *Science,* **325**, 852 (2009).

Chapter 3. Restructuring Porous YSZ by Treatment in Hydrofluoric Acid for Use in SOFC Cathodes*

Summary

The structure of porous yttria-stabilized zirconia (YSZ) has been modified by infiltration with concentrated hydrofluoric acid (HF) for application in solid-oxide fuel cell (SOFC) electrodes. Dissolution and precipitation of the YSZ greatly increased the surface area of the porous YSZ and formed sheets and pillars of YSZ within the structure that were largely stable to calcination at 1373 K. Electrodes made by infiltration of 35-wt% (20 vol%) $La_{0.8}Sr_{0.2}FeO_3$ into the pore structure exhibited significantly lower impedances at 973 K, even after calcination to 1373 K.

3.1 Introduction

In solid oxide fuel cells (SOFC), the cathodes showing the best performance are usually composites of an electronically conductive oxide with a perovskite structure and the electrolyte [1]. For example, the standard material in SOFC that are based on yttria-stabilized zirconia (YSZ) electrolytes is a composite of YSZ and Sr-doped $LaMnO_3$ (LSM) [2,3]. In LSM-YSZ cathodes, the LSM provides electronic conductivity and catalytic activity for oxygen reduction, while the YSZ provides ion-conducting channels from the electrolyte into the electrode to increase the length of the three-phase boundary (TPB) [1]. The conventional method for preparing composite cathodes involves sintering

* This chapter was published as a research paper in the Journal of the American Ceramic Society, 94(7) (2011) 2220.

a powdered mixture of the conductive oxide and the electrolyte together with the dense electrolyte. With YSZ electrolytes, the best performance is achieved using sintering temperatures on the order of 1373 K [4]. This temperature is a compromise, high enough to form good ion-conducting channels by sintering the YSZ particles in the electrode to the electrolyte but low enough to avoid solid-state reactions between YSZ and the electronic conductor.

A new method for electrode fabrication has recently been developed in which the composite is formed by infiltration of the electronically conductive component into a porous layer of the electrolyte [5-16]. With composites prepared by infiltration, the high-temperature sintering step required to form the porous-dense-porous electrolyte scaffold and the low-temperature calcination step that is needed to form the perovskite structure after the infiltration of LSF are temporally separated. The higher temperatures used for the sintering of YSZ results in better ion-conducting channels from the electrolyte into the electrode and make the electrodes mechanically stronger [5]. Furthermore, the composites formed by infiltration do not have a random structure, so that sufficient conductivity can be achieved even when perovskite loadings below the normal percolation threshold of 30-vol% are used [8,17]. The non-random structure also causes the coefficients of thermal expansion (CTE) of the composite to be closer to that of YSZ scaffold than to the weighted average of the components [5,8].

$La_{0.8}Sr_{0.2}CoO_3$ (LSCo) and $La_{0.8}Sr_{0.2}FeO_3$ (LSF) are promising candidates for intermediate temperature SOFC cathodes and these electrodes are best formed using infiltration procedures [5,9,18-23]. However, previous studies using these materials have

indicated that the structure of both the electrolyte scaffold and the infiltrated perovskite strongly influences performance. For example, Huang, *et al*. prepared YSZ scaffolds using different pore formers to obtain scaffolds that had similar porosities but very different pore-size distributions and surface areas [21]. They showed that the impedance of an electrode formed by infiltration of LSCo into a YSZ scaffold with smaller pores and a higher surface area is much lower than that of an electrode formed by infiltration into a scaffold with larger pores and lower surface areas. These findings agree with modeling studies conducted by Tanner *et al.* [1], which also suggest that the structure of the YSZ component of composite electrodes should influence performance. Similarly, other studies have indicated that the electrode performance correlates with the surface area and structure of the infiltrated particles [14,24,25]. Increases in the impedance of infiltrated LSF-YSZ electrodes with time or increasing calcination temperature correlated with losses in the surface areas [25]. Furthermore, attempts to improve the performance of infiltrated LSF-YSZ electrodes through the addition of a wide range of catalytic or ion-conducting additives showed no improvement for the case where the LSF was prepared at low temperatures and had a high surface area, whereas a significant decrease in the electrode impedance was observed when the same additives were infiltrated into composites formed at high temperatures with a low surface area [24].

These results suggest that improvements could be made in electrodes through modifications in either the structure of the infiltrated particles or of the pores in the scaffold. While modifying the structure of the infiltrated particles (e.g. through preparation of nanoparticles) is relatively easy, the challenge in this approach is in

maintaining that structure at the relatively high operating temperatures of SOFC. Regarding the YSZ scaffold pore structure, the challenge is to maintain the smaller pores while still using calcination temperatures sufficient to fully sinter the scaffold to the electrolyte.

In this chapter, an approach will be described for modifying a YSZ scaffold through a treatment with hydrofluoric acid (HF) that partially dissolves and then precipitates the YSZ within the pores. The process significantly increases the surface area of the scaffold without appearing to affect the connectivity of the YSZ scaffold.

3.2 Experimental

The electrochemical cells used in this study were prepared from tri-layer, YSZ wafers, in which a 75±2-μm dense electrolyte disc was sandwiched between two 60-μm porous YSZ layers. The diameter of the dense part of each wafer was 1 cm but the diameter of the porous regions was only 0.67 cm. These wafers were used in making both symmetric cells and fuel cells.

The tri-layer wafers were fabricated by laminating three green tapes, made by tape-casting, followed by calcination at 1773 K for 4 h. Unlike in previous work [5-10,17,21,24-29], the tapes used here were based on organic solvents [30]. For the dense electrolyte layer, the tape-casting slurry was prepared by adding YSZ powder (Tosoh Corp., TZ-8Y) to a mixture of the solvent (ethanol and xylenes in a weight ratio 3:1) and a dispersant (Menhaden fish oil, Richard E. Mistler, Inc.). After ball milling this mixture for 12 h, binder (polyvinyl butyral B-98, Solutia Inc.) and plasticizers (polyethylene

glycol 400 MW, Alfa Aesar; benzyl butyl phthalate, Aldrich) were added, followed by another 24 h of ball-milling. The green tape was then cast onto a Mylar film using a tape casting system obtained from Richard E. Mistler, Inc. The tapes used in the porous layers were prepared in a similar manner, except that a different ethanol-to-xylene ratio (1:5) was used to accommodate the addition of the pore formers (either synthetic graphite (300 mesh, Alfa Aesar) or poly(methyl methacrylate) beads (PMMA, Scientific Polymer Products, MW = 540,000)). When PMMA was used as the pore former, the beads were stirred into the slurry immediately before tape casting to avoid loss of the beads by dissolving into the solvent.

The HF treatment for modifying the YSZ scaffold was carried out by simply infiltrating the porous scaffold with concentrated hydrofluoric acid (ACS reagent grade, MP Biomedicals) at room temperature. The solution was then left in the scaffold 1 h before being removed by washing with distilled water and ethanol.

LSF-YSZ electrodes in this study were fabricated by infiltrating the porous YSZ scaffolds with an aqueous solution consisting of $La(NO_3)_3 \cdot 6H_2O$ (Alfa Aesar, 99.9%), $Sr(NO_3)_2$ (Alfa Aesar, 99%), and $Fe(NO_3)_3 \cdot 9H_2O$ (Fisher, 98.4%) at a molar ratio of La:Sr:Fe = 0.8:0.2:1. Citric acid, in a 1:1 ratio with the metal cations, was used as a complexing agent in order to assist the formation of the perovskite phase at lower temperatures. Infiltration steps were followed by a 0.5-h heat treatment at 723 K to decompose the nitrates. This procedure was repeated until a loading of 35-wt% (20 vol%) LSF was achieved. (Note: The compositions in this paper are based on the total weight and volume of the electrode.) The LSF-YSZ composites were then calcined to either

1123 K or to 1373 K for 4 h. For fuel-cell measurements, 45-wt% (23 vol%) of ceria and 1-wt% (0.2 vol%) Pd were added to the porous layer opposite the LSF-YSZ composite using $Ce(NO_3)_3 \cdot 6H_2O$ (Alfa Aesar, 99.5%) and tetra-ammine palladium(II) nitrate solutions (Alfa Aesar, 99.9%), followed by calcination to 723 K.

For electrochemical testing, cells were attached to an alumina tube using a ceramic adhesive (Aremco, Ceramabond 552). Ag paste and Ag wire was used for current collection at both electrodes. Electrochemical impedance spectra were recorded using a Gamry Instruments potentiostat in the frequency range of 0.1 Hz to 100 kHz and with an AC perturbation of 5 mA, with the cathodes being subject to ambient air and anodes to 3% humidified H_2. All of the impedances of symmetric cells in this paper have been divided by two to account for there being two electrodes.

Surface areas were obtained from BET isotherms measured on 3 × 3 × 6 mm slabs, prepared from the same slurries that were used in the tape-casting process for the porous YSZ scaffolds. The BET isotherms were measured using Kr adsorption at 78 K. Porosities of the YSZ scaffolds were calculated from the weight changes in the slabs after saturation in water but ranged from 66 to 70% for each of the samples used here. X-ray diffraction patterns were measured with a Rigaku X-ray spectrometer using Cu K_α radiation in the 2θ range of 20 to 40°. FEI Quanta FEG ESEM scanning electron microscope (SEM) with energy-dispersive x-ray analysis (EDX) capability was used to determine the microstructure and elemental composition of prepared cells.

3.3 Results and discussion

Figure 3.1 shows a series of SEM micrographs of the various YSZ scaffolds used in this work. Figure 3.1a) is a low-magnification image of the unmodified YSZ prepared with graphite pore formers. The scaffold is uniform and exhibits a good interface with the dense electrolyte layer. At higher magnification, Figure 3.1b), the "sponge-like" character of this scaffold is observed, with characteristic pore dimensions between 1 and 3 μm. The effect of using the larger PMMA pore former is seen in Figure 3.1c). The pores in this material are spherical and nearly 30 μm in size. As discussed in previous publications [5,21,28], the spherical shape of the pores is due to the spherical shape of the PMMA that was added to the tape-casting slurry. The size of the voids is somewhat smaller than that of the initial PMMA beads due to shrinkage of the YSZ during sintering [28].

The effect of treating the porous YSZ, made using graphite pore formers, with concentrated HF for 1 h at room temperature is shown in Figure 3.1d) and 3.1e). The sample in these images was heated in air to 823 K to remove any residual fluorine. The overall structure remained stable but the entire pore network was changed. Sheet and pillar like structures are observed, with a characteristic length scale of less than 100 nm. EDX analysis on these formed structures was performed. It was found that the atomic ratio of Zr : Y to be 14.7 : 85.3, which is very close to the nominal 16 : 84 ratio expected for 8YSZ. XRD analysis on bulk HF-treated samples revealed no evidence of the tetragonal zirconia phase that would be expected if selective leaching of Y was occurring during the HF-treatment. However, due to the inherent limitations of EDX and XRD,

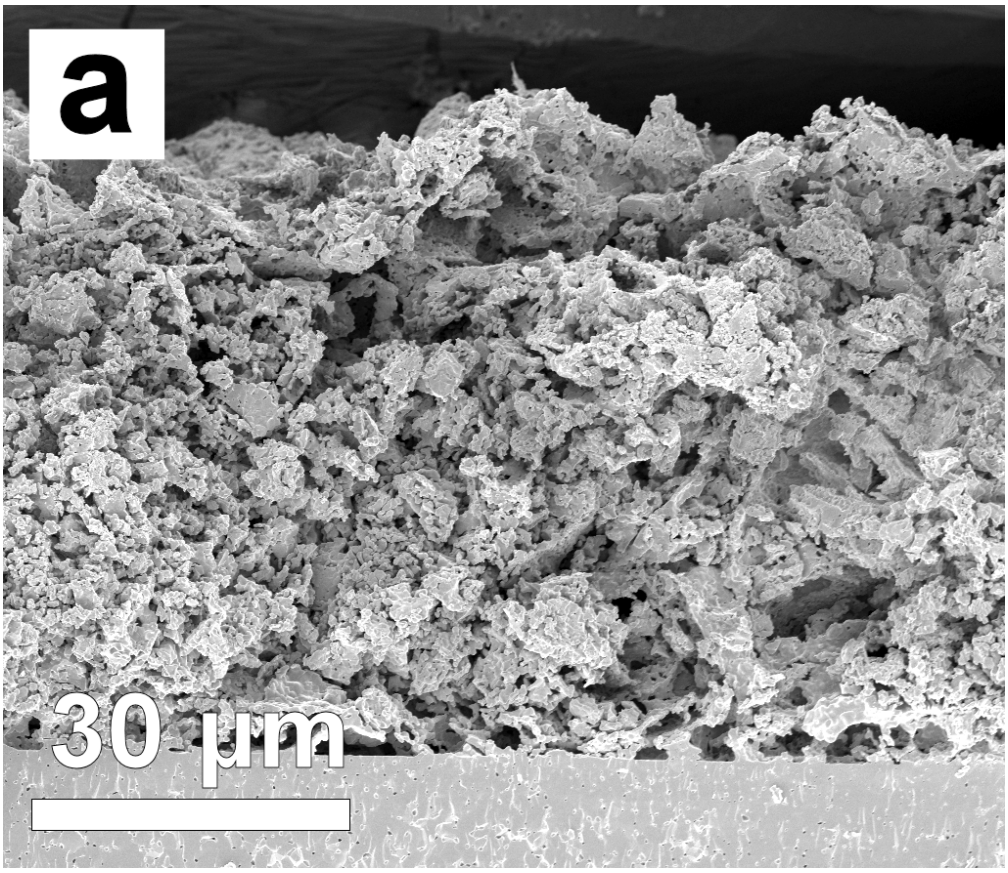

Figure 3.1a SEM images of porous YSZ scaffolds: a low magnification image of the graphite-prepared YSZ before HF treatment.

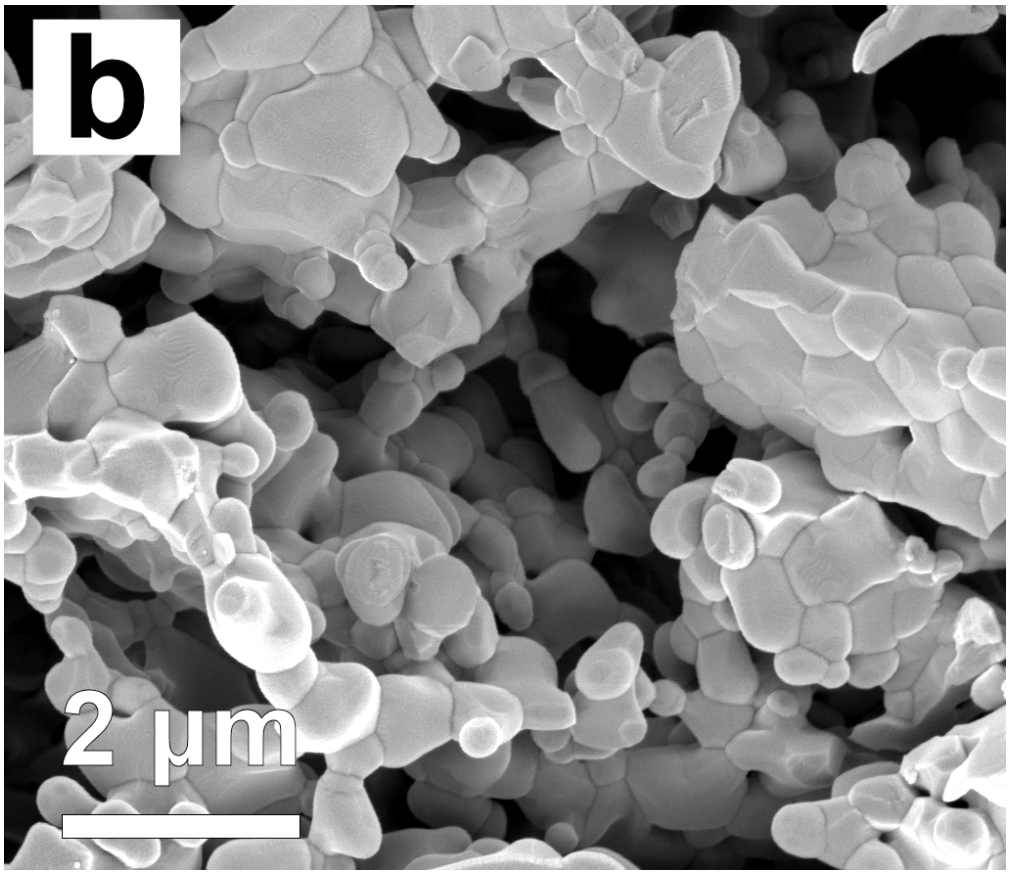

Figure 3.1b SEM images of porous YSZ scaffolds: a high magnification image of the sample in a).

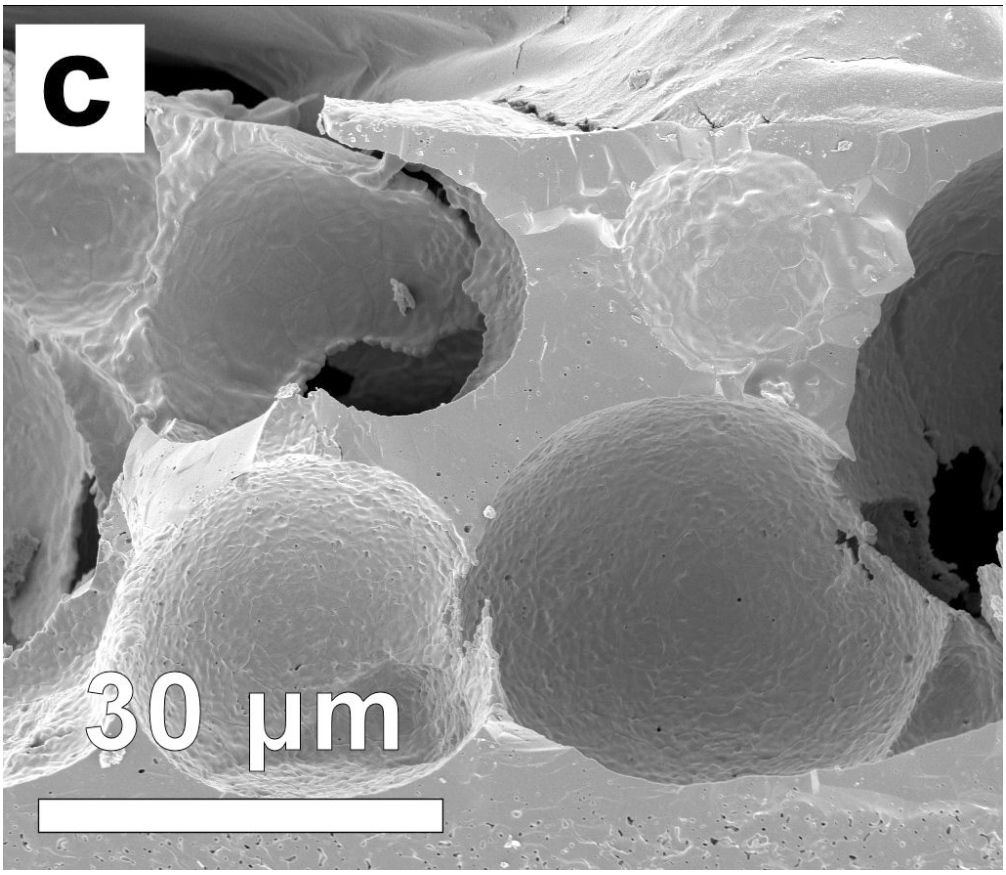

Figure 3.1c SEM images of porous YSZ scaffolds: a low magnification image of the PMMA-prepared YSZ structure.

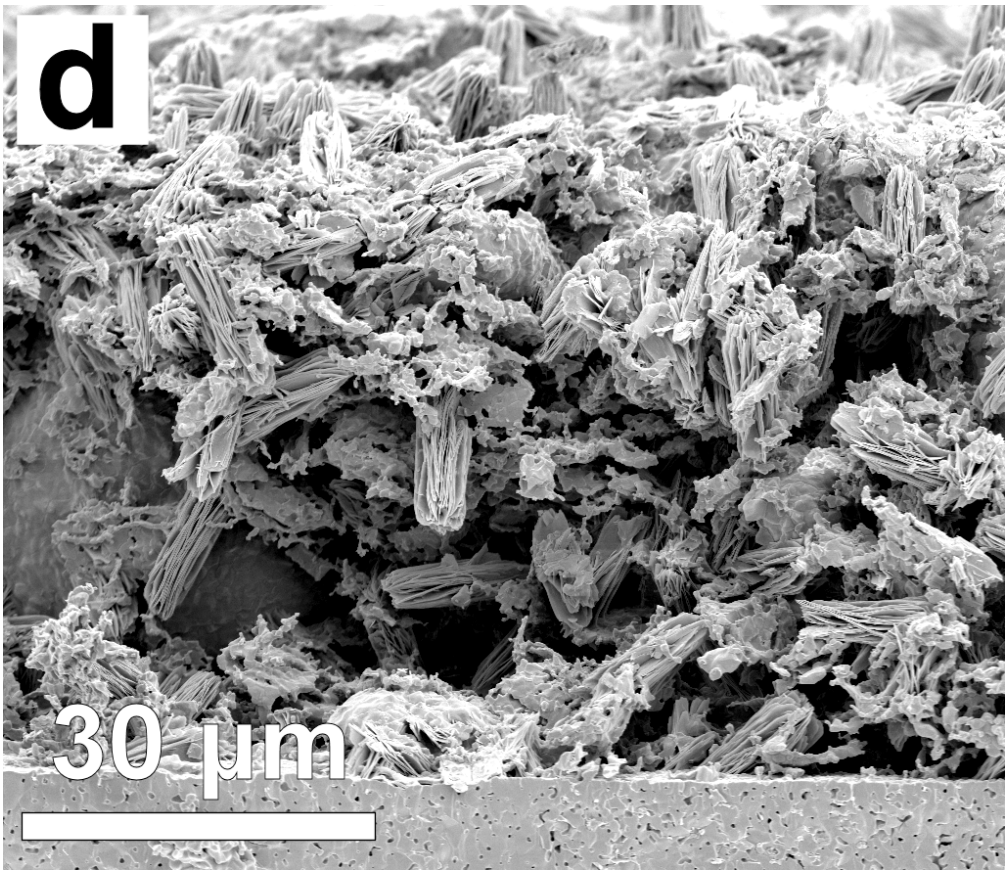

Figure 3.1d SEM images of porous YSZ scaffolds: a low magnification image of the graphite-prepared YSZ after HF treatment.

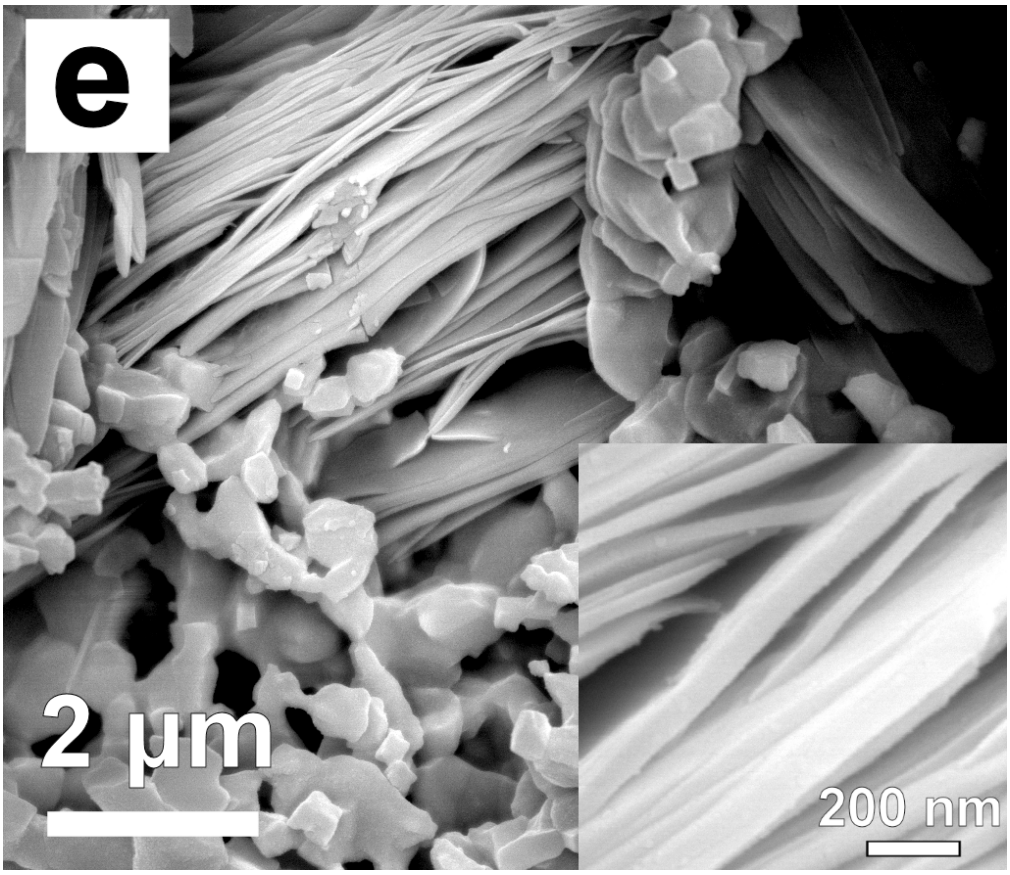

Figure 3.1e SEM images of porous YSZ scaffolds: a high magnification image of the sample in d).

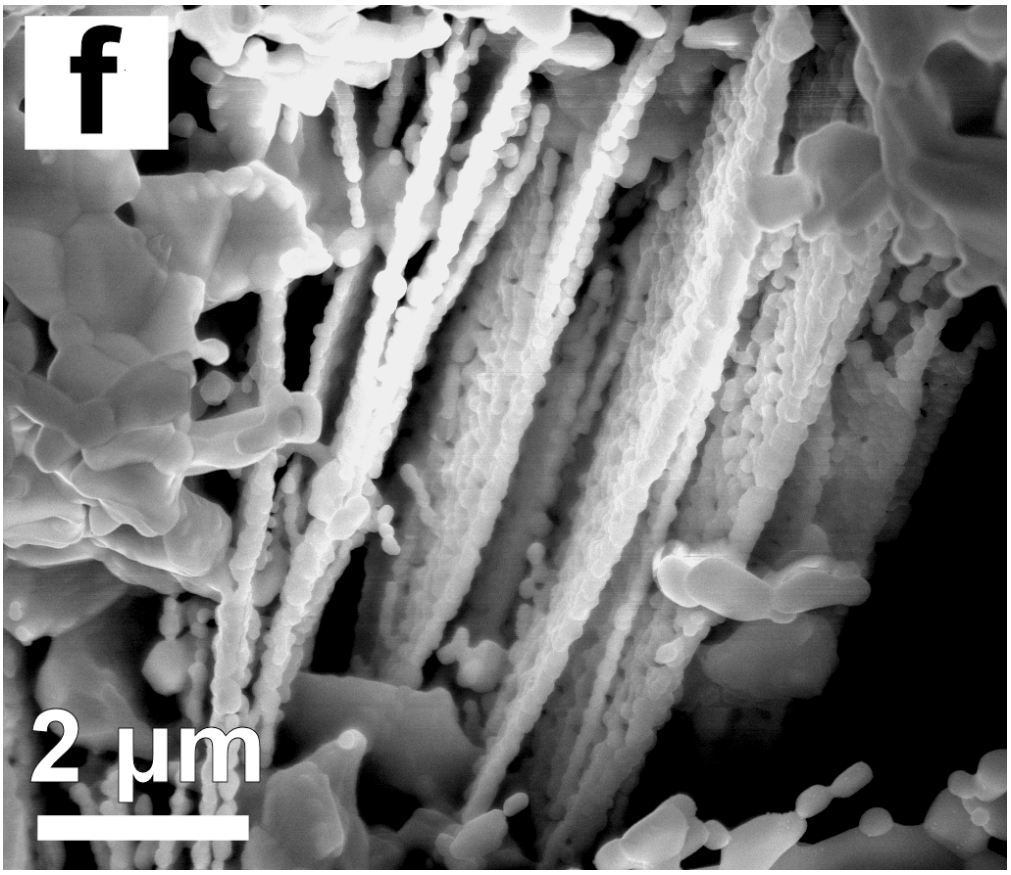

Figure 3.1f SEM images of porous YSZ scaffolds: an image of the sample in e) after 4h treatment at 1373 K.

selective Y leaching cannot be completely ruled out.

The treated structure was also reasonably stable. The image in Figure 3.1f) was taken on a sample that had been heated in air at 1373 K for 4 h. The sheets and pillars are still observed after this treatment. The BET surface areas for these samples are reported in Table 3.1. When graphite was used as the pore former, the specific surface area was 0.48 m^2/g. This low specific surface area demonstrates that there is no microporosity in the YSZ scaffold. The pore size that would be calculated for a 70% porous, YSZ scaffold with uniform cylindrical pores and this specific surface area is 2.8 μm [7], which is similar to the characteristic size of the channels in Figure 3.1a). The specific surface area of the scaffold prepared with PMMA was much lower, 0.04 m^2/g, again consistent with the much larger pores. The HF treatment to the YSZ prepared with graphite resulted in a large increase in the surface area. The specific surface area was 2.1 m^2/g after heating to 823 K and was still 0.83 m^2/g after 1373 K.

Table 3.1. BET specific surface areas (m^2/g) of the samples made using graphite as the pore former for the YSZ scaffold. (HF)YSZ is the HF-treated sample.

Sample		YSZ	(HF)YSZ	YSZ + 35% LSF	(HF)YSZ + 35% LSF
Calcination Temperature	1123 K	0.48	1.80	1.97	1.82
	1373 K	0.48	0.83	0.30	0.48

The effect of the scaffold on electrode performance is shown in Figure 3.2. The data in this figure were obtained at 973 K in air on symmetric cells prepared by infiltration of 35-wt% LSF. All impedances were divided by two to account for the two identical electrodes. A comparison of the performance of the cells made with graphite-prepared YSZ, with and without HF treatment, is given in Figure 3.2a). The ohmic losses, indicated by the high-frequency intercept with the real axis, were the same in both cells, 0.18 Ω cm^2, and very close to half the value expected for a 75-μm YSZ electrolyte. Although the non-ohmic losses, determined from the lengths of the arcs in the Cole-Cole plot, were very good for both cells, the cell with the HF-treated scaffolds was superior, with an impedance of 0.07 Ω cm^2, compared to an impedance of 0.13 Ω cm^2 on the untreated cell.

While the impedance observed on the LSF-infiltrated electrode prepared with the untreated YSZ would be acceptable for most applications, previous work has shown that the impedances increase with time or increasing calcination temperature because of coarsening of the infiltrated LSF [24.25]. It has been reported that heating infiltrated, LSF-YSZ composites to 1373 K had a similar effect on LSF structure as operation for several thousand hours at 973 K [25]. Figure 3.2b) shows impedance data at 973 K from cells made by infiltration of LSF into YSZ scaffolds prepared with graphite pore formers, both HF treated and untreated, and PMMA pore formers, after calcination of the LSF to 1373 K for 4 h. The ohmic losses on all three cells were unchanged and remain the same as that expected for the YSZ electrolyte, indicating that there are no solid state reactions between LSF and YSZ [22]; however, the effect of YSZ pore structure on the non-ohmic

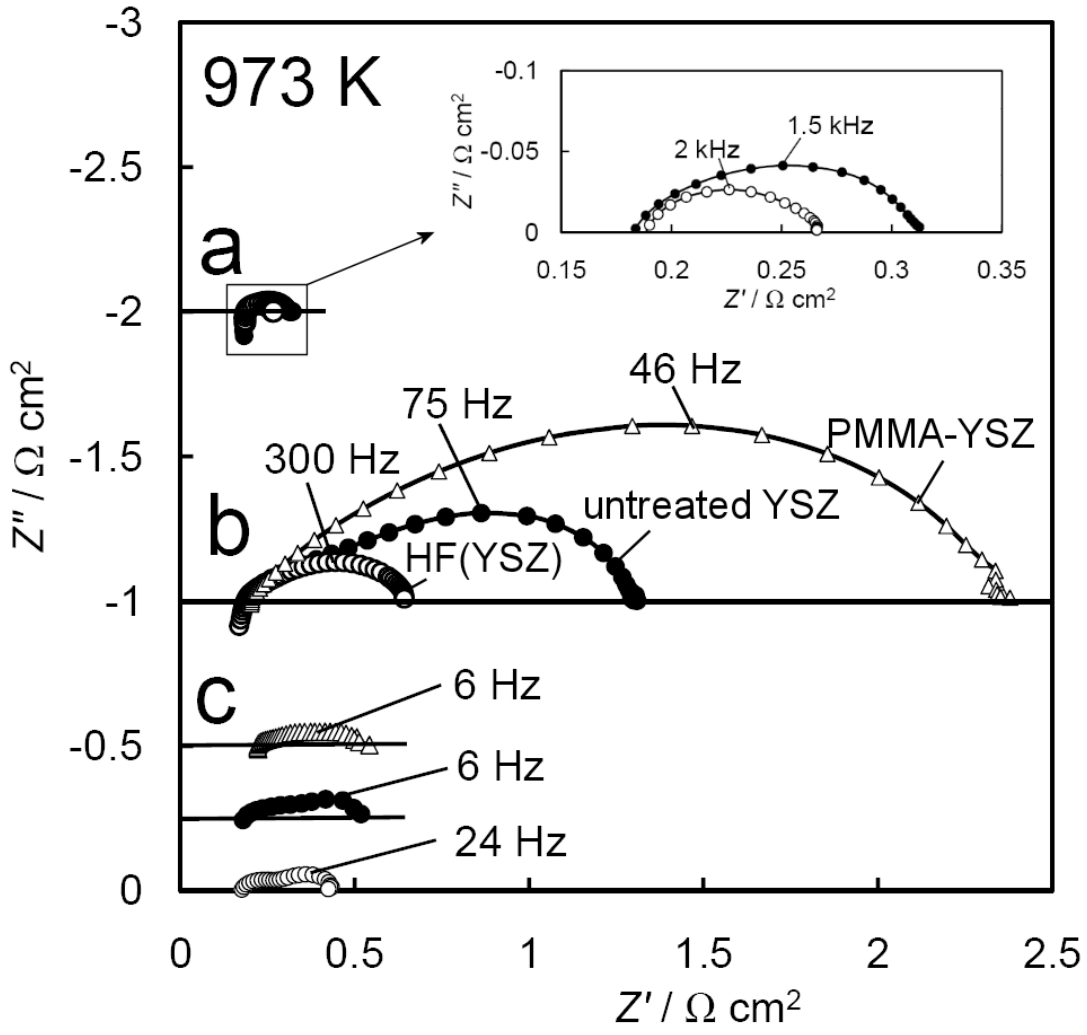

Figure 3.2 Electrochemical impedance spectra of LSF-YSZ symmetric cells at 973 K: a) At open circuit, after calcination of the composites to 1123 K; b) at open circuit, after calcination of the composites to 1373 K; c) at a current density of 400 mA/cm^2, after calcination to 1373 K. The open symbols indicate HF-treated YSZ, while the filled symbols indicate untreated YSZ. Triangles show data from a cell in which PMMA was the pore former.

losses was dramatic. The impedance of the cell made with the PMMA was greater than 2 Ω cm^2, while that of the graphite-prepared cells were approximately 1.2 and 0.5 Ω cm^2, respectively. Clearly, this performance scaled with the surface area of the YSZ scaffold.

As was found in previous studies of LSF-YSZ electrodes following calcination to 1373 K, the impedances are a strong function of current density, especially for the poorer performing cells [25]. This is shown by the data in Figure 3.2c), which provides impedance spectra on the same three cells while applying a current of 400 mA/cm^2. The spectra in Figure 3.2c) are an average of the performance that these electrodes would exhibit under cathodic and anodic polarization, so that the impedances under cathodic polarization at 400 mA/cm^2 cannot be greater than twice the value shown here, even if the electrodes were perfect under anodic polarization. The fact that the impedances decrease with current density shows that the electrodes are better than the high impedances in Figure 3.2b) would indicate. Although all three electrodes look similar in Figure 3.2c), the electrode overpotentials are an impedance integrated over current. That the HF-treated sample is clearly the best of the three is seen from potentials required to achieve 400 mA/cm^2, which were 0.82 V for the cell with the PMMA-formed YSZ, 0.75 V for the cell with the untreated, graphite-formed YSZ, and 0.47 V for the HF-treated YSZ. By subtracting the electrolyte losses, 0.15 V, and dividing by two, the average electrode overpotentials at 400 mA/cm^2 were 0.34 V for the PMMA cell, 0.30 V for the unmodified, graphite cell, and 0.16 V for the HF-treated cell.

In order to demonstrate that HF-treated scaffold can be used to prepare an effective cathode, we prepared a fuel cell with 45-wt% ceria and 1-wt% Pd on anode

side and 35-wt% LSF, calcined to 1123 K, on the cathode side. The performance of this and an otherwise identical but untreated cell on 97% H_2-3% H_2O at 973 K are shown in Figure 3.3. The open-circuit impedance spectrum, Figure 3.3a), indicated a total cell impedance of 0.48 Ω cm^2 for the HF-treated cell and 0.55 Ω cm^2 for the untreated cell, of which 0.38 Ω cm^2 was due to the 75-μm electrolyte. The *V-i* polarization curve in Figure 3.3b) was consistent with the impedance spectra of Figure 3.3a). Since the *V-i* relationships were nearly linear, the impedance of the electrodes must be nearly independent of current density for these preparation conditions.

It is interesting to ask whether the improvement in electrode performance with the different YSZ scaffolds in Figure 3.2 is simply due to an increased surface area for the LSF or whether other factors are also important. As shown in Table 3.1, the surface areas of the LSF-infiltrated composites following calcination at 1123 K in the graphite-formed YSZ, for HF-treated and untreated scaffolds, were similar, 2.0 m^2/g on the untreated and 1.8 m^2/g on the treated samples. It is likely that the high surface areas of these two samples result from the particulate nature of the LSF at this lower calcination temperature. After calcination to 1373 K, the surface areas of LSF-YSZ composites made from these two scaffold materials were 0.30 and 0.48 m^2/g, respectively, for the untreated and treated, graphite-formed YSZ. These areas are much lower than that of the YSZ scaffolds themselves, showing that the LSF must be forming a dense film on the substrates. Since higher scaffold surface area did not translate into a dramatically higher area for the LSF-YSZ composite, we suggest that underlying scaffold must have an effect beyond simply increasing the electrode surface area.

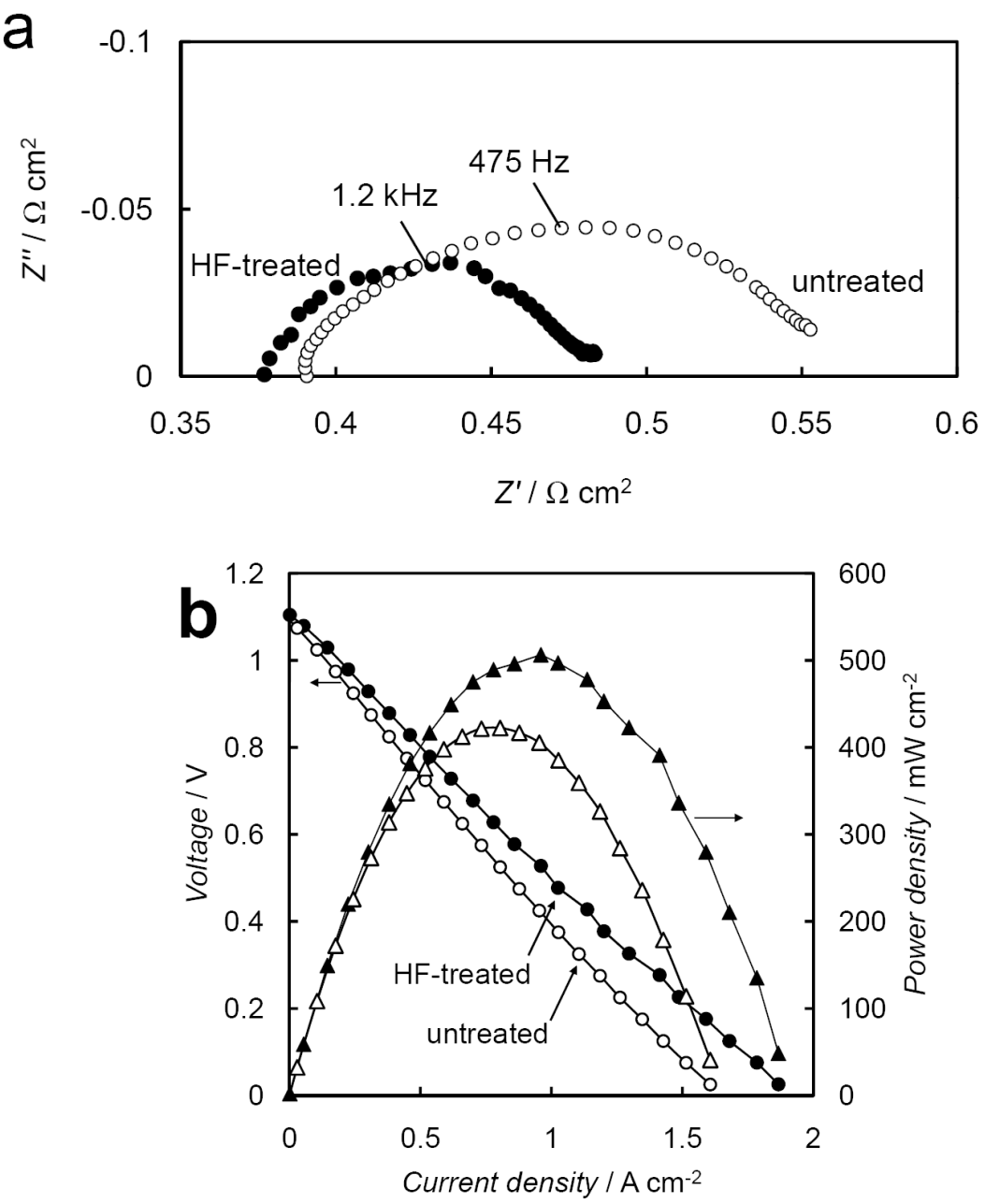

Figure 3.3 Electrochemical testing results of an SOFC single cell with an LSF-YSZ cathode and a 1-wt% Pd – 45-wt% CeO_2 anode at 973 K in humidified (3% H_2O) H_2. Electrochemical impedance spectra at OCV conditions for HF-treated sample (filled symbols) and untreated sample (open symbols) are shown in (a) and corresponding *V-i* and *P-i* curves are shown in (b).

One possibility for understanding the effect of the YSZ scaffold is shown in the schematic in Figure 3.4. Following preparation at 1123 K, both the treated and untreated composites have effective nano-structures associated with the infiltrated LSF. However, after long-time operation or calcination at 1373 K, the LSF coarsens and forms a film over the YSZ structure. Coarsening also occurs in the HF-treated sample, but there is an additional fine structure in the underlying YSZ. Although this fine structure may increase the surface area of the composite slightly, we suggest that a more important effect is to establish underlying, ion-conducting YSZ channels that improve electrode performance.

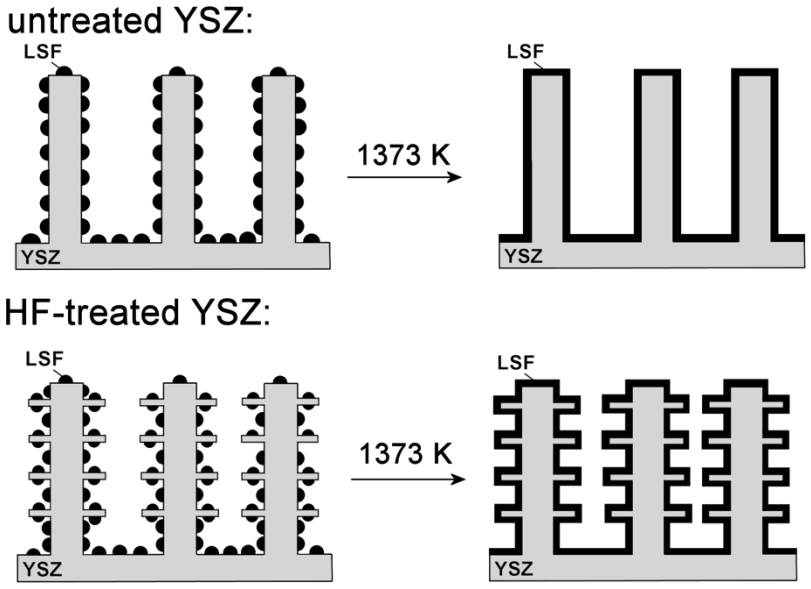

Figure 3.4 A schematic illustrating the changes in microstructure of two different LSF-YSZ composites.

3.5 Conclusion

It has been demonstrated that exposing porous YSZ to a concentrated solution of HF can restructure the pores by dissolution and precipitation processes. Significant increases in the surface areas can be obtained, even after calcination of the treated YSZ to 1373 K. SOFC cathodes formed by infiltration of these treated YSZ scaffolds with LSF showed significantly improved performance.

3.6 References

1. C. W. Tanner, K. Z. Fung, and A. V. Virkar, The effect of porous composite electrode structure on solid oxide fuel cell performance: 1. Theoretical analysis, *J. Electrochem. Soc.,* **144**[1], 21 (1997).
2. S. B. Adler, Factors governing oxygen reduction in solid oxide fuel cell cathodes, *Chem. Rev.,* **104**[10], 4791 (2004).
3. J. Mertens, V. A. C. Haanappel, C. Wedershoven, and H. P. Buchkremer, Sintering behavior of (La, Sr)MnO_3 type cathodes for planar anode-supported SOFCs, *J. Fuel Cell Sci. Technol.,* **3**[4], 415 (2006).
4. M. J. Jørgensen, S. Primdahl, C. Bagger, and M. Mogensen, Effect of sintering temperature on microstructure and performance of LSM–YSZ composite cathodes, *Solid State Ionics,* **139**[1-2], 1 (2001).
5. Y. Huang, J. M. Vohs, and R. J. Gorte, Fabrication of Sr-doped $LaFeO_3$ YSZ composite cathodes, *J. Electrochem. Soc.,* **151**[4], A646 (2004).

6. Y. Huang, J. M. Vohs, and R. J. Gorte, SOFC cathodes prepared by infiltration with various LSM precursors, *Electrochem. Solid-State Lett.,* **9**[5], A237 (2006).
7. Y. Huang, J. M. Vohs, and R. J. Gorte, Characterization of LSM-YSZ Composites Prepared by Impregnation Methods, *J. Electrochem. Soc.,* **152**[7] A1347 (2005).
8. J. M. Vohs and R. J. Gorte, High-performance SOFC cathodes prepared by infiltration, *Adv. Mat.,* **21**[9], 943 (2009).
9. R. Küngas, F. Bidrawn, J. M. Vohs, and R. J. Gorte, Doped-ceria diffusion barriers prepared by infiltration for solid oxide fuel cells, *Electrochem. Solid-State Lett.*, **13**, B87 (2010).
10. M. D. Gross, J. M. Vohs, and R. J. Gorte, Recent progress in SOFC anodes for direct utilization of hydrocarbons, *J. Mater.Chem.,* **17**[30], 3071 (2007).
11. R. Craciun, S. Park, R. J. Gorte, J. M. Vohs, C. Wang, and W. L. Worrell, A novel method for preparing anode cermets for solid oxide fuel cells, *J. Electrochem. Soc.,* **146**[11], 4019 (1999).
12. J. D. Nicholas and S. A. Barnett, Measurements and modeling of $Sm_{0.5}Sr_{0.5}CoO_{3-x}$-$Ce_{0.9}Gd_{0.1}O_{1.95}$ SOFC cathodes produced using infiltrate solution additives, *J. Electrochem. Soc.,* **157**[4], B536 (2010).
13. T. Z. Sholklapper, H. Kurokawa, C. P. Jacobson, S. J. Visco, and L. C. De Jonghe, Nanostructured solid oxide fuel cell electrodes, *Nano Lett.,* **7**[7], 2136 (2007).
14. T. Z. Sholklapper, C. P. Jacobson, S. J. Visco, and L. C. De Jonghe, Synthesis of dispersed and contiguous nanoparticles in solid oxide fuel cell electrodes, *Fuel Cells,* **8**[5], 303 (2008).

15. S. P. Jiang, A review of wet impregnation - an alternative method for the fabrication of high performance and nano-structured electrodes of solid oxide fuel cells, *Mat. Sci. Eng. A,* **418**[1-2], 199 (2006).

16. M. Shah and S. A. Barnett, Solid oxide fuel cell cathodes by infiltration of $La_{0.6}Sr_{0.4}Co_{0.2}Fe_{0.8}O_{3-\delta}$ into Gd-doped ceria, *Solid State Ionics,* **179**[35-36], 2059 (2008).

17. H. P. He, Y. Y. Huang, J. Regal, M. Boaro, J. M. Vohs, and R. J. Gorte, Low-temperature fabrication of oxide composites for solid-oxide fuel cells, *J. Am. Ceram. Soc.,* **87**[3], 331 (2004).

18. A. Mai, V. A. C. Haanappel, S. Uhlenbruck, F. Tietz, and D. Stöver, Ferrite-based perovskites as cathode materials for anode-supported solid oxide fuel cells: Part I. Variation of composition, *Solid State Ionics,* **176**[15-16], 1341 (2005).

19. P. Hjalmarsson, M. Sogaard, and M. Mogensen, Electrochemical performance and degradation of $(La_{0.6}Sr_{0.4})_{0.99}CoO_{3-\delta}$ as porous SOFC-cathode, *Solid State Ionics,* **179**[27-32], 1422 (2008).

20. R. Küngas, I. Kivi, K. Lust, G. Nurk, and E. Lust, Statistical method to optimize the medium temperature solid oxide fuel cell electrode materials, *J. Electroanal. Chem.,* **629**[1-2], 94 (2009).

21. Y. Huang, K. Ahn, J. M. Vohs, and R. J. Gorte, Characterization of Sr-doped $LaCoO_3$-YSZ composites prepared by impregnation methods, *J. Electrochem. Soc.,* **151**[10], A1592 (2004).

22. S. P. Simner, J. P. Shelton, M. D. Anderson, and J. W. Stevenson, Interaction between La(Sr)FeO_3 SOFC cathode and YSZ electrolyte, *Solid State Ionics,* **161**[1-2], 11 (2003).
23. M. Søgaard, P. V. Hendriksen, and M. Mogensen, Oxygen nonstoichiometry and transport properties of strontium substituted lanthanum ferrite, *J. Solid State Chem.,* **180**[4], 1489 (2007).
24. F. Bidrawn, G. Kim, N. Aramrueang, J. M. Vohs, and R. J. Gorte, Dopants to enhance SOFC cathodes based on Sr-doped $LaFeO_3$ and $LaMnO_3$, *J. Power Sources,* **195**[3], 720 (2010).
25. W. S. Wang, M. D. Gross, J. M. Vohs, and R. J. Gorte, The stability of LSF–YSZ electrodes prepared by infiltration, *J. Electrochem. Soc.,* **154**[5], B439 (2007).
26. F. Bidrawn, G. Kim, G. Corre, J. T. S. Irvine, J. M. Vohs, and R. J. Gorte, Efficient reduction of CO_2 in a solid oxide electrolyzer, *Electrochem. Solid State Lett.,* **11**[9], B167 (2008).
27. F. Bidrawn, S. Lee, J. M. Vohs, and R. J. Gorte, The effect of Ca, Sr, and Ba doping on the ionic conductivity and cathode performance of $LaFeO_3$, *J. Electrochem. Soc.,* **155**[7], B660 (2008).
28. M. Boaro, J. M. Vohs, and R. J. Gorte, Synthesis of highly porous yttria-stabilized zirconia by tape-casting methods, *J. Am. Ceram. Soc.,* **86**[3], 395 (2003).
29. S. F. Corbin and P. S. Apté, Engineered porosity via tape casting, lamination and the percolation of pyrolyzable particulates, *J. Am. Ceram. Soc.,* **82**[7], 1693 (1999).

30. R. E. Mistler and E. R. Twiname, *Tape Casting: Theory and Practice*, pp. 298. The American Ceramic Society: Westerville, OH, (2000).

Chapter 4. Evidence of Surface Exchange Limitation in SOFC Cathodes Prepared by Infiltration*

Summary

An analytical model has been developed and experimentally tested to determine the factors that lead to high overpotentials in composite solid oxide fuel cell (SOFC) cathodes. Results suggest that the performance of infiltrated, composite electrodes is limited by O_2 adsorption and incorporation into the perovskite lattice. Model predictions about the effect of the microstructure and ionic conductivity of the porous electrolyte scaffold are verified by experimental results. The impedance of cathodes prepared by infiltration of $La_{0.8}Sr_{0.2}FeO_3$ (LSF) into porous yttria-stabilized zirconia (YSZ) depends strongly on the surface area of the perovskite phase and is independent of LSF film thickness.

4.1 Introduction

It is generally accepted that microstructure plays an important role in determining the impedance of solid oxide fuel cell (SOFC) electrodes [1-5]. A major implication of this is that differences in cell preparation techniques by different groups often makes it difficult to compare results between laboratories. For example, there are many cases where cells with nominally identical electrode compositions show significantly different performance [2]. It is therefore not surprising that the effect of important material

* This paper has been accepted for publication in Solid State Ionics, manuscript number SSI-D-11-00470R1.

properties still remains unclear. For example, the ionic conductivity of the perovskite in a composite cathode is generally considered to be very important in determining cathode impedance [6-8]. However, recent results from our laboratory suggest that performance may be identical for cathodes made of perovskites with ionic conductivities that differ by almost three orders of magnitude [9,10].

In this chapter, the effect of electrode microstructure and composition will be elucidated by combining theoretical and experimental approaches. The theoretical modeling is aimed at predicting key trends between microstructure, chemical composition, and fuel cell cathode performance. The model focuses on SOFC electrodes prepared by infiltration because of the relative simplicity of the composite structure, but the findings are likely to be applicable to more traditional electrode structures [3]. Experimentally, infiltration makes it relatively easy to vary the composition and structure independently, so that predictions from the analytical model can be tested.

To prepare electrodes by infiltration, a porous scaffold of the electrolyte material (e.g. YSZ) is first fabricated by high-temperature calcination. The perovskite conductor is then added in subsequent steps by infiltrating the scaffold with solutions that contain the appropriate cations for synthesizing the perovskites *in situ* [9-23]. The many advantages of this approach (such as improved contact between the electrode and the electrolyte, finer perovskite microstructure, no problems related to dissimilar thermal expansion coefficients, higher conductivity at lower loadings etc.) have been discussed in depth elsewhere [19]. For the purposes of this study, it is important to note that infiltration approach allows one to control the microstructure of the composite to a

degree where one structural parameter can be varied at a time while leaving other properties of the composite unchanged. In other words, electrodes prepared by infiltration are good platforms for carrying out systematic studies on the effect of microstructure and materials properties on electrode performance [20,21].

In this chapter, the main features of a relatively simple analytical model are outlined. Additionally, some experiments that have been conducted to verify the predictions of the model will be described. One noteworthy result is that both the analytical model and the experiments on SOFC cathodes point towards dissociative adsorption of O_2 as the rate-limiting step in SOFC composite cathodes prepared by infiltration.

4.2 Experimental

All electrochemical measurements were carried out on symmetric cells prepared by infiltration of LSF into porous stabilized zirconia scaffolds. The porous scaffolds and the supporting dense electrolyte were prepared by tape casting. A more detailed description of the procedures used has been given elsewhere [11,12,20-23]. The green porous and dense tapes were laminated together in a uniaxial hot press and fired at 1773 K or 1823 K for 4 hours to form a porous-dense-porous electrolyte structure. In some cases, the porous YSZ structure was further modified by a room-temperature hydrofluoric acid (HF) treatment [21], in order to increase surface area.

Infiltration was performed using a ~1 M solution of $La(NO_3)_3 \cdot 6H_2O$, $Sr(NO_3)_2$, $Fe(NO_3)_3 \cdot 9H_2O$ and citric acid at a molar ratio of La : Sr : Fe : citric acid = 0.8:0.2:1:2, until the desired loading of 35-wt% LSF was achieved [13,20,21].

For electrochemical testing, the electrodes were coated with a layer of silver paste (SPI Supplies) and silver contacts were taken from the cell to a Gamry Instruments G750 Potentiostat. All of the measurements were conducted on symmetric cells, and therefore the impedances reported have been divided by two to account for there being two electrodes. Additional physical characterization was performed using an SEM and by BET Kr adsorption measurements at 77 K [14,21]. ImageJ computer software was used for image analysis [24].

4.3. Results and discussion

4.3.1 Model calculations

Our analytical model of the cathode composite is based on a picture developed by Tanner *et al.*, who represented the electrode as an array of electrolyte fins emanating from the dense electrolyte support, covered by perovskite particles [3]. That this is also a reasonable picture of our composite cathodes is shown by the SEM images of $La_{0.8}Sr_{0.2}FeO_3$ (LSF)-YSZ composites formed by infiltration and calcinations to 1373 K, Fig 4.1a,b. At the lower magnification, Fig. 4.1a, the composite appears as a tortuous and interconnected network of YSZ that provides continuous channels for oxygen ions to move from the electrode active sites to the electrolyte bulk. As shown in Fig. 4.1b, the YSZ can be viewed as fins that are about 1 μm in diameter, so that the scaffold is about

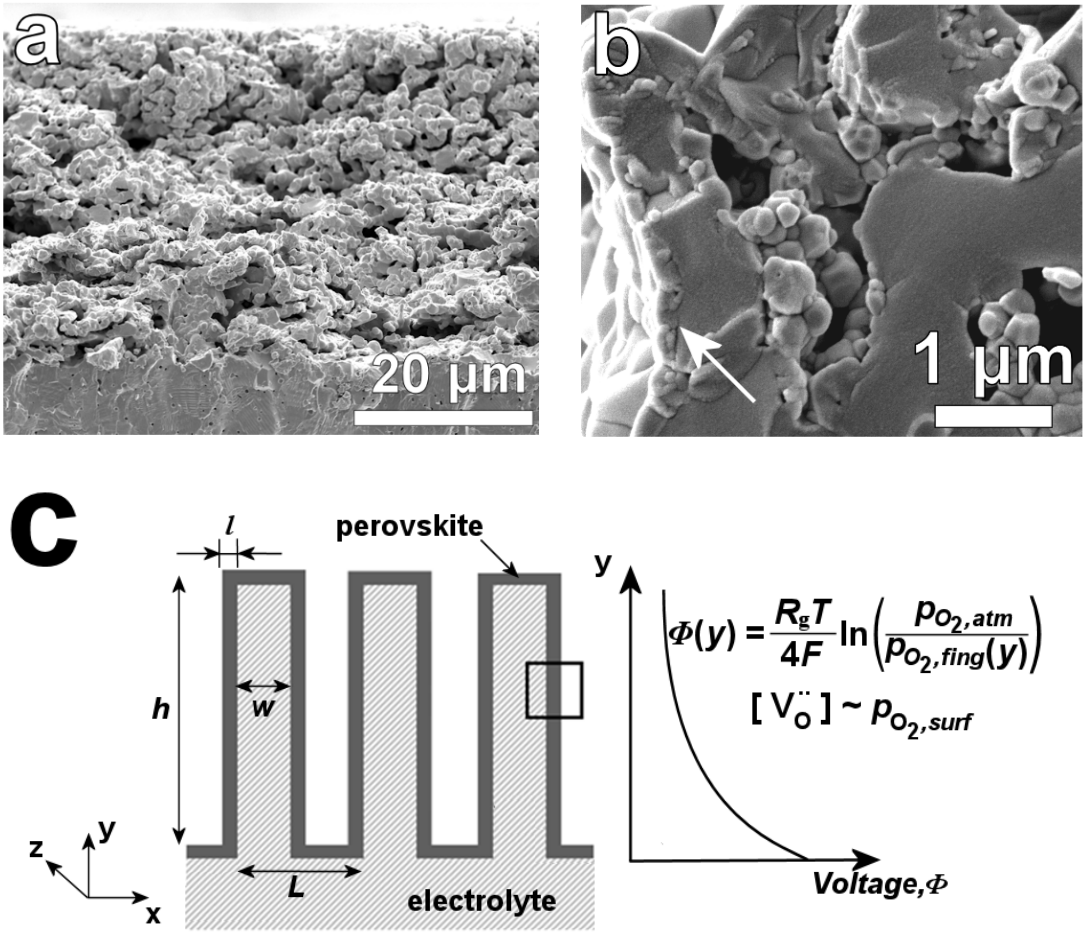

Figure 4.1 SEM images of an LSF-YSZ composite electrode (a,b) and the simplified microstructure considered in the model (c). The arrow in (b) shows the location of LSF film. Inset in (c): potential, Φ, given as a function of distance y, oxygen partial pressure in the gas phase, $p_{O2,atm}$, and effective oxygen partial pressure in the fin, $p_{O2,fin}$. R_g is universal gas constant, T – temperature, F – Faraday constant. The vacancy concentration at the perovskite surface, $[V_O^{\cdot\cdot}]$, is proportional to the oxygen partial pressure at the perovskite surface, $p_{O2,surf}$.

65% porous [25]. The LSF covers the electrolyte fins in the form of either particles or a dense film, depending on the calcination temperature [9,13,19,21]. The simplified structure that we have modeled is then shown in Fig. 4.1c for the case where the perovskite forms a film on the electrolyte fins. We assume that the potential at the base of the fin is equal to the electrode overpotential, Φ_0, and that the potential at other positions in the fin can be related to the p_{O2} at each point on the fin. The electronic conductivity of the perovskite is assumed to be very high and the difference in the potentials of the fin at y=0 and y=h is defined to be the electrode overpotential. While the model starts from a simplified microstructure, it encompasses the main characteristics of real SOFC composite electrodes. Additional details for the model are elsewhere [25].

To determine the potential in the fin as a function of position, it is necessary to obtain an expression for the rate at which O^{2-} ions are inserted into the fin from the perovskite as a function of y. We considered two rate-limiting processes: 1) slow diffusion of oxygen ions through the perovskite film, and 2) slow adsorption of O_2 on a vacancy site on the perovskite surface [25,26]. We assumed that gas phase diffusion is fast so that the p_{O2} outside the film is $p_{O2,atm}$.

In the case of slow diffusion, the logarithm of the effective partial pressure of O_2 decreases linearly with distance x through the film, as shown in Fig. 4.2a. The O_2 flux, J_{O2}, and therefore the current flux, i_S", is then proportional to the ambipolar conductivity of the film, σ_{amb}, the logarithm of the difference in p_{O2}, and inversely proportional to the thickness of the film, l. Furthermore, the electrode impedance can be calculated from the parameters in Fig. 4.2a without additional assumptions.

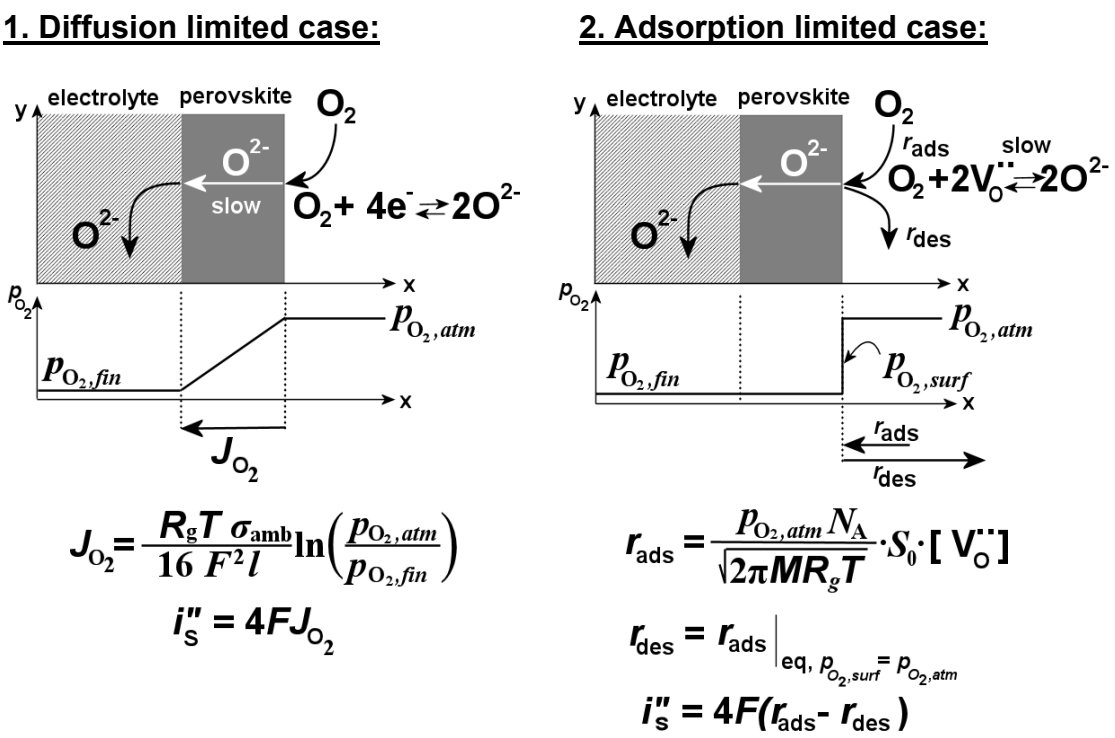

Figure 4.2 Magnified region from Fig. 4.1c: rate-limiting steps considered in the model and corresponding expressions for oxygen flux, J_{O2}, and current flux, i_S". The meaning of symbols used is explained in the text.

When diffusion of O^{2-} is fast compared to the adsorption of O_2, the oxygen activity profile through the perovskite film is essentially flat and exhibits a discontinuity at the perovskite/air interface. We assumed the perovskite surface is then in equilibrium with the oxygen potential that exists at every position *y* in the YSZ fin, as shown in Fig. 4.2b. In order to account for the fact that adsorption of gas-phase O_2 onto the perovskite surface must be a function of the perovskite oxygen potential, we assumed that the rate of adsorption, r_{ads}, calculated from the Kinetic Theory of Gases, is proportional to the flux of O_2 to the surface, and that the concentration of oxygen vacancies on the perovskite surface, $[V_O^{\cdot\cdot}]$ is a function of oxygen potential measured at equilibrium [19,27]. The proportionality constant relating r_{ads} to these values is the reactive sticking coefficient, S_0. S_0 is the probability that an O_2 molecule colliding with a surface vacancy will adsorb and be incorporated into the lattice. The rate of O_2 desorption from the perovskite, r_{des}, is assumed to be equal to r_{ads} in the absence of an overpotential, so that the net adsorption rate under polarization is equal to (r_{ads} - r_{des}). When O_2 adsorption is limiting, electrode impedance is no longer a function of the ionic conductivity or thickness of the perovskite, but depends strongly on O_2 partial pressure of the gas phase and the concentration of oxygen vacancies on the perovskite surface. Although adsorption rates can also be modeled using an oxygen exchange coefficient, k^*, this would require k^* to be determined as a function of the oxygen potential [28,29].

Example calculations for this model have been presented in Ref. 25. Regarding the diffusion-limited case, calculated impedances for LSF-YSZ electrodes were almost 100 times lower than experimentally observed values. Furthermore, modifying the

perovskite so as to change its ionic conductivity had no effect on the experimentally measured impedances [9,10,25]. However, good agreement with experimental data was achieved if adsorption was assumed to be rate-limiting, with $S_0 = \sim 10^{-3}$. Therefore, our calculations suggest that surface adsorption, and not diffusion, is rate-limiting in LSF-YSZ electrodes.

4.3.2 Effect of perovskite microstructure

One implication of adsorption limitation is that electrode performance should be a strong function of the surface area of the perovskite phase. With infiltrated electrodes, this surface area can be modified by increasing the calcination temperature, without affecting the scaffold phase. To study this effect, we examined symmetric cells with 35-wt% LSF in YSZ, heated to various temperatures in order to change the LSF microstructure, as shown in Fig. 4.3a. Because there is no interfacial reaction between LSF and YSZ below 1573 K [13], only the perovskite microstructure and not the chemical composition of the cathode was affected by heating.

Fig. 4.3a shows the LSF is present as discrete particles following calcination at 1123 K. The particle size distribution, obtained by analysis of approximately 2000 particles, follows a log-normal distribution with a maximum at 50 nm (Fig. 4.3b). Upon heating to higher temperatures, the particles agglomerate and the particle-size distribution shifts toward larger particle sizes. By 1373 K, the perovskite covers the underlying YSZ completely in the form of a dense film. Particles larger than 500 nm are present, although the mean particle size is still about 125 nm (Fig. 4.3b).

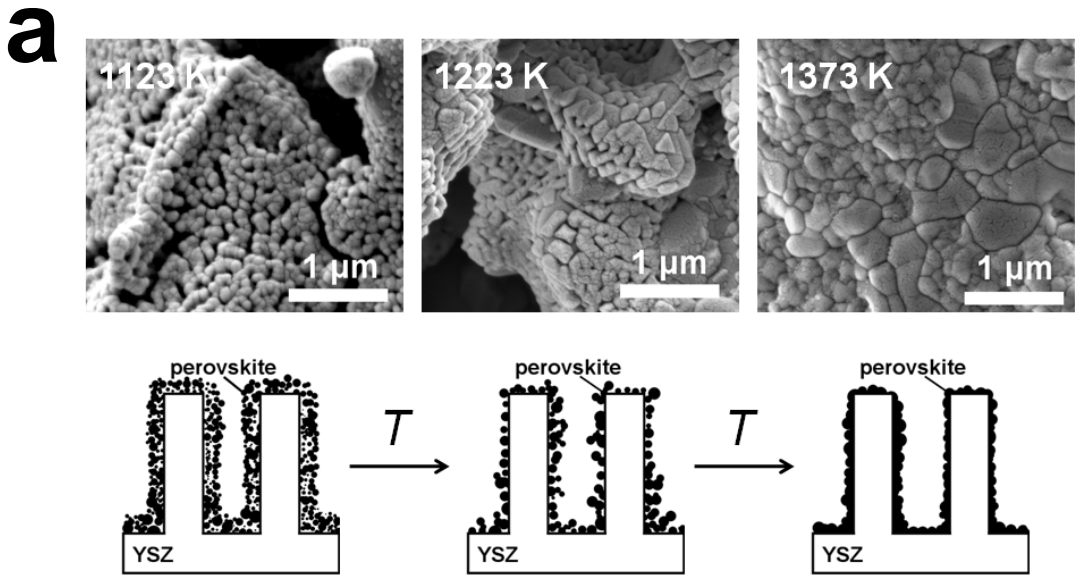

Figure 4.3a The microstructure of $La_{0.8}Sr_{0.2}CoO_3$-YSZ composites as a function of calcination temperature: SEM images and illustrating schematic drawings of the perovskite structure.

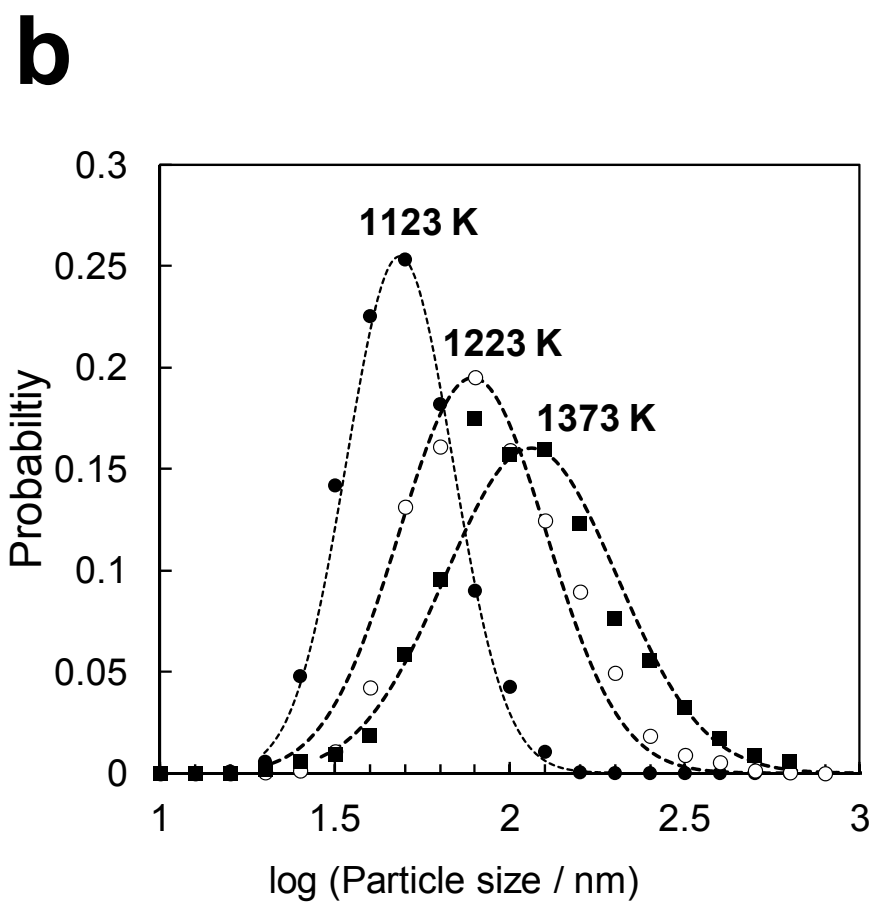

Figure 4.3b The microstructure of $La_{0.8}Sr_{0.2}CoO_3$-YSZ composites as a function of calcination temperature: the corresponding particle size distributions as determined by image analysis.

Although SEM images provide a visual picture of the changes that occur in the perovskite, BET adsorption measurements are able to provide more quantitative information in the form of catalyst specific surface areas, as shown in Table 4.1. The LSF-YSZ composite calcined to 1123 K had a surface area of 1.31 m^2/g. This decreased with temperature until it reached 0.5 m^2/g above 1323 K. Because this area is close to that of the YSZ scaffold, the LSF in this case must be forming a film.

In good agreement with the hypothesis of slow O_2 adsorption, we found that for the electrode polarization resistance, R_p, increased with decreasing perovskite surface area, as shown by the values in Table 4.1. The LSF-YSZ electrode heated to 1123 K exhibited a resistance of 0.12 Ω cm^2 at 973 K, whereas an electrode heated to 1373 K had a resistance of 1.08 Ω cm^2. It is interesting that the relationship between polarization resistance and surface area was not linear. Initially, large decreases in surface area resulted in relatively small changes in performance, whereas even small changes in surface area affected the performance dramatically at the higher calcination temperatures.

In order to demonstrate that solid-state reactions were not responsible for electrode deactivation at 1373 K, we infiltrated an additional 15-wt% LSF onto the deactivated electrode, followed by calcination at 1123 K, in order to restore the surface area of the composite back to 0.75 m^2/g. As shown in Fig. 4.4 and Table 4.1, this procedure restored by electrode polarization resistance to 0.22 Ω cm^2. Recalcination to 1373 K again increased the resistance to ~ 1 Ω cm^2. This result supports the conclusion that oxygen reduction kinetics in composite SOFC cathodes are limited by a slow surface process. If diffusion were rate-limiting, the impedance should have increased after

Table 4.1 Summary of the effect of calcination temperature on the BET surface area and electrochemical properties of LSF-YSZ symmetric cells.

Calcination temperature	BET surface area (m^2/g)	R_{ohm} at 973 K / $\Omega\ cm^2$	R_p at 973 K / $\Omega\ cm^2$
1123 K	1.31	0.19	0.12
1173 K	0.86	0.15	0.22
1223 K	0.83	0.19	0.19
1273 K	0.56	0.18	0.28
1323 K	0.47	0.20	0.85
1373 K	0.46	0.27	1.08
1373 K + 1123 K*	0.75	0.20	0.22

* With 15 wt% additional LSF added after 1373 K.

addition of more LSF due to increased film thickness. Similar enhancement upon addition of oxides into composite cathodes have been reported in the literature for various perovskite cathodes [30-32], suggesting that adsorption rates likely limit performance with other perovskites as well. Several oxygen permeation and isotope exchange measurements (such as studies by Gurauskis *et al*. on $La_{0.2}Sr_{0.8}Fe_{0.8}Ta_{0.2}O_{3-\delta}$ and Bouwmeester *et al*. on $Ba_{0.5}Sr_{0.5}Co_{0.8}Fe_{0.2}O_{3-\delta}$ and $La_2NiO_{4+\delta}$) also show that adsorption is rate-limiting in these systems [33,34].

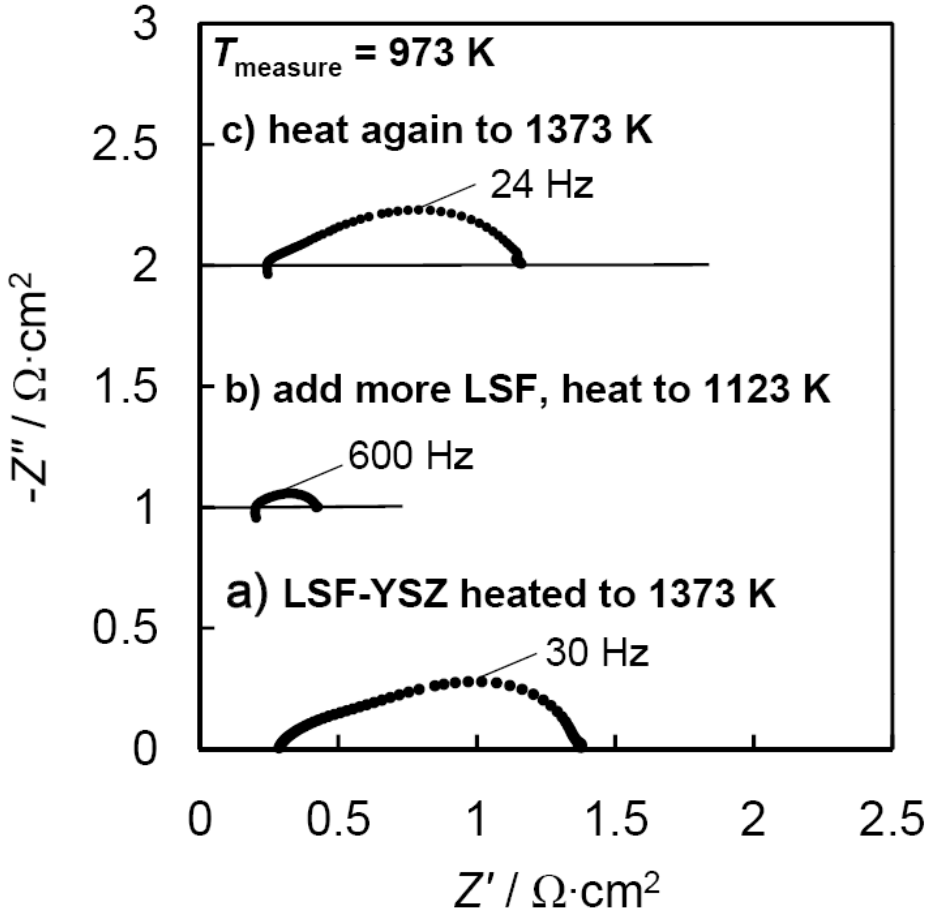

Figure 4.4 Electrochemical performance of LSF-YSZ symmetric cells at 973 K in air: a) initial impedance after deactivation at 1373 K, b) impedance after infiltration of additional 15 wt% of LSF into the deactivated structure and calcination to 1123 K, c) impedance after the composite was re-heated to 1373 K.

4.3.3 Effect of electrolyte microstructure

The model in Fig. 4.1c implies that the resistance of a composite cathode should also depend on the microstructure and ionic conductivity of the porous electrolyte scaffold. Impedance should decrease as the fins become smaller in width, *w*, due to increase in electrode surface area. To determine the effect of structure, we prepared symmetric cells with various YSZ scaffolds [20]. The structure of the empty scaffolds is shown in the SEM images in Fig. 4.5, while the properties of the composite electrodes are summarized Table 4.2. The use of different pore formers allowed the scaffold surface area to change from 0.04 m^2/g (Fig. 4.5a) to 0.48 m^2/g (Fig. 4.5b). This surface area could be further increased by treatment with HF (Fig. 4.5c) [20]. All these scaffolds were infiltrated with 35-wt% LSF, calcined to either 1123 K or 1373 K, and tested at 973 K in air. The polarization resistances were strongly affected by the microstructure of the porous scaffold, especially after a heat treatment to 1373 K. The polarization resistance of the low surface area electrode was 2.12 $\Omega\ cm^2$, whereas that of the high surface area, HF-treated cell was almost 5 times lower under the same experimental conditions [20]. Therefore, SOFC cathode performance can be greatly enhanced by increasing the surface area of the porous electrolyte scaffold.

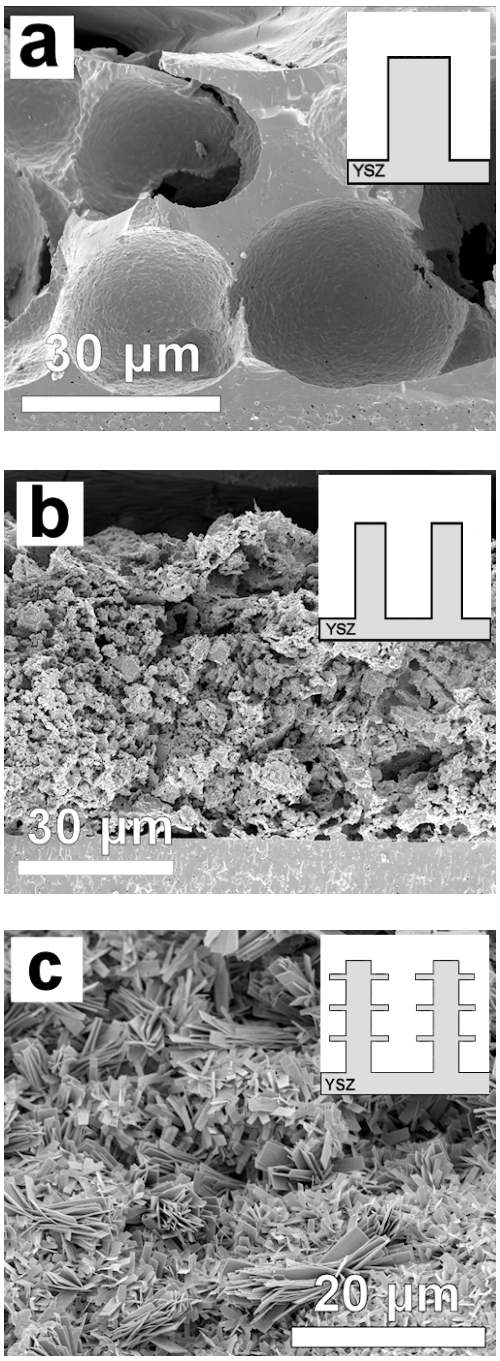

Figure 4.5 SEM micrographs of YSZ scaffolds prior to infiltration with LSF: (a) PMMA-YSZ, (b) graphite-YSZ, and (c) HF-treated graphite-YSZ.

Table 4.2 Summary of the BET surface areas of porous electrolyte scaffolds, and ohmic and polarization resistances of corresponding LSF-YSZ symmetric cells tested in air at 973 K and treated at 1123 K or 1373 K.

Electrode	BET surface area of YSZ scaffold (m^2/g)	R_{ohmic} at 973 K (Ω cm^2)		$R_{polarization}$ at 973 K (Ω cm^2)	
		After 1123 K	After 1373 K	After 1123 K	After 1373 K
LSF-(PMMA)YSZ	0.04	-	0.20	-	2.12
LSF-(graphite)YSZ	0.48	0.18	0.19	0.13	1.09
LSF-(HF)YSZ	3.00	0.19	0.18	0.18	0.44

4.3.4 Effect of the ionic conductivity of the porous electrolyte

For both rate-limiting steps, the model described in Section 4.3.1 predicts that the electrode impedance will depend on the ionic conductivity of the scaffold. To verify this effect experimentally, electrodes were prepared using scaffolds made from electrolyte materials having very different ionic conductivies: 8 mol% YSZ, 10 mol% Sc_2O_3-stabilized zirconia (ScSZ), and 10 mol% Al_2O_3, 3 mol% Y_2O_3 co-stabilized zirconia (YAZ). The microstructure of the zirconia scaffolds was identical in each case. After infiltration with 35-wt% LSF, the cells were heated to either 1123 K or 1373 K for 4 hours and then tested at 973 K.

As shown by the data in Table 4.3, the ohmic resistances, R_{ohm}, were in good agreement with the literature ionic conductivity values for these electrolytes [21,35,36]. However, the values for the polarization resistance increase in the order ScSZ < YSZ < YAZ for both 1123 K and 1373 K samples. Based on the data in Table 4.3, the value of the exponent x in $R_p \sim \sigma_{i,electrolyte}^{x}$ is equal to -0.73 for samples treated at 1373 K. This value agrees reasonably well with the -0.5 dependence predicted by the models [3,25]. For lower temperature samples, the dependence on ionic conductivity is stronger (x = -1.16), which likely arises because of the nanoscale microstructure of the perovskite [21]. Based on these results, it is clear that the ionic conductivity of the porous electrolyte scaffold also plays an important role in determining the cathode performance.

Table 4.3 Summary of ionic conductivity of the electrolyte, ohmic and polarization resistance of LSF-stabilized zirconia symmetric cells tested in air at 973 K.

Electrode	$\sigma_{i,electrolyte}$ at 973 K (S/cm)	R_{ohm} at 973 K (Ω cm^2)		R_p at 973 K (Ω cm^2)	
		After 1123 K	After 1373 K	After 1123 K	After 1373 K
LSF-YAZ	0.0048 [35]	1.27	1.30	0.72	2.67
LSF-YSZ	0.018 [36]	0.32	0.26	0.14	0.91
LSF-ScSZ	0.048 [21]	0.10	0.13	0.06	0.54

4.4 Conclusion

In this chapter, we presented a model as well as a set of supporting experimental data suggesting that the performance of typical SOFC composite electrodes, such as LSF-YSZ, is limited by slow surface process, i.e. O_2 adsorption and incorporation into the perovskite lattice.

The model implies that electrode impedances depend strongly on the perovskite surface area available for reaction and on the structure and ionic conductivity of the porous electrolyte scaffold. These predictions were experimentally verified on LSF-YSZ symmetric cells prepared by infiltration.

Experimental evidence shows that electrode performance is enhanced when the surface area of the perovskite phase is increased. However, no increase in impedance was observed when the thickness of the perovskite film was increased. Significant improvement is also observed when the surface area of the porous YSZ scaffold is

increased. Finally, the ionic conductivity of the scaffold was also found to affect performance, in good quantitative agreement with model predictions.

4.5 References

1. M. J. L. Østergård, C. Clausen, C. Bagger and M. Mogensen, Manganite-zirconia composite cathode for SOFC: influence of structure and composition, *Electrochim. Acta*, **40**[12], 1971 (1995).
2. M. J. Jørgensen and M. Mogensen, Impedance of solid oxide fuel cell LSM/YSZ composite cathodes, *J. Electrochem. Soc.,* **148**, A433 (2001).
3. C. W. Tanner, K.-Z. Fung, and A. V. Virkar, The effect of porous composite electrode structure on solid oxide fuel cell performance: Part I - theoretical analysis, *J. Electrochem. Soc.*, **144**, 21 (1997).
4. J. R. Smith, A. Chen, D. Gostovic, D. Hickey, D. Kundinger, K. L. Duncan, R. T. DeHoff, K. S. Jones, and E. D. Wachsman, Evaluation of the relationship between cathode microstructure and electrochemical behavior for SOFCs, *Solid State Ionics*, **180**, 90 (2009).
5. J. R. Wilson, W. Kobsiriphat, R. Mendoza, H.-Y. Chen, T. Hines, J. M. Hiller, D. J. Miller, K. Thornton, P. W. Voorhees, S. B. Adler, D. Mumm, and S. A. Barnett, Three dimensional reconstruction of solid oxide fuel cell electrodes using focused ion beam - scanning electron microscopy, *ECS Trans.* **7**[1], 1879 (2007).
6. S. B. Adler, J. A. Lane, and B. C. H. Steele, Electrode kinetics of porous mixed-conducting oxygen electrodes, *J. Electrochem. Soc*., **143**, 3554 (1996).

7. S. B. Adler, Factors governing oxygen reduction in solid oxide fuel cell cathodes, *Chem. Rev.,* **104**[10], 4791 (2004).
8. J. Fleig and J. Maier, The polarization of mixed conducting SOFC cathodes: Effects of surface reaction coefficient, ionic conductivity and geometry, *J. Eur. Ceram. Soc.*, **24**, 1343. (2004).
9. F. Bidrawn, S. Lee, J. M. Vohs, and R. J. Gorte, The effect of Ca, Sr, and Ba doping on the ionic conductivity and cathode performance of $LaFeO_3$, *J. Electrochem. Soc.,* **155**[7], B660 (2008).
10. S. Lee, M. Bevilacqua, P. Fornasiero, J. M. Vohs, and R. J. Gorte, Solid oxide fuel cell cathodes prepared by infiltration of $LaNi_{0.6}Fe_{0.4}O_3$ and $La_{0.91}Sr_{0.09}Ni_{0.6}Fe_{0.4}O_3$ in porous yttria-stabilized zirconia, *J. Power Sources*, **193**, 747 (2009).
11. Y. Huang, J. M. Vohs, and R. J. Gorte Fabrication of Sr-doped $LaFeO_3$ YSZ composite cathodes, *J. Electrochem. Soc.,* **151**[4], A646 (2004).
12. Y. Huang, J. M. Vohs, and R. J. Gorte, Characterization of LSM-YSZ Composites Prepared by Impregnation Methods, *J. Electrochem. Soc.,* **152**[7] A1347 (2005).
13. W. Wang, M. D. Gross, J. M. Vohs, and R. J. Gorte, The stability of LSF–YSZ electrodes prepared by infiltration, *J. Electrochem. Soc.,* **154**[5], B439 (2007).
14. R. Küngas, F. Bidrawn, J. M. Vohs, and R. J. Gorte, Doped-ceria diffusion barriers prepared by infiltration for solid oxide fuel cells, *Electrochem. Solid-State Lett.*, **13**, B87 (2010).

15. M. Shah and S. A. Barnett, Solid oxide fuel cell cathodes by infiltration of $La_{0.6}Sr_{0.4}Co_{0.2}Fe_{0.8}O_{3-\delta}$ into Gd-doped ceria, *Solid State Ionics,* **179**[35-36], 2059 (2008).
16. A. Samson, M. Søgaard, R. Knibbe and N. Bonanos, High Performance Cathodes for Solid Oxide Fuel Cells Prepared by Infiltration of $La_{0.6}Sr_{0.4}CoO_{3-\delta}$ into Gd-Doped Ceria, *J. Electrochem. Soc.*, **158**[6], B650 (2011).
17. T. Z. Sholklapper, H. Kurokawa, C. P. Jacobson, S. J. Visco, and L. C. De Jonghe, Nanostructured solid oxide fuel cell electrodes, *Nano Lett.,* **7**[7], 2136 (2007).
18. S. P. Jiang, A review of wet impregnation - an alternative method for the fabrication of high performance and nano-structured electrodes of solid oxide fuel cells, *Mat. Sci. Eng. A,* **418**[1-2], 199 (2006).
19. J. M. Vohs and R. J. Gorte, High-performance SOFC cathodes prepared by infiltration, *Adv. Mat.,* **21**[9], 943 (2009).
20. R. Küngas, J.-S. Kim, J. M. Vohs, and R. J. Gorte, Restructuring porous YSZ by treatment in hydrofluoric acid for use in SOFC cathodes, *J. Am. Ceram. Soc*, **94**[7], 2220 (2011).
21. R. Küngas, J. M. Vohs, and R. J. Gorte, Effect of ionic conductivity of the electrolyte in composite SOFC cathodes, *J. Electrochem. Soc*, **158**[6], B743 (2011).
22. H. P. He, Y. Huang, J. Regal, M. Boaro, J. M. Vohs, and R. J. Gorte, Low-temperature fabrication of oxide composites for solid-oxide fuel cells, *J. Am. Ceram. Soc.,* **87**[3], 331 (2004).

23. M. Boaro, J. M. Vohs, and R. J. Gorte, Synthesis of highly porous yttria-stabilized zirconia by tape-casting methods, *J. Am. Ceram. Soc.,* **86**[3], 395 (2003).

24. W.S. Rasband, *ImageJ*, U.S. National Institutes of Health, Bethesda, Maryland, USA, http://imagej.nih.gov/ij/, 1997-2012.

25. F. Bidrawn, R. Küngas, J. M. Vohs, and R. J. Gorte, Modeling impedance response of SOFC cathodes prepared by infiltration, *J. Electrochem. Soc.*, **158**[5], B514 (2011).

26. R. J. Gorte and J. M. Vohs, Catalysis in solid oxide fuel cells, *Annu. Rev. Chem. Biomol. Eng.* **2**, 9 (2011).

27. M. Søgaard, P. V. Hendriksen, and M. Mogensen, Oxygen nonstoichiometry and transport properties of strontium substituted lanthanum ferrite*, J. Solid State Chem.,* **180**[4], 1489 (2007).

28. T. Kawada, J. Suzuki, M. Sase, A. Kaimai, K. Yashiro, Y. Nigara, J. Mizusaki, K. Kawamura, and H. Yugami, Determination of oxygen vacancy concentration in a thin film of $La_{0.6}Sr_{0.4}CoO_{3-\delta}$ by an electrochemical method, *J. Electrochem. Soc.* **149**, E252 (2002).

29. Ø. F. Lohne, T. N. Phung, H. L. Lein, H. J. M. Bouwmeester, and K. Wiik, Effect of B-site doping on oxygen transport properties and stability of $La_{0.2}Sr_{0.8}Fe_{1-x}M_xO_{3-\delta}$, M=Al, Zr, Ta, *Proceedings of the 18th International Conference on Solid State Ionics*, Warsaw, Poland, p. 70 (2011).

30. F. Bidrawn, G. Kim, N. Aramrueang, J. M. Vohs, and R. J. Gorte, Dopants to enhance SOFC cathodes based on Sr-doped $LaFeO_3$ and $LaMnO_3$, *J. Power Sources,* **195**[3], 720 (2010).

31. Na Ai, S. P. Jiang, Z. Lü, K. Chen, and W. Su, Nanostructured $(Ba,Sr)(Co,Fe)O_{3-\delta}$ impregnated $(La,Sr)MnO_3$ cathode for intermediate-temperature solid oxide fuel cells, *J. Electrochem. Soc.* **157**[7], B1033 (2010).

32. M. Mogensen, M. Søgaard, P. Blennow, and K. Kammer Hansen, The action of SOFC nano-particles, *Proceedings of the 8th European SOFC Forum*, Lucerne, Switzerland, 6 p. (2008).

33. J. Gurauskis, E. Wefring, Ø. F. Lohne, H. L. Lein, and K. Wiik, LSFTa perovskite based membranes for oxygen separation, *Proceedings of the 18th International Conference on Solid State Ionics*, Warsaw, Poland, p. 310 (2011).

34. H. J. M. Bouwmeester, C. Song, J. Zhu, J. Yi, M. van Sint Annaland, and B. A. Boukamp, A novel pulse isotopic exchange technique for rapid determination of the oxygen surface exchange rate of oxide ion conductors, *Phys. Chem. Chem. Phys.*, **11**, 9640 (2009).

35. O. Yamamoto, T. Kawahara, K. Kohno, Y. Takeda, and N. Imanshi, in *Solid State Materials*, S. Radhakrishna and A. Daud, (Eds,), p. 372, Narosa Publishing House, New Delhi (1991).

36. V. V. Kharton, F. M. B. Marques, and A. Atkinson, Transport properties of solid oxide electrolyte ceramics: a brief review, *Solid State Ionics*, **174**, 135 (2004).

Chapter 5. Doped-Ceria Diffusion Barriers Prepared by Infiltration for Solid Oxide Fuel Cells*

Summary

To stabilize solid oxide fuel cell cathodes prepared by infiltration of $La_{0.8}Sr_{0.2}CoO_3$ (LSCo) into porous yttria-stabilized zirconia (YSZ), a coating of Sm-doped ceria (SDC) was first deposited onto the YSZ scaffold. The dense SDC coating was prepared by infiltration with aqueous solutions of $Sm(NO_3)_3$ and $Ce(NO_3)_3$, followed by calcination to 1473 K. The SDC coating was shown to prevent solid-state reactions between LSCo and YSZ at 1373 K. LSCo-SDC/YSZ electrodes exhibited low cathode impedances, ~20 mΩ cm^2, at 973 K, with acceptable degradation after heating to 1373 K.

5.1 Introduction

The most commonly used material for cathodes in solid oxide fuel cells (SOFC) is a composite of Sr-doped $LaMnO_3$ (LSM) and yttria-stabilized zirconia (YSZ), with the LSM in the composite providing electronic conductivity and catalytic activity for oxygen reduction. The addition of YSZ to the electrode provides ionic conductivity to increase the length of the three-phase boundary (TPB) by providing ion-conducting channels from the electrolyte into the electrode [1]. In most cases, LSM-YSZ composites are prepared by sintering a mixture of LSM and YSZ powders onto the YSZ electrolyte.

* This chapter was published as a research paper in Electrochemical and Solid-State Letters, 13(8) (2010) B87.

Relatively high temperatures (>~1300 K [2]) are required in order to sinter the YSZ particles in the electrode to the electrolyte. Significantly improved performance can be achieved by replacing LSM with mixed conducting perovskites, such as Sr-doped $LaCoO_3$ (LSCo) [3-7], $LaFeO_3$ (LSF) [8-12], or $LaCo_xFe_{1-x}O_3$ (LSCF) [13,14]; however, it is not possible to co-fire these perovskites with YSZ at the temperatures required for sintering the YSZ phase because this leads to either reaction with the YSZ or other effects that lower the electrode performance [15,16].

Recently, composite electrodes have been prepared without high-temperature sintering of the perovskite phase using infiltration [16-18]. In this case, a porous YSZ scaffold is first sintered together with the electrolyte and the perovskite is then added in subsequent steps by infiltrating the porous YSZ with solutions that contain either the nano-particles of the perovskites or the appropriate cations for synthesizing the perovskites *in situ* [19,20]. Composites prepared by infiltration have two main advantages over composites prepared by traditional approaches. First, the sintering temperature for the YSZ component of the composite can be much higher than the sintering temperature used for the perovskite. Because the YSZ scaffold can be sintered to the electrolyte at very high temperatures, the ion-conducting channels from the electrolyte into the electrode are well established and de-lamination of electrodes is typically not a problem. Second, because the conducting phase is added to an existing YSZ scaffold, the composites formed by infiltration are not random. One implication of the non-random structure is that sufficient conductivity can be achieved using perovskite loadings below the normal percolation threshold of 30-vol% [16,21]. Another

consequence is that the coefficients of thermal expansion (CTE) of the composite are closer to that of YSZ scaffold than to the weighted average of the components [6].

Composites of Sr-doped $LaCoO_3$ (LSCo) and YSZ have been shown to provide very low cathode impedances when prepared by infiltration [6,22]; however, the impedance has been observed to increase dramatically with time or increased calcination temperature. Degradation with LSCo is likely due to solid-state reactions, which have been observed to occur between YSZ and $LaCoO_3$ at temperatures as low as 973 K [23]. The usual approach to preventing solid-state reactions between perovskites and YSZ involves incorporating a thin layer of doped ceria (e.g. $Ce_{0.8}Sm_{0.2}O_{1.9}$, SDC) between the electrolyte and the electrode, in a manner similar to what is shown in Figure 5.1a) [24,25]. This approach is being successfully applied with cathodes based on Sr-doped $LaCo_{0.2}Fe_{0.8}O_3$ (LSCF) [26]. However, the incorporation of barrier layers does not prevent problems of CTE mismatch or mechanical instability. Furthermore, a recent comparison of LSM cathodes with and without doped-ceria layers indicated that doped ceria layer may alter performance in a more complicated manner [27].

In the present study, we set out to test an alternative method for incorporating a barrier layer, shown schematically in Figure 5.1b). The concept was to coat the porous YSZ scaffold with SDC prior to infiltration with the conducting perovskite. Electrodes prepared in this manner exhibit the advantages associated with infiltrated electrodes (e.g. less LSCo required for conductivity, better CTE match, better stability towards de-lamination), while minimizing problems associated with solid-state reactions at the LSCo-YSZ interface.

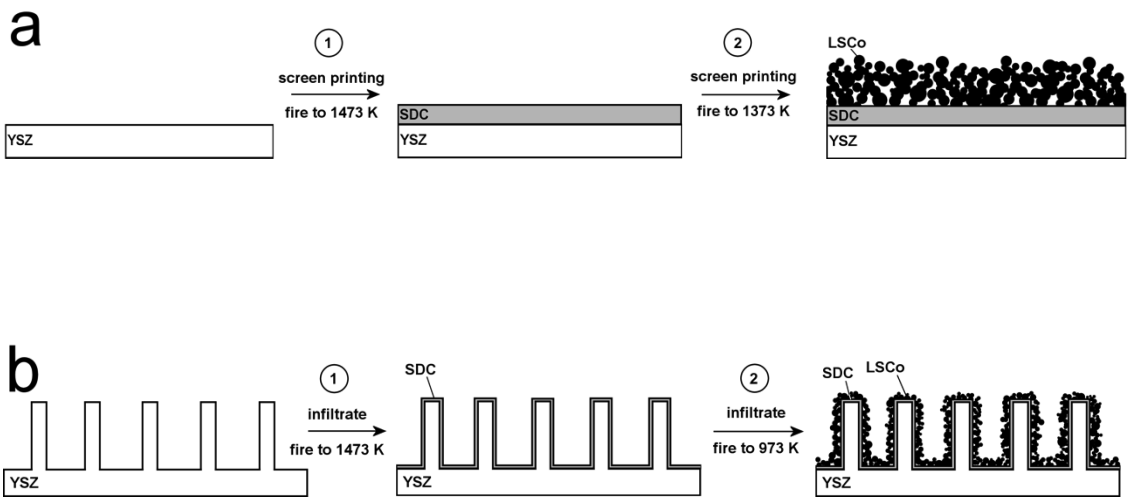

Figure 5.1 Schematic comparison of traditional (a) and proposed (b) approach to preparing SDC diffusion barrier layers.

5.2 Experimental

The electrode performances in this study were measured using symmetric cells. The first step in cell fabrication involved making a porous-dense-porous YSZ wafer using tape-casting methods, as described in detail elsewhere [28]. After sintering the tapes at 1773 K for 4 hours, the dense electrolyte layers were 88±5 μm thick and 1 cm in diameter, while the two porous layers were each 55±2 μm in thickness and 0.67 cm in diameter. Based on earlier work, the porous layers were known to be between 60 to 65% porous [28]. To prepare an SDC barrier coating, an aqueous mixture of $Ce(NO_3)_3 \cdot 6H_2O$ (Alfa Aesar, 99.5%) and $Sm(NO_3)_3 \cdot 6H_2O$ (Alfa Aesar, 99.9%) was infiltrated into the porous YSZ layers, followed by heating in air to 723 K. Infiltration steps were repeated until desired loading had been achieved. The cells were then fired to temperatures up to 1473 K for 4 hours.

The LSCo-YSZ and LSCo-SDC-YSZ electrodes were prepared by infiltration of the porous YSZ or the SDC-YSZ scaffolds with an aqueous solution consisting of $La(NO_3)_3 \cdot 6H_2O$ (Alfa Aesar, 99.9%), $Sr(NO_3)_2$ (Alfa Aesar, 99%), and $Co(NO_3) \cdot 6H_2O$ (Aldrich, 99%) at a molar ratio of La:Sr:Co = 0.8:0.2:1. Citric acid, in a 1:1 ratio with the metal cations, was used as a complexing agent in order to form the perovskite at lower temperatures. The use of a complexing agent is critical, since new phases, indicative of solid-state reaction with the YSZ, were formed at much lower temperatures when citric acid was not included. Furthermore, we found the reproducibility of the electrochemical test results to improve significantly when complexing agent was used. Infiltration was followed by heat treatment in air at 723 K. Multiple infiltration steps

were needed to reach the final loading of 35 wt% (~20 vol%). In order to form the desired perovskite structure, the cells were heated in air to 973 K for 4 hours prior to applying Ag paste for current collection. The cells were then attached to an alumina rod using a ceramic adhesive (Aremco, Ceramabond 552). Electrochemical impedance spectra were recorded using a Gamry Instruments potentiostat in the frequency range of 0.1 Hz to 100 kHz and with an AC perturbation of 5 mA, with the samples held in ambient air. All of the impedances in this paper have been divided by two to account for there being two electrodes.

BET and XRD characterizations were carried out on 3 × 3 × 10 mm slabs, prepared from the same slurries that were used in the tape-casting process for the porous YSZ. X-ray diffraction patterns were measured using Cu K_α radiation. BET isotherms were measured using Kr adsorption at 78 K and were used to determine surface areas. Scanning electron microscopy (SEM) coupled with energy-dispersive x-ray analysis (FEI Quanta 600 FE-SEM) was used to determine the microstructure and elemental distribution of prepared cells.

5.3 Results and discussion

In earlier studies of ceria incorporation into YSZ scaffolds, ceria was found to form a porous coating of nanoparticles over the porous YSZ following calcination at temperatures below 1123 K, with then increasingly dense films being formed at calcination temperatures above 1473 K [29]. Since the doped-ceria interlayers must be dense in order to effectively prevent interfacial reactions [26], we first investigated the

effect of sintering temperature on the morphology of SDC in YSZ using SEM and BET isotherms.

The SEM results for the SDC coatings are shown in Figure 5.2. Figure 5.2a) is a micrograph of the empty YSZ scaffold. The pore structure has an appearance similar to that of a sponge, with pores ranging between 0.5 and 3 μm. After adding 20-wt% (~10-vol%) SDC with calcination to 1373 K, the YSZ scaffold is covered by well-defined particles that are much less than 0.1 μm in diameter. There appear to be gaps between the particles that would allow fluid-phase species to interact with the underlying YSZ. The SDC particles grow dramatically after heating to 1473 K, Figure 5.2c), forming crystallites that are 0.2 to 0.3 μm in size and that completely cover the YSZ scaffold. An EDX scan along the line A-B in Figure 5.2c), Figure 5.2d), demonstrated that Ce was evenly distributed on the surface of the underlying YSZ. The peaks in Ce concentration in this line scan correspond to the edges of the original YSZ features, where the SDC film appears thicker to the electron beam used in the EDX measurement. There were no signs of phase segregation or of large blocks of SDC anywhere in the sample.

Data from the BET isotherms, shown in Table 5.1, confirm the above picture. In the absence of added SDC, the YSZ scaffold had a surface area 0.27 m^2/g. For a material with uniform cylindrical pores, a porosity of 65%, and walls having the bulk density of YSZ, the average pore diameter is calculated to be ~3 μm [30], a value that is in reasonable agreement with the SEM measurements. Following the addition of 20-wt% SDC and calcination to 1123 K, the surface area increased to 1.2 m^2/g due to the

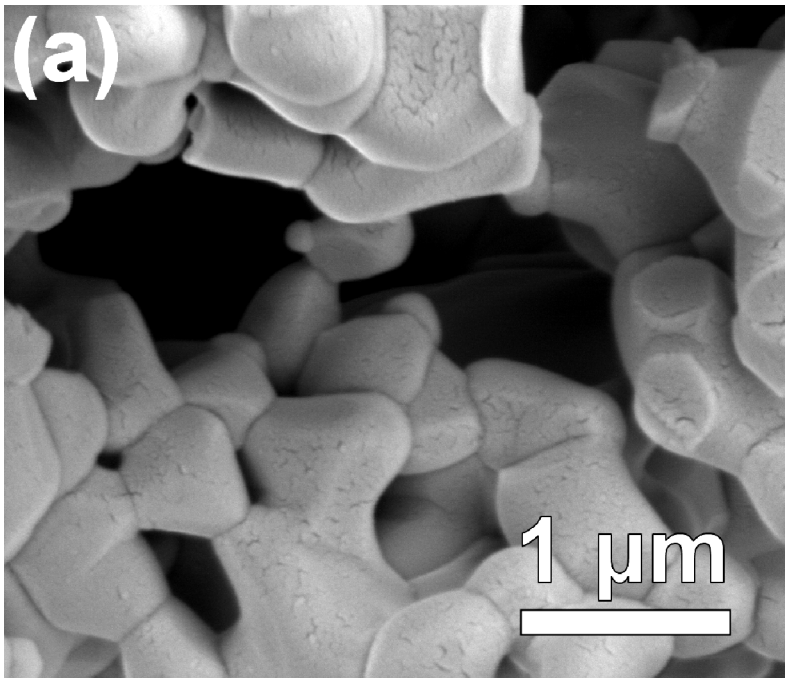

Figure 5.2a The microstructure of the YSZ matrix.

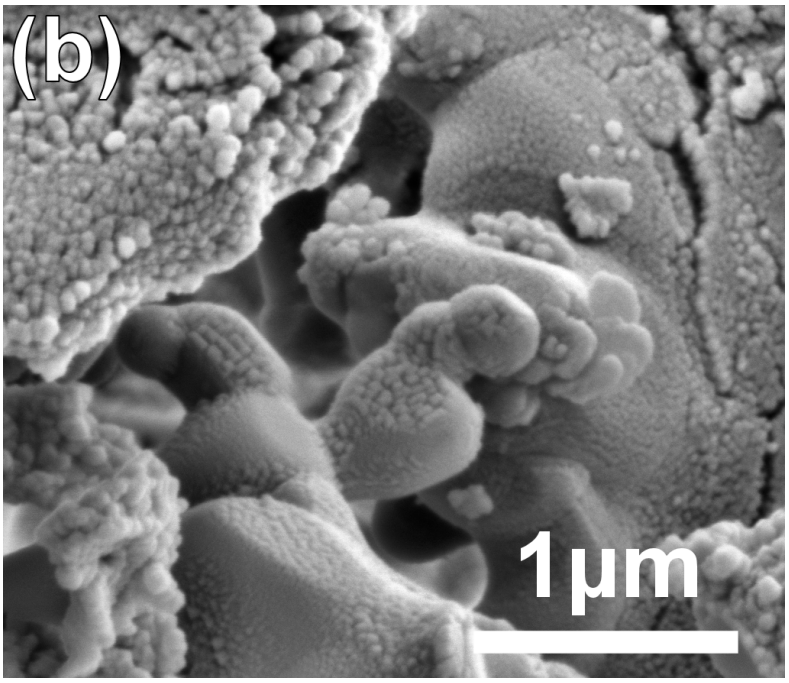

Figure 5.2b The microstructure of the YSZ-SDC composites with 20-wt% SDC fired to 1373 K.

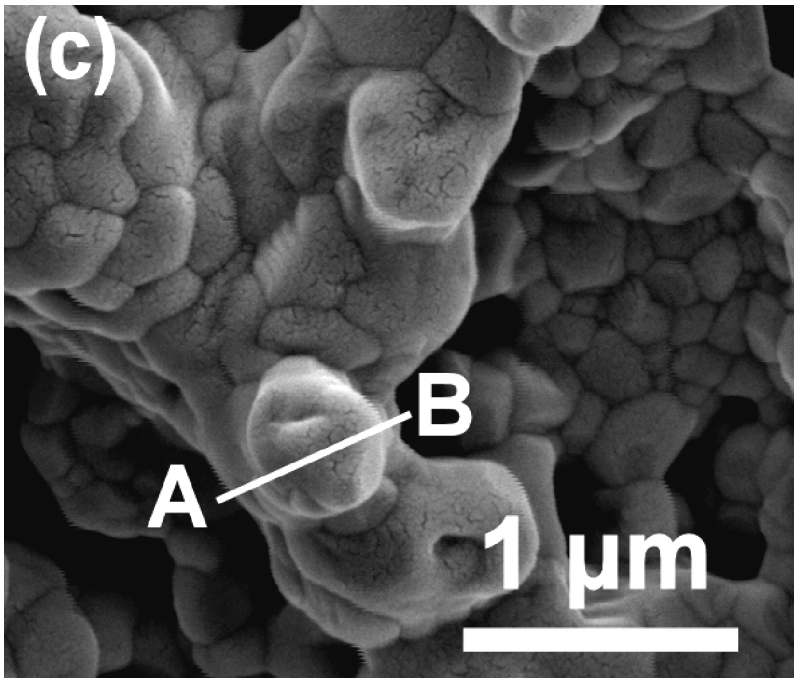

Figure 5.2c The microstructure of the YSZ-SDC composites with 20-wt% SDC fired to 1473 K.

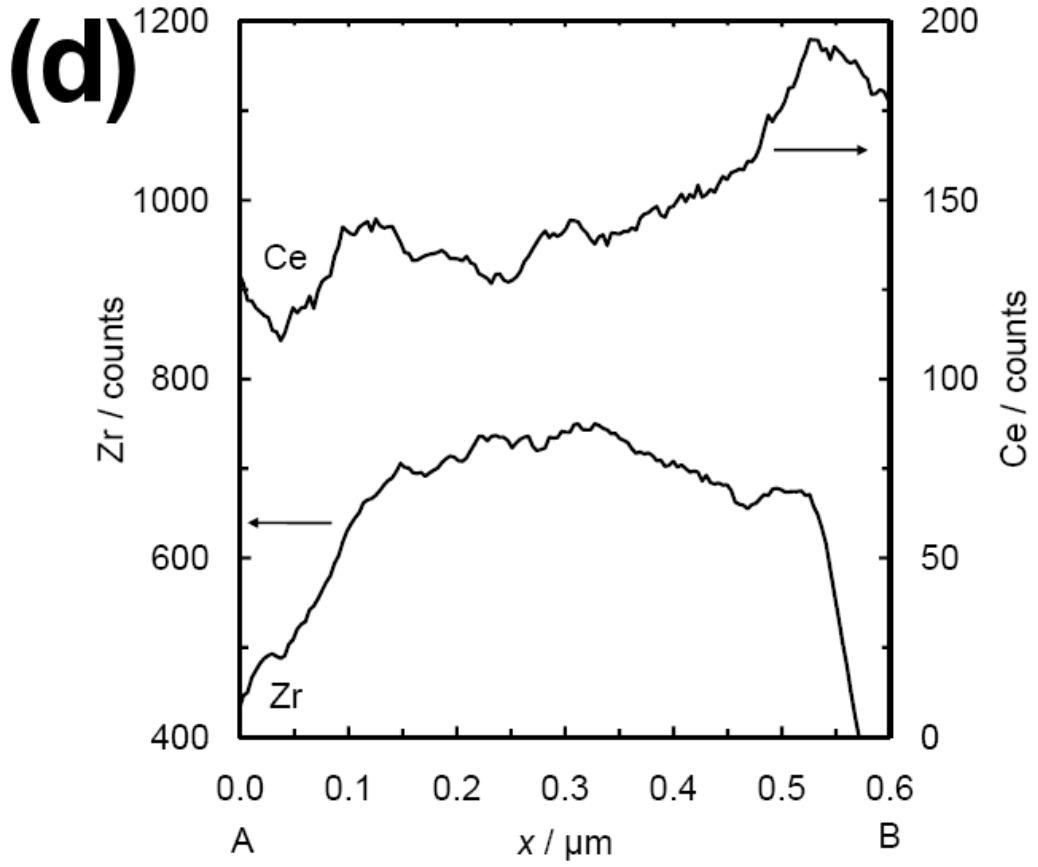

Figure 5.2d The result of an EDX scan along the path A-B in c).

Table 5.1. BET surface areas of an empty YSZ scaffold and 20-wt% SDC in YSZ composite, shown as a function of SDC calcination temperature. The measurements were conducted on 3 × 3 × 10 mm SDC/YSZ slabs.

Sample		S_{BET} / m^2 g^{-1}
Blank YSZ		0.27
SDC-YSZ calcined to	1123 K	1.24
	1273 K	0.57
	1373 K	0.39
	1473 K	0.24
	1573 K	0.21

presence of small SDC particles. Only after calcination to 1473 K did the specific surface area of the SDC-YSZ composite decrease below that of the original YSZ, indicating formation of dense film of SDC over the YSZ. Further heating to 1573 K had a minimal effect on the surface area.

Because SDC can react with YSZ to form solid solutions [31], XRD measurements of 40-wt% (~20-vol%) SDC in YSZ were performed as a function of temperature, as shown in Figure 5.3. There were no changes in the YSZ peaks at 30.17 and 35.12 degrees as the temperature was increased from 973 K to 1473 K, and features associated with SDC at 28.43 and 32.95 degrees simply narrowed due to increasing crystallite size. At 1523 K, there was a shifting of both the SDC and the YSZ peaks because of the formation of solid solutions at the interface. At 1573 K, the extent of the solid-state reaction between SDC and YSZ is such that the XRD pattern is nearly that of a single-phase oxide.

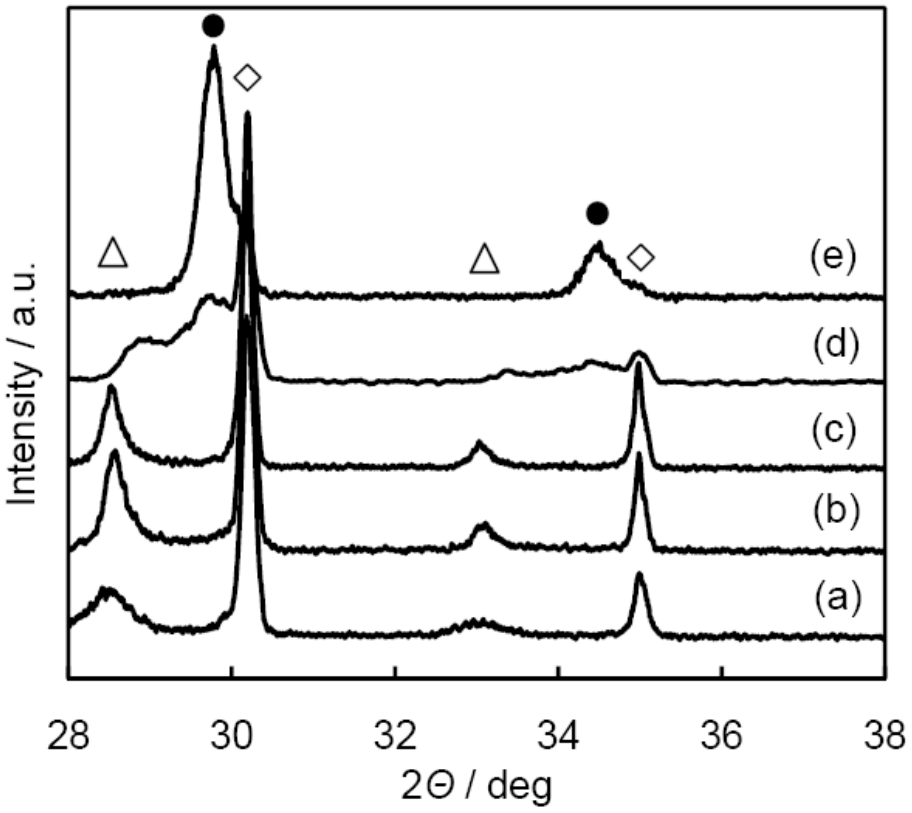

Figure 5.3 XRD patterns of the SDC/YSZ composite calcined to a) 973 K, b) 1373 K, c) 1473 K, d) 1523 K, and e) 1573 K: (◊) YSZ, (Δ) SDC, (●) $Ce_2Zr_3O_{10}$. The measurements were carried out on 3 × 3 × 10 mm SDC/YSZ slabs.

Figure 5.4 summarizes the XRD results obtained following the addition of 20-vol% LSCo into the YSZ scaffold, with varying heat treatments. The patterns in Figures 5.4a) through e) were obtained without an SDC coating, while that in Figure 5.4f) corresponds to a sample in which 20-vol% SDC, calcined at 1473 K, was incorporated into the YSZ scaffold prior to adding LSCo. The pattern in Figure 5.4b, contains a broad peak at 33 degrees 2θ, demonstrating the formation of the perovskite phase after heating to only 973 K. The two underlying peaks, associated with the rhombohedral structure of the LSCo perovskite, are resolved after heating to 1123 K for 4 h, due to improved crystallinity, Figure 5.4c). By 1273 K, the appearance of $La_2Zr_2O_7$ is evident from the peak at 28.59 degrees 2θ. After calcining at 1373 K, the peak corresponding to $La_2Zr_2O_7$ has grown larger and an addition feature at 30.86 degrees 2θ, due to $SrZrO_3$, is observed.

In a previous study of the stability of cathodes formed by infiltration of $La_{0.8}Sr_{0.2}FeO_3$ (LSF) into porous YSZ, it was found that calcination to 1373 K caused similar changes to the cathode as those observed after fuel-cell operation at 973 K for several thousand hours [15]. Assuming that a similar correlation exists between operating time and calcination temperature for the LSCo-YSZ composites, the observation of new phases in the XRD data in Figure 5.4d) and e) implies that LSCo-YSZ electrodes will not be stable. Therefore, in order to prevent solid-state reaction between LSCo and YSZ, we first incorporated 20-vol% SDC into the YSZ, followed by calcination to 1473 K, before again adding 20-vol% LSCo. The diffraction pattern in Figure 5.4f) was obtained from this composite after calcination to 1373 K for 4 h. While overlap of features associated with SDC and $La_2Zr_2O_7$ near 28.5 degrees 2θ prevents us

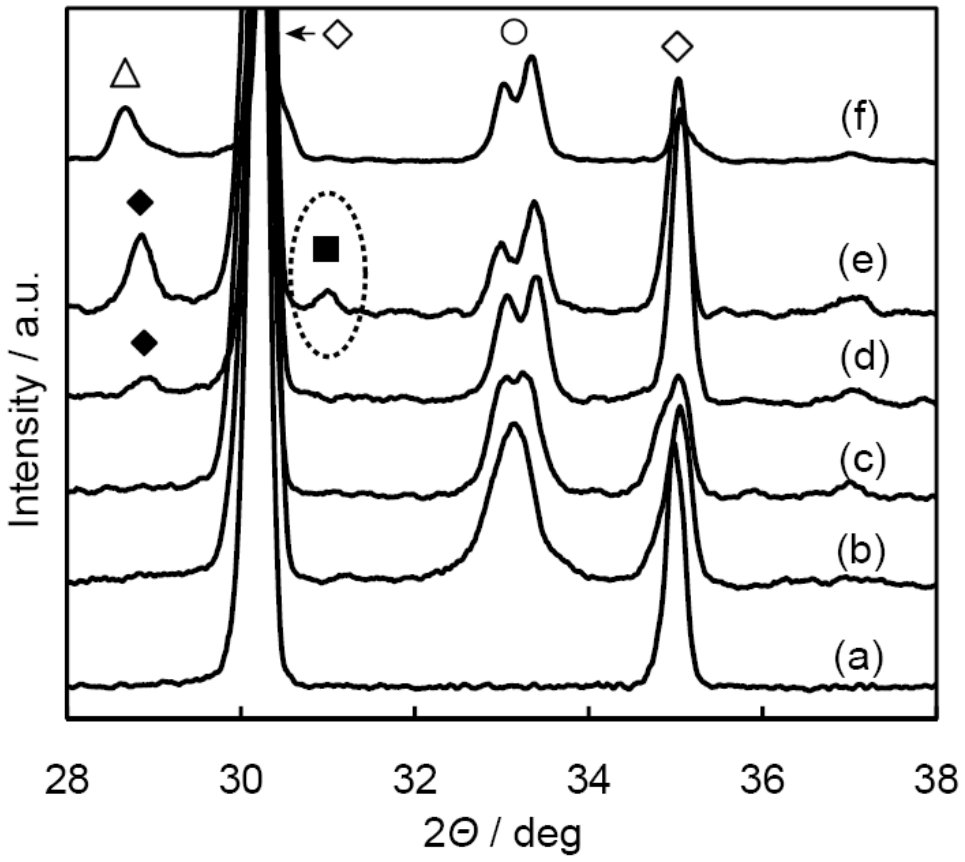

Figure 5.4 XRD patterns of blank YSZ (a), LSCo-YSZ (b-e), and LSCo-SDC/YSZ (f) composites. Calcination temperatures: b) 973 K, c) 1123 K, d) 1273 K, e) and f) both 1373 K. (◊) YSZ, (Δ) SDC, (o) LSCo, (♦) $La_2Zr_2O_7$, (■) $SrZrO_3$.

from seeing whether $La_2Zr_2O_7$ is formed, there is no evidence in the XRD pattern for features corresponding to $SrZrO_3$, suggesting that the SDC layer has prevented the solid-state reactions. It should be noted that slight broadening of the YSZ peaks at 30.17 and 35.12 degrees 2θ can be detected in pattern (f) in Fig. 5.4. This effect is likely to be caused by the onset of a solid state reaction between YSZ and SDC. However, we found samples with SDC layers calcined to either 1373 K or 1573 K to be much less effective in stabilizing the LSCo. SDC layers calcined to 1373 K are not dense enough to provide an effective barrier, while layers fired to 1573 K showed extensive reaction between YSZ and SDC.

Electrode performance and stability are the most important tests of the effectiveness of the SDC layer. To determine the effect of the SDC layer, impedance data were measured at 973 K, using symmetric cells having 20-vol% LSCo, with and without 20-vol% SDC, following calcination at 973 and 1373 K. The impedance data, reported as Cole-Cole plots in Figure 5.5, have all been divided by two to account for the presence of two electrodes. After calcination to 973 K, the performances of both composite electrodes were very good (Figure 5.5a and b). The resistance of an 88-μm YSZ electrolyte at 973 K is calculated to be 0.46 $\Omega \cdot cm^2$ [32], so that the high-frequency intercepts at 0.23 and 0.25 $\Omega \cdot cm^2$ for the cells with and without SDC are close to 50% of the expected resistance of the electrolyte. The non-ohmic losses, ~20 and 30 $m\Omega \cdot cm^2$ for cells with and without SDC, respectively, are also both very good.

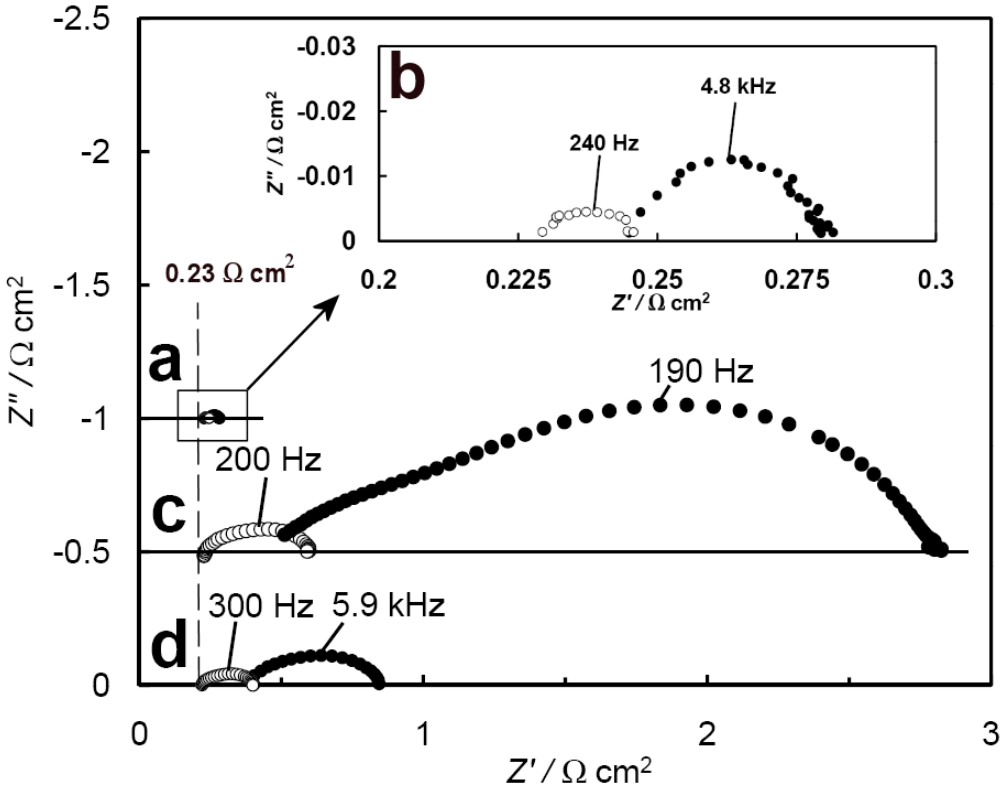

Figure 5.5 Electrochemical impedance results for LSCo-YSZ (filled symbols) and LSCo-SDC/YSZ (open symbols) symmetric cells at 973 K and ambient air conditions. The LSCo calcination temperature was 973 K for a) and b) and 1373 K for c) and d). All measurements were carried out at open circuit conditions, except for d), where a current of 600 mA/cm^2 was applied.

The effect of the SDC layer is clearly seen in the impedances measured on cells that had been calcined to 1373 K (Figure 5.5c). Without SDC, ohmic losses have increased to 0.5 $\Omega \cdot cm^2$ and the non-ohmic losses to 2.3 $\Omega \cdot cm^2$. However, with the SDC layer, the ohmic losses remain unchanged and the non-ohmic losses have increased to a more acceptable value of ~0.3 $\Omega \cdot cm^2$. The reason for the increased impedance in the absence of SDC is almost certainly associated with solid-state reactions that form insulating phases at the LSCo-YSZ interface. With the SDC, we suggest that the increase in impedance is due to coarsening of the perovskite particles, as seen in Figure 5.6, and a subsequent loss in three-phase boundary sites. Previous work on the infiltration of less reactive perovskites also saw increased impedances following higher calcination temperatures that appeared to be due to particle coarsening [33,34]. Studies by Jørgensen *et al*. on LSM/YSZ composite electrodes also support this conclusion [35].

The impedances for the cells that had been calcined to 1373 K overestimate the losses that would be observed during fuel cell operation. As shown in Figure 5.5d, when a current of 600 mA/cm^2 was applied to the symmetric cells, the non-ohmic losses decreased to 0.15 $\Omega \cdot cm^2$ for the cell with SDC and 0.43 $\Omega \cdot cm^2$ for cell without. Although application of a current makes the cells asymmetric, with one electrode operating anodically and the other cathodically, the cathodic impedances of the cells cannot be larger than the sum of the impedances of the two electrodes. Therefore, the electrode impedances for the two cells decrease with current density. This was also observed with LSF-YSZ electrodes calcined to higher temperatures and, again, appears to be due to the coarsening of the perovskite nanoparticles [33,34].

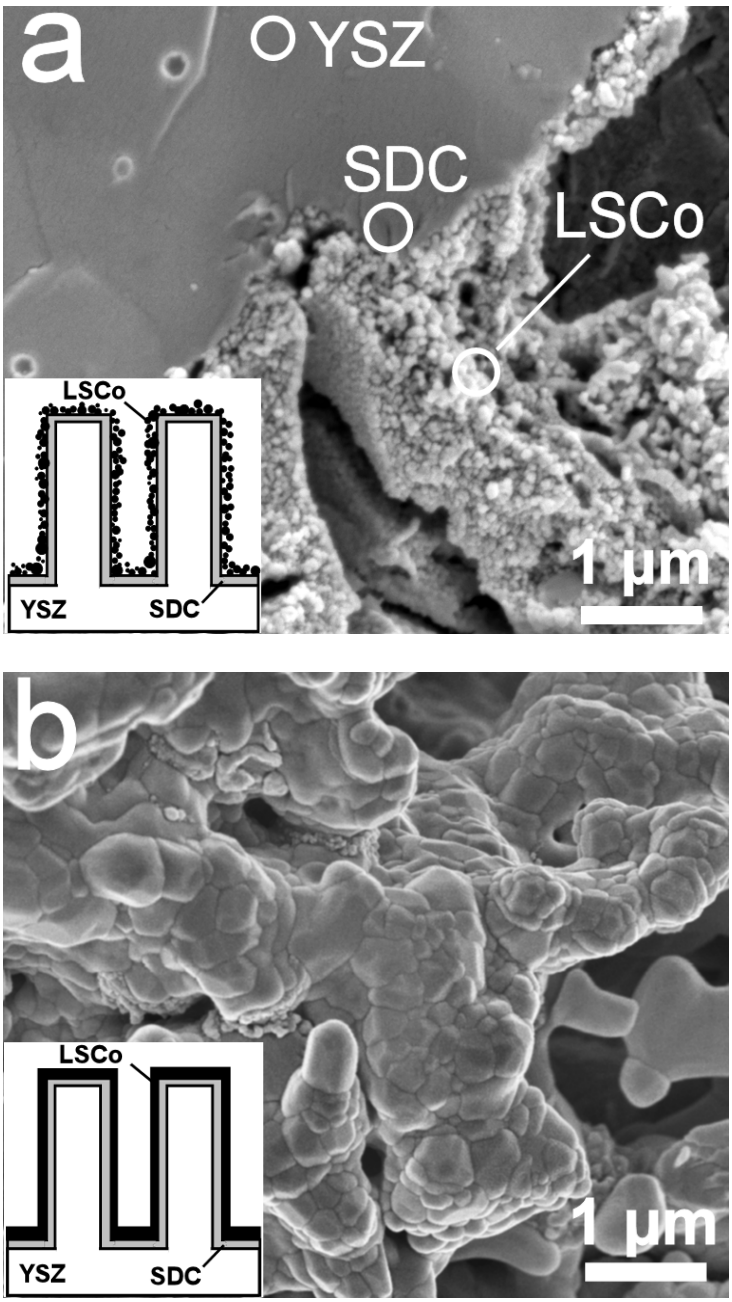

Figure 5.6 SEM images of an LSCo-SDC-YSZ electrode calcined to (a) 973 K, and (b) 1373 K. The composition of point marked with open circles in (a) were determined by EDX.

Although the impedance of the electrode prepared by infiltration of LSCo into a YSZ scaffold with an SDC barrier in this study was good, this can almost certainly be improved. For example, previous work showed that the pore structure of the YSZ scaffold can have a large impact on electrode impedance [6]. We made no attempt to optimize this pore structure in the present investigation. We also did not investigate whether there is an optimal thickness for the SDC layer.

Obviously, the additional steps required for fabricating electrodes by infiltration are a barrier to adopting this procedure, particularly when an SDC film must first be added into the YSZ scaffold to prevent solid-state reactions between the YSZ and the perovskite. However, the present results show that one can use this method to make high-performance electrodes, with good stability, from materials that are not well matched for CTE. The fact that the YSZ scaffold is heated together with the electrolyte to very high temperatures also ensures that these electrodes will adhere well to the electrolyte. Therefore, we believe this approach is worth considering as a method for producing high-performance cathodes.

5.4 Conclusion

The possibility of preparing a samaria doped ceria (SDC) diffusion barrier layer by infiltration methods was investigated. The best results were observed when the SDC was calcined to 1473 K. Both electrode impedances measured on symmetric cells and X-ray diffraction data suggest that such layers are effective in reducing the extent of solid-state reaction between LSCo and YSZ.

5.5 References

1. W. Tanner, K.-Z. Fung, and A. V. Virkar, The effect of porous composite electrode structure on solid oxide fuel cell performance: 1. Theoretical analysis, *J. Electrochem. Soc.,* **144**[1], 21 (1997).
2. J. Mertens, V. A. C. Haanappel, C. Wedershoven, and H.-P. Buchkremer, Sintering behavior of (La, Sr)MnO_3 type cathodes for planar anode-supported SOFCs, *J. Fuel Cell Sci. Technol.,* **3**[4], 415 (2006).
3. H. Uchida, S. Arisaka, and M. Watanabe, High performance electrodes for medium-temperature solid oxide fuel cells: Activation of La(Sr)CoO_3 cathode with highly dispersed Pt metal electrocatalysts, *Solid State Ionics*, **135**, 347 (2000).
4. T. Horita, K. Yamaji, N. Sakai, H. Yokokawa, A. Weber, and E. Ivers-Tiffee, Oxygen reduction mechanism at porous $La_{1-x}Sr_xCoO_{3-\delta}$ cathodes / $La_{0.8}Sr_{0.2}Ga_{0.8}Mg_{0.2}O_{2.8}$ electrolyte interface for solid oxide fuel cells, *Electrochim. Acta*, **46**, 1837 (2001).
5. S. J. Skinner, Recent advances in perovskite-type materials for solid oxide fuel cell cathodes, *Int. J. Inorg. Mater.*, **3**, 113 (2001).
6. Y. Huang, J. M. Vohs, and R. J. Gorte, Characterization of LSM-YSZ composites prepared by impregnation methods, *J. Electrochem. Soc.,* **152**[7] A1347 (2005).
7. R. Küngas, I. Kivi, K. Lust, G. Nurk, and E. Lust, Statistical method to optimize the medium temperature solid oxide fuel cell electrode materials, *J. Electroanal. Chem.*, **629**, 94-101 (2009).

8. J. M. Ralph, C. Rossignol, and R. Kumar, Cathode materials for reduced-temperature SOFCs, *J. Electrochem. Soc.*, **15**, A1518 (2003).
9. S. P. Simner, J. F. Bonnett, N. L. Canfield, K. D. Meinhardt, V. L. Sprenkle, and J. W. Stevenson, Optimized lanthanum ferrite-based cathodes for anode-supported SOFCs, *Electrochem. Solid-State Lett.*, **5**, A173 (2002).
10. S. P. Simner, J. F. Bonnett, N. L. Canfield, K. D. Meinhardt, J. P. Shelton, V. L. Sprenkle, and J. W. Stevenson, Development of lanthanum ferrite SOFC cathodes, *J. Power Sources,* **113**, 1 (2003).
11. S. P. Simner, M. D. Anderson, and J. W. Stevenson, La(Sr)FeO_3 SOFC cathodes with marginal copper doping, *J. Am. Ceram. Soc.*, **87**, 1471 (2004).
12. Y. Huang, J. M. Vohs, and R. J. Gorte, Fabrication of Sr-doped $LaFeO_3$ YSZ composite cathodes, *J. Electrochem. Soc.,* **151**[4], A646 (2004).
13. S. P. Jiang, A comparison of O_2 reduction reactions on porous (La,Sr)MnO_3 and (La,Sr)(Co,Fe)O_3 electrodes, *Solid State Ionics*, **146**, 1 (2002).
14. A. Esquirol, N. P. Brandon, J. A. Kilner, and M. Mogensen, Electrochemical characterization of $La_{0.6}Sr_{0.4}Co_{0.2}Fe_{0.8}O_3$ cathodes for intermediate-temperature SOFCs, *J. Electrochem. Soc.*, **151**, A1847 (2004).
15. W. Wang, M. D. Gross, J. M. Vohs, and R. J. Gorte, The stability of LSF–YSZ electrodes prepared by infiltration, *J. Electrochem. Soc.*, **154**, B439 (2007).
16. J. M. Vohs and R. J. Gorte, High-performance SOFC cathodes prepared by infiltration, *Adv. Mater.*, **21**, 943 (2009).

17. M. D. Gross, J. M. Vohs, and R. J. Gorte, Recent progress in SOFC anodes for direct utilization of hydrocarbons, *J. Mater. Chem*., **17**, 3071 (2007).

18. R. Craciun, S. Park, R. J. Gorte, J. M. Vohs, C. Wang, and W. L. Worrell, A novel method for preparing anode cermets for solid oxide fuel cells, *J. Electrochem. Soc.*, **146**, 4019 (1999).

19. S. P. Jiang, A review of wet impregnation - an alternative method for the fabrication of high performance and nano-structured electrodes of solid oxide fuel cells*, Matls. Sci. & Eng. A*, **418**, 199 (2006).

20. Y. Huang, J. M. Vohs, and R. J. Gorte, SOFC cathodes prepared by infiltration with various LSM precursors, *Electrochem. Solid-State Lett.*, **9**, A237 (2006).

21. H. P. He, Y. Huang, J. Regal, M. Boaro, J. M. Vohs, and R. J. Gorte, Low-temperature fabrication of oxide composites for solid-oxide fuel cells, *J. Am. Ceram. Soc*., **87**, 331 (2004).

22. T. J. Armstrong and J. G. Rich, Anode-supported solid oxide fuel cells with $La_{0.6}Sr_{0.4}CoO_{3-\lambda}$-$Zr_{0.84}Y_{0.16}O_{2-\delta}$ composite cathodes fabricated by an infiltration method, *J. Electrochem. Soc.*, **153**, A515 (2006).

23. M. Sase, D. Ueno, K. Yashiro, A. Kaimai, T. Kawada, and J. Mizusaki, Interfacial reaction and electrochemical properties of dense $(La,Sr)CoO_{3-\delta}$ cathode on YSZ (100), *J. Phys. Chem. Solids*, **66**, 343 (2005).

24. M. Shiono, K. Kobayashi, T. L. Nguyen, K. Hosoda, T. Kato, K. Ota, and M. Dokiya, Effect of CeO_2 interlayer on ZrO_2 electrolyte/$La(Sr)CoO_3$ cathode for low-temperature SOFCs, *Solid State Ionics*, **170**, 1 (2004).

25. C. Rossignol, J.M. Ralph, J.-M. Bae, and J.T. Vaughey, $Ln_{1-x}Sr_xCoO_3$ (Ln=Gd, Pr) as a cathode for intermediate-temperature solid oxide fuel cells, *Solid State Ionics*, **175**, 59 (2004).
26. S. Uhlenbruck, T. Moskalewicz, N. Jordan, H.-J. Penkalla, and H.P. Buchkremer, Element interdiffusion at electrolyte–cathode interfaces in ceramic high-temperature fuel cells, *Solid State Ionics*, **180**, 418 (2009).
27. K. Kammer Hansen, M. Menon, J. Knudsen, N. Bonanos, and M. Mogensen, The effect of a CGO barrier layer on the performance of LSM/YSZ SOFC cathodes, *J. Electrochem. Soc.*, **157**, B309 (2010).
28. S. Park, R. J. Gorte, and J. M. Vohs, Tape cast solid-oxide fuel cells for the direct oxidation of hydrocarbons, *J. Electrochem. Soc.*, **148**, A443 (2001).
29. G. Kim, J. M. Vohs, and R. J. Gorte, Enhanced reducibility of ceria–YSZ composites in solid oxide electrodes, *J. Mater. Chem*., **18**, 2386 (2008).
30. Y. Huang, J. M. Vohs, and R. J. Gorte, Characterization of LSM-YSZ Composites Prepared by Impregnation Methods, *J. Electrochem. Soc.*, **152**, A1347 (2005).
31. G. Kim, M. D. Gross, W. Wang, J. M. Vohs, and R. J. Gorte, SOFC anodes based on LST-YSZ composites and on $Y_{0.04}Ce_{0.48}Zr_{0.48}O_2$, *J. Electrochem. Soc.*, **155**, B360 (2008).
32. K. Sasaki and J. Maier, Re-analysis of defect equilibria and transport parameters in Y_2O_3-stabilized ZrO_2 using EPR and optical relaxation, *Solid State Ionics*, **134**, 303 (2000).

33. S. Lee, M. Bevilacqua, P. Fornasiero, J. M. Vohs, and R. J. Gorte, Solid oxide fuel cell cathodes prepared by infiltration of $LaNi_{0.6}Fe_{0.4}O_3$ and $La_{0.91}Sr_{0.09}Ni_{0.6}Fe_{0.4}O_3$ in porous yttria-stabilized zirconia, *J. Power Sources*, **193**, 747 (2009).
34. F. Bidrawn, G. Kim, N. Aramrueang, J. M. Vohs, and R. J. Gorte, Dopants to enhance SOFC cathodes based on Sr-doped $LaFeO_3$ and $LaMnO_3$, *J. Power Sources*, **195**, 720 (2010).
35. M. J. Jørgensen, S. Primdahl, C. Bagger, and M. Mogensen, Effect of sintering temperature on microstructure and performance of LSM–YSZ composite cathodes, *Solid State Ionics* **139**, 1 (2001).

Chapter 6. Atomic Layer Deposition to Investigate Surface Reactions in SOFC Cathodes Prepared by Infiltration*

Summary

The processes limiting the performance of solid oxide fuel cell (SOFC) were examined for composite cathodes made by infiltrating $La_{0.8}Sr_{0.2}FeO_{3-\delta}$ (LSF) into porous yttria-stabilized zirconia (YSZ). Impedance spectra measured on symmetric cells calcined to 1123 K consisted of a single arc with a polarization resistance of 0.3 Ω cm^2 at 973 K in air. The higher impedance of cells deactivated by calcination to 1373 K could be attributed to an additional low-frequency surface process. The addition of a conformal oxide coating of less than 1 nm in thickness further deactivated the LSF-YSZ cathode. At 873 K, the polarization resistance of Al_2O_3-coated cells increased by almost an order of magnitude. This deactivation was reversible; performance could be restored by a heat treatment that caused the conformal oxide coating to disintegrate.

6.1 Introduction

The mechanism of oxygen reduction on mixed conducting perovskite surfaces has been the subject of numerous experimental and theoretical studies. Recently, a growing number of research groups have been converging on the idea that the kinetics of oxygen reduction on mixed conductors are generally not limited by the diffusion of O^{2-}

* This chapter has been accepted for publication in ECS Transactions, manuscript number MS #B7-0840.

species through the perovskite bulk, but rather by a slow adsorption step occurring on the perovskite surface [1-5].

These results have a number of interesting implications. First, it is implied that maximizing the ionic conductivity of the perovskite used in an SOFC composite cathode may not be necessary, as long as the conductivity exceeds a certain threshold value. The validity of this claim has been verified experimentally for differently doped $LaFeO_3$-YSZ cathodes prepared by infiltration [6].

Secondly, in case a surface reaction is rate-limiting, increasing the surface area of the electrode (e.g. by infiltration of nanoparticles) should result in enhanced performance. This phenomenon has been verified experimentally for many perovskite systems and nanoparticles [7-12]. That small additions of species like Pd, doped and undoped CeO_2, $La_{0.8}Sr_{0.2}FeO_{3-\delta}$ (LSF), and yttria-stabilized zirconia (YSZ) are able to enhance performance is perhaps not surprising. However, similar enhancements have also been observed after the infiltration of CaO and K_2O [12].

Thirdly, the chemical composition of the perovskite surface is likely to play an important role in determining the overall performance of the fuel cell or even an entire multi-kW fuel cell system. It is therefore very important to identify the nature and concentration of catalytically active sites on such surfaces. Recent density functional theory studies have shown that the concentration of oxygen vacancies on the perovskite surface can differ dramatically from the concentration of vacancies in the bulk [13,14]. For example, for an ideal MnO_2-terminated $La_{0.9}Sr_{0.1}MnO_{3-\delta}$ surface, the concentration of vacancies should be 6 orders of magnitude higher than that in the bulk [14]. In

contrast, secondary ion mass spectrometry (SIMS) measurements on quenched perovskite single crystals suggest that a vacancy depletion region may exist on the surface instead [15].

In this chapter, we have taken one step further in the study of surface reaction limited SOFC electrodes. By measuring the impedance response of symmetric cells under different oxygen partial pressures, we have first elucidated the conditions under which composite electrodes made by infiltrating LSF into YSZ are surface-limited. We then used atomic layer deposition (ALD) to coat the perovskite active surface with thin layers of an insulating oxide. Our results indicate that the LSF surface is extremely sensitive towards impurities.

6.2 Experimental

All of the electrochemical measurements in this study were performed on symmetric cells in which the electrodes were prepared by infiltration of nitrate solutions into a porous electrolyte matrix. The first step in cell fabrication involved making a porous-dense-porous structure of the electrolyte using tape-casting methods. The tapes for the porous YSZ were prepared by mixing 8 mol.% YSZ powder (Tosoh), a solvent mixture (ethanol+xylenes), dispersant (Menhaden Fish Oil), binder (PVB B98), plasticizers (benzyl butyl phthalate and polyethylene glycole), and the pore former (graphite and rice starch in a weight ratio of 1:2). A detailed description of the tape-casting and lamination procedure is available elsewhere [16,17]. The resulting slurry was tape cast and laminated onto both sides of a dense YSZ green tape. After sintering at

1773 K for 4 hours, the resulting YSZ matrix was approximately 65-70% porous and had a surface area of 0.48 m^2/g. The thickness of the sintered porous YSZ electrodes was ≈ 40 μm.

$La_{0.8}Sr_{0.2}FeO_3$ was introduced by infiltrating the electrolyte scaffolds with an aqueous solution consisting of $La(NO_3)_3 \cdot 6H_2O$, $Sr(NO_3)_2$, and $Fe(NO_3)_3 \cdot 9H_2O$ at a molar ratio of La:Sr:Fe = 0.8:0.2:1. Citric acid, in a 1:1 ratio with the metal cations, was used as a complexing agent in order to assist the formation of the perovskite phase at lower temperatures. Infiltration steps were followed by a 0.5-h heat treatment at 723 K to decompose the nitrates. This procedure was repeated until a loading of 35-wt% LSF was achieved. The composites were then calcined to either 1123 K or to 1373 K for 4 hours.

In some cases, the electrodes were subject to Al_2O_3 treatment in an atomic layer deposition (ALD) setup (Savannah 200, Cambridge Nanotech). Conformal coatings of Al_2O_3 were deposited into the porous LSF-YSZ electrodes using alternating exposures to water and trimethylaluminum (TMA). The reactants were maintained at room temperature, resulting in vapor pressures of about 20 Torr and 11 Torr inside the sample containers, respectively [18]. The deposition chamber was maintained at 150°C and at a base pressure of 0.08 Torr in a N_2 flow of 5 ml/min. Each deposition cycle consisted of the following steps: 1) purge chamber with N_2 for 10 s 2) stop N_2 flow, 3) pulse water for 15 ms, 4) wait 25 s to achieve uniform coverage throughout the porous sample, 5) purge chamber with N_2 for 10 s, 6) stop N_2 flow, 7) pulse TMA for 15 ms, 8) wait 25 s. Increasing the duration of steps 4 and 8 to 50 s did not affect the amount deposited per

cycle, suggesting that 25 s reaction time was enough to achieve uniform deposition throughout the porous LSF-YSZ electrode.

The amount of oxide deposited was quantified by gravimetry. For this, a pellet was made from LSF powder, synthesized from the same nitrate/citric acid solution that was used for infiltration and heated to 973 K for 4 hours, by pressing the powder into thin disks of about 1 mm in thickness. The disks were then further calcined to 1123 K for 4 hours. It was assumed that the surface composition of LSF in the pellet was identical to LSF infiltrated into YSZ and heated to the same temperature for the same amount of time. The specific surface area of each pellet was determined by Brunauer-Emmett-Teller Kr adsorption measurements at 77 K using a setup described elsewhere [19]. The weight change after a known number of deposition cycles was converted to a corresponding Al_2O_3 surface coverage.

Electrochemical impedance spectra of symmetric LSF-YSZ-LSF cells were recorded using a Gamry Instruments potentiostat in the frequency range of 0.01 Hz to 300 kHz. All symmetric cell impedances in this paper have been divided by two to account for there being two identical electrodes. The effect of oxygen partial pressure on electrode performance was studied by mixing O_2 (99.8%, Airgas) and N_2 (99.999%, Airgas) in desired ratios. Ambient air and 5% O_2 in Ar mixture (Airgas) were used as reference for $p(O_2)$ = 0.21 atm and $p(O_2)$ = 0.05 atm. The sample was allowed to equilibrate for 15 minutes in each atmosphere before impedance measurements were conducted.

6.3 Results and discussion

6.3.1 Surface limitation in LSF-YSZ cathodes

LSF infiltrated into YSZ is a good model system for studying the effect of perovskite surface area on the electrochemical properties of the electrode. LSF does not react with YSZ even above 1373 K [20,21], which allows us to simulate degradation and change the perovskite microstructure by simply varying the calcination temperature of the electrode after infiltration [9,20,22,23]. Furthermore, since the porous YSZ has been heated to 1773 K prior to infiltration, the microstructure of the electrolyte scaffold will be unaffected by subsequent heat treatments to lower temperatures and any changes in the performance can be attributed to changes in the LSF phase alone.

After calcination to 1123 K, the microstructure of the perovskite is very fine with an average particle size of about 50 nm [9]. An SEM image of such a structure is shown in Fig. 6.1a. The regions in the image without fine particles correspond to the YSZ fracture surface. In contrast, the microstructure of the same electrode after calcination to 1373 K is shown in Fig. 6.1b. As a result of the heat treatment, the perovskite particle size has increased dramatically and the LSF phase is coating the underlying YSZ in the form of a thin dense film.

Figure 6.2 summarizes the electrochemical properties of the electrodes shown above. The ohmic resistance of both cells is about 0.25 Ω cm^2 at 973 K, which agrees well with the theoretical ohmic resistance of a 50 μm YSZ (The thickness of the electrolyte was ≈ 100 μm, but the impedance values in Fig. 6.2 have been divided by two to account for there being two electrodes.). The ohmic resistance was identical for both

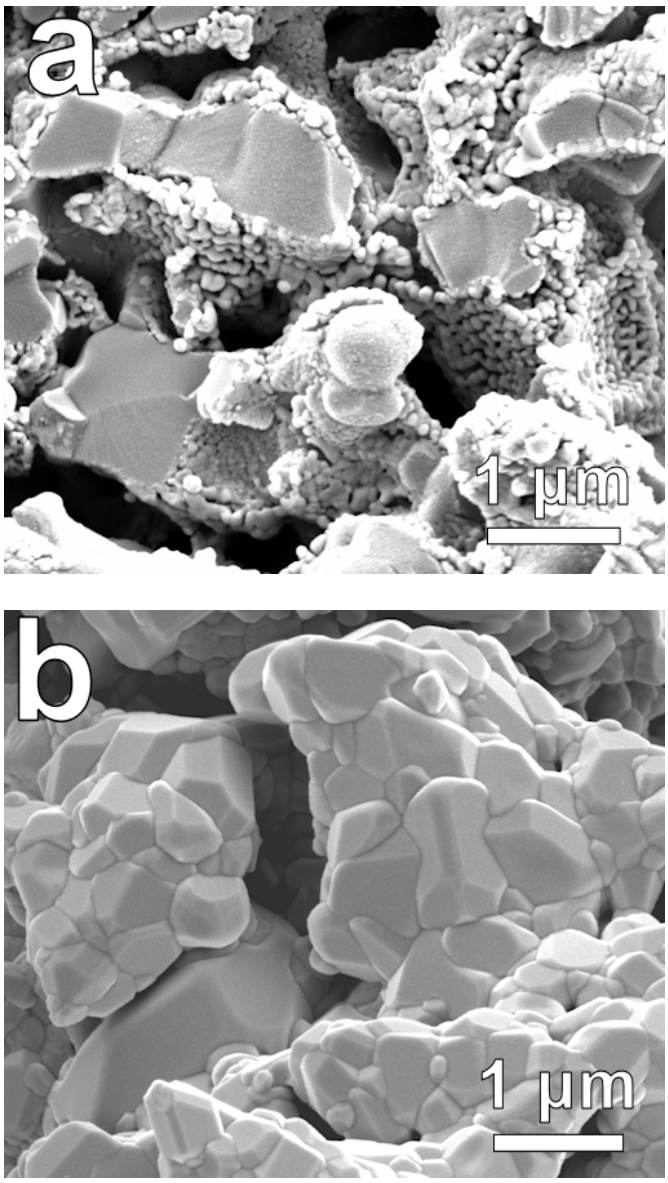

Figure 6.1 Scanning electron microscopy images of LSF-YSZ electrodes prepared by infiltration after calcination to (a) 1123 K and (b) 1373 K.

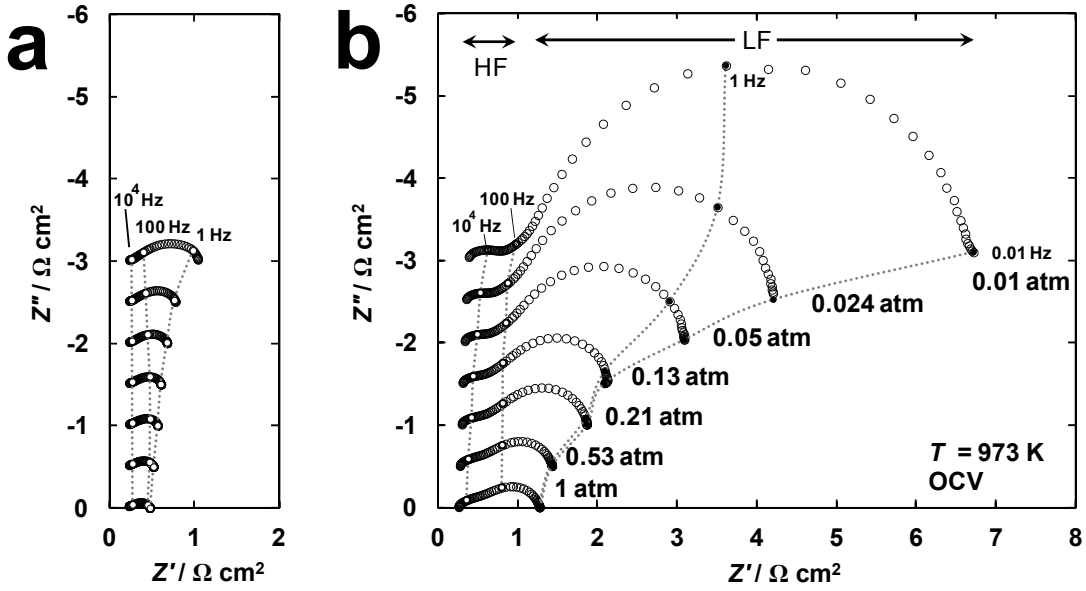

Figure 6.2 Nyquist plots of LSF-YSZ cathode symmetric cells measured at 973 K and open circuit conditions as a function of oxygen partial pressure: (a) LSF-YSZ calcined to 1123 K, (b) LSF-YSZ calcined to 1373 K. The impedance spectra have been offset for clarity. The spectra in (a) were measured at the same $p(O_2)$ as in (b).

1123 K and 1373 K cell, consistent with there being no solid-state reactions between the LSF and YSZ phases. The ohmic resistance the cell heated to 1123 K did not show any changes with changing $p(O_2)$. The ohmic resistance of the cell heated to 1373 K increased slightly at lower oxygen partial pressures, suggesting possible changes in the conductivity of the LSF phase.

By comparing the polarization resistance of the symmetric cells presented in Fig. 6.2, it becomes apparent that the perovskite microstructure plays a crucial role in determining the electrode performance. The total impedance of the cell shown in Fig. 6.1b was almost 2 Ω cm^2, whereas that of the cell shown in Fig. 6.1a was just 0.57 Ω cm^2 at 973 K in ambient air. The impedance of the deactivated cell is dominated by the large polarization resistance, which accounts for almost 85% of the overall impedance. When the oxygen concentration in the gas mixture is lowered to 1%, polarization resistance accounts for over 94% of all losses.

The shape of the impedance spectra changes dramatically with increasing calcination temperature. The spectra for the cell that was heated to 1123 K consist of a single semicircle with a characteristic frequency of 150 Hz ($p(O_2)$ = 0.21 atm). The shapes of the spectra remain unchanged over a wide range of oxygen partial pressures. Only at very low oxygen partial pressures, i.e. $p(O_2) < 0.05$ atm, may an additional process affect the impedance response (Fig 6.2a). The corresponding changes in the performance of the cell calcined to 1373 K are much more dramatic. A low frequency (LF) process is present and accounts for most of the impedance, especially at low oxygen partial pressures. A smaller, high frequency (HF) process is also present (Fig. 6.2b) [24].

Figure 6.3 plots the impedance of the three processes as a function of the oxygen partial pressure on a log-log scale. The LF process observed for the deactivated cell stands out from the rest with a strong $p(O_2)^{-0.43}$ dependence. A $p(O_2)$ dependence close to ½ suggests that the reaction step involves the dissociation of molecular, i.e. gas-phase oxygen into atomic oxygen [5,25]. Thus, the LF process is likely to be a slow process occurring on the surface of the perovskite.

The $p(O_2)$ dependence of the HF process of the deactivated cell is very similar to that of the low-temperature calcination cell (Fig. 6.3). The impedance values are of the same order of magnitude and both processes exhibit a weaker, approximately $p(O_2)^{-0.20}$ dependence (exact values $p(O_2)^{-0.22}$ for 1373 K, HF and $p(O_2)^{-0.17}$ for 1123 K cell). The nature of this process is more difficult to determine from the oxygen partial pressure dependence alone [26].

The same LSF-YSZ cells were also tested under a current load of 100 mA/cm^2. The results are summarized in Figure 6.4. Only the data under 5% O_2 in argon is shown, but the results are representative of cell performance under all $p(O_2)$ conditions. For LSF heated to 1123 K, the impedance arcs remain completely unchanged upon the application of current (Fig. 6.4a). Similarly, no changes can be observed in the magnitude and shape of the arc corresponding to the high-frequency process of the deactivated cell (Fig. 6.4b). The only strongly current dependent process is the low-frequency process of the 1373 K cell, suggesting the latter process may also involve charge transfer.

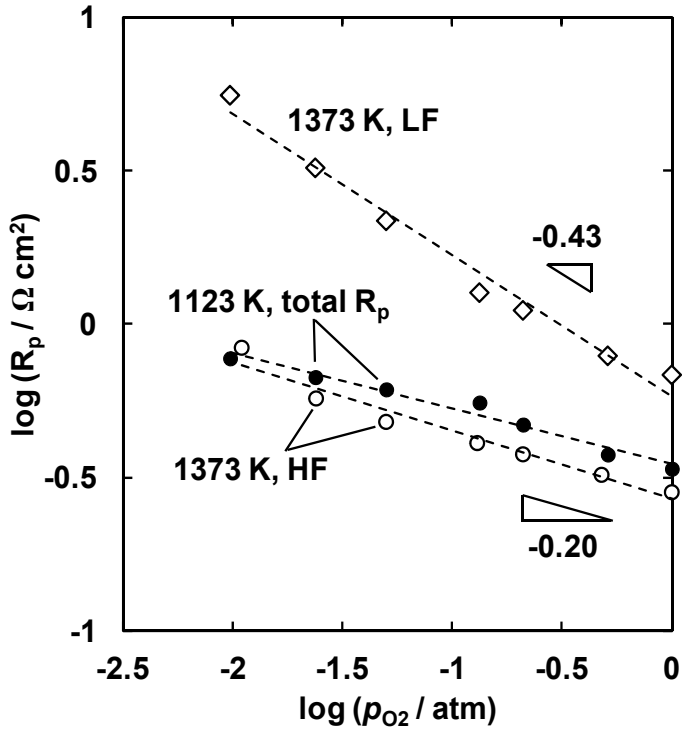

Figure 6.3 Oxygen partial pressure dependence of processes in the impedance spectra of LSF-YSZ electrodes at 973 K: (•) total polarization resistance of a cell heated to 1123 K, (o) high-frequency (HF) polarization resistance of a cell heated to 1373 K, and (◊) low-frequency (LF) polarization resistance of a cell heated to 1373 K.

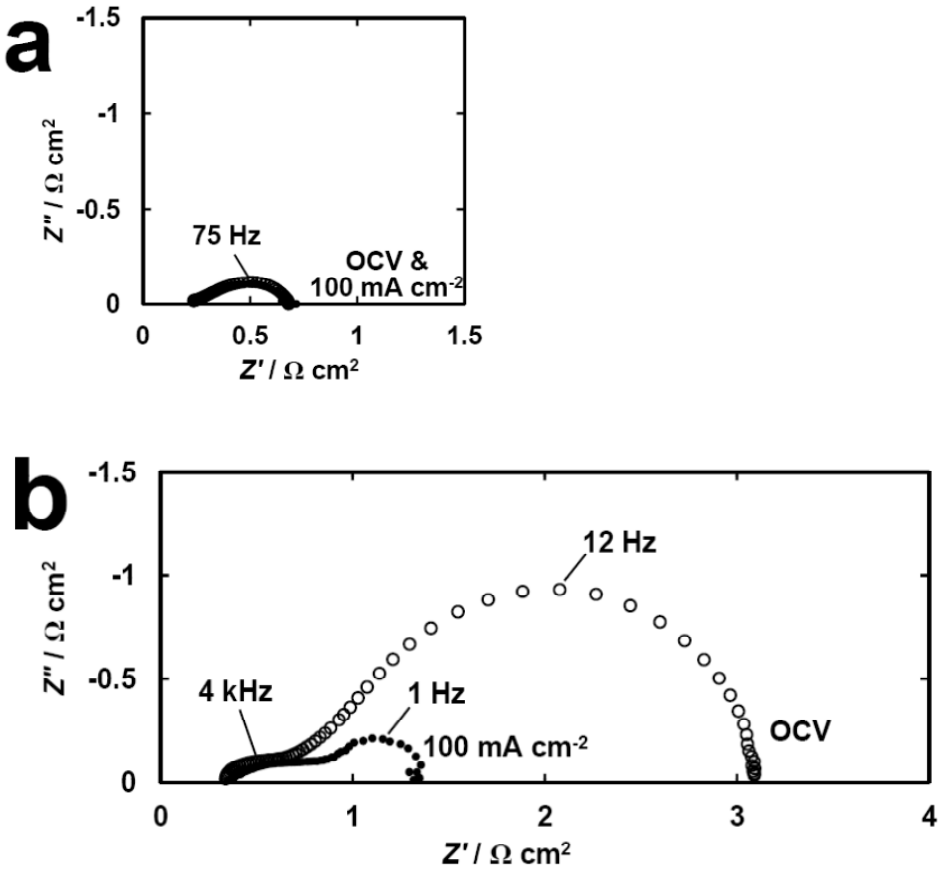

Figure 6.4 Nyquist plots of LSF-YSZ cathode symmetric cells measured at 973 K in 5% O_2 in argon as a function of applied current density: (a) LSF-YSZ calcined to 1123 K, (b) LSF-YSZ calcined to 1373 K.

6.3.2 Effect of sub-nanometer oxide coatings to electrode performance

Summarizing the findings from Fig. 6.2-4, the main difference in the performance of fresh and deactivated LSF-YSZ electrodes arises from a slow surface process that involves both gas-phase oxygen and charge transfer. A thorough understanding of the factors that result in surface limitation is therefore needed in order to prevent performance degradation in these systems.

ALD is a sequential chemical vapor deposition (CVD) technique where evaporated precursors are alternatively pulsed into the deposition chamber, allowing the deposition of one atomic layer after another of conformal, homogeneous (sub-) nanometer thin films [18,27-29]. In contrast to traditional CVD, reactions in ALD are self-terminating, i.e. once the precursor has reacted with the substrate surface, further deposition is impossible. The self-terminating nature of ALD provides an exceptionally high level of control over the thickness of the deposited layers, even when deposition is carried out in a porous medium.

Al_2O_3 deposition with TMA and water is probably the most well-known and thoroughly characterized ALD process [18,29]. The reaction between TMA and the substrate is rapid and works well on a large number of different substrates [29]. In this study, we used TMA/water ALD to study the effect of modifying the surface of the perovskite with extremely thin (< 1 nm) oxide films. We did this in order to investigate the sensitivity of LSF-YSZ electrodes to changes in the surface composition of LSF. Note that the use of model electrodes with simplified geometry was not necessary due to the self-terminating nature of ALD.

LSF-YSZ composite electrodes heat-treated to 1123 K were first prepared and tested. Good reproducibility was observed from cell to cell (Fig. 6.5a and 6.5b, black symbols). After testing, the silver current collectors were carefully removed and the same cells were subject to a TMA/water treatment (see Experimental section). After *n* depositions (*n* = 1, 2, 5, 10), the electrochemical performance of each cell was again tested at 873 K and 973 K. The corresponding impedance plots are also shown in Fig. 6.5 (open symbols). The addition of Al_2O_3 was found to have an adverse effect to cell performance in all cases studied. The observed effect was most dramatic at 873 K (Fig. 6.5a). Electrodes that had previously demonstrated excellent polarization resistances of about 0.7 Ω cm^2 had now non-ohmic impedances of 1.12 Ω cm^2 (1 cycle of Al_2O_3), 2.50 Ω cm^2 (2 cycles of Al_2O_3), 4.18 Ω cm^2 (5 cycles of Al_2O_3), and 6.01 Ω cm^2 (10 cycles of Al_2O_3) at 873 K. The increase in polarization resistance for the electrode with 10 ALD cycles was thus almost tenfold.

The thickness of Al_2O_3 deposited in a single cycle was 0.24 Å (equivalent to just 1.1 Al atoms / nm^2 or about $^1/_{11}$ of a monolayer), based on calibration experiments with pressed LSF pellets. In other words, even the thickest coatings reported here were less than 1 monolayer thick. These results demonstrate clearly how sensitive SOFC electrodes are to surface-poisoning. If the Al_2O_3 film is assumed to cover the LSF, the extent of deactivation is similar to what one would expect for geometric covering of the exposed surface.

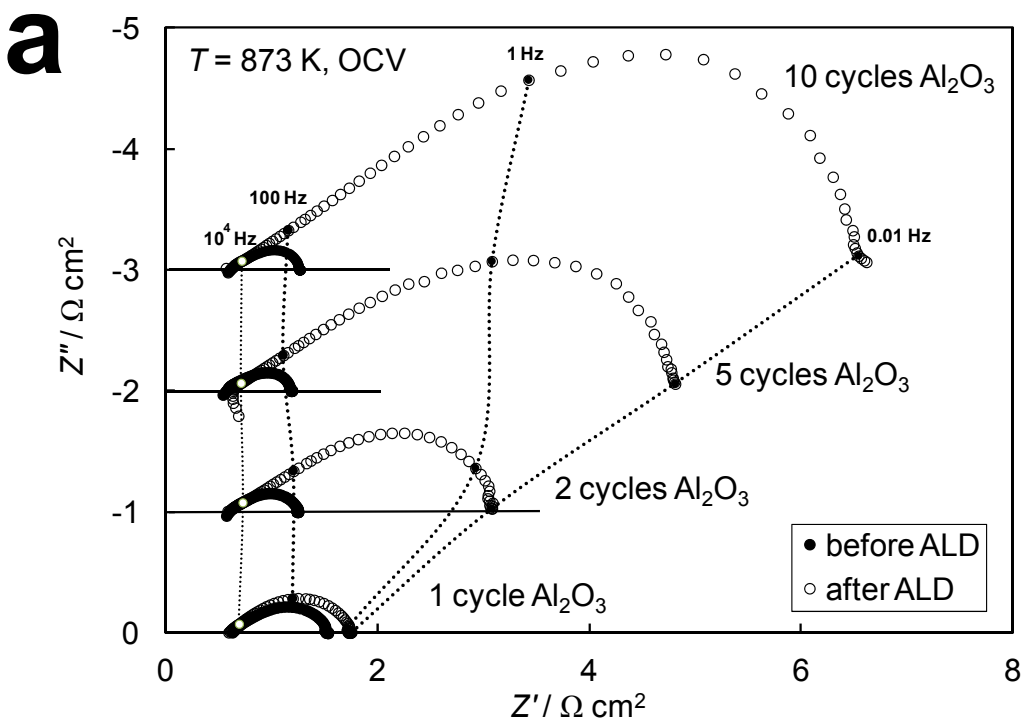

Figure 6.5a Nyquist plots of four LSF-YSZ cathode symmetric cells calcined to 1123 K and measured at 873 K before and after ALD treatment. The impedance spectra have been offset for clarity.

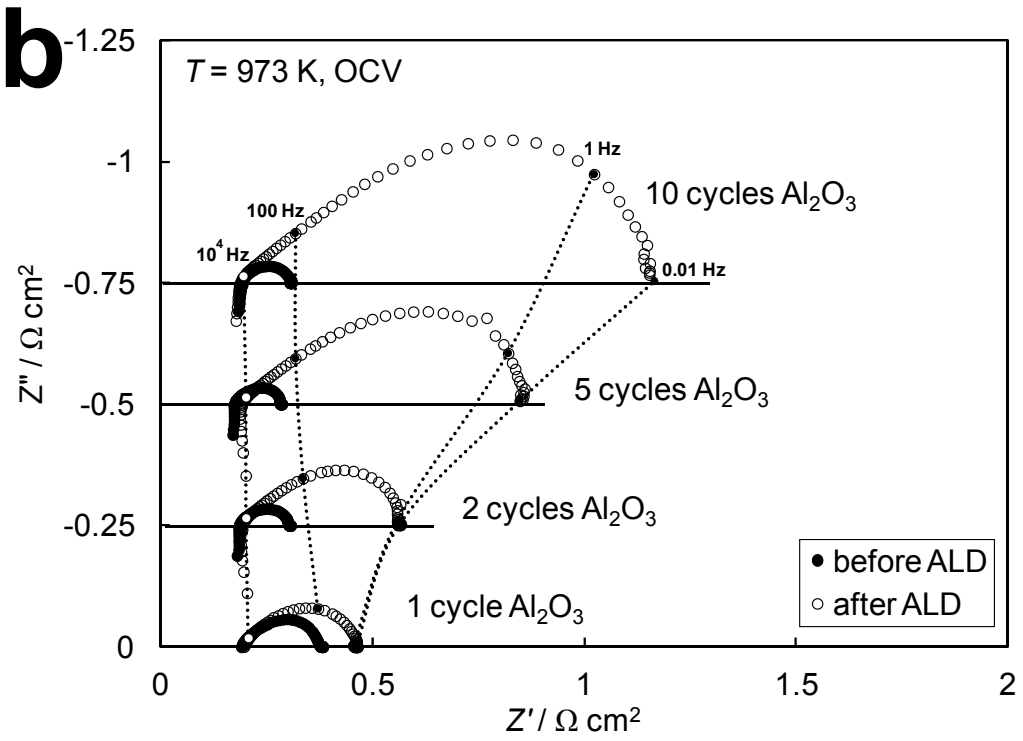

Figure 6.5b Nyquist plots of four LSF-YSZ cathode symmetric cells calcined to 1123 K and measured at 973 K before and after ALD treatment. The impedance spectra have been offset for clarity.

Similar, but slightly less pronounced effect is observable at 973 K (Fig. 6.5b). We attribute the smaller effect to the breaking-up of the initially conformal alumina coating due to thermally induced mechanical stresses. Indeed, the impedance of the four cells shown in Fig. 6.5 was very similar in magnitude when tested at 1073 K. Furthermore, the resistance decreased substantially after the electrodes were cooled back down to 973 K (Fig. 6.6).

The temperatures at which deposition and subsequent characterization was carried out are too low to result in any degree of Al_2O_3 incorporation into the bulk of the perovskite phase, and therefore, the alumina can only affect processes occurring on the immediate surface of LSF. Furthermore, the shape of impedance spectra of Fig. 6.5 and 6.6 is very similar to these shown in Fig. 6.2 for the thermally deactivated cell. We suggest that the ALD experiments verify our prior assignment of the low-frequency process in Fig. 6.2 to a slow surface process. We further propose the use of ALD as a sensitive method to investigate surface-limited performance in SOFC electrodes in general.

6.4 Conclusion

LSF-YSZ electrodes prepared by infiltration were coated with sub-nanometer layers of conformal Al_2O_3 using atomic layer deposition (ALD). Electrochemical impedance spectroscopy measurements conducted before and after ALD demonstrate the sensitivity of SOFC electrodes to surface-poisoning. Even a fraction of a monolayer of Al_2O_3 on LSF was found to have an adverse effect on cell performance.

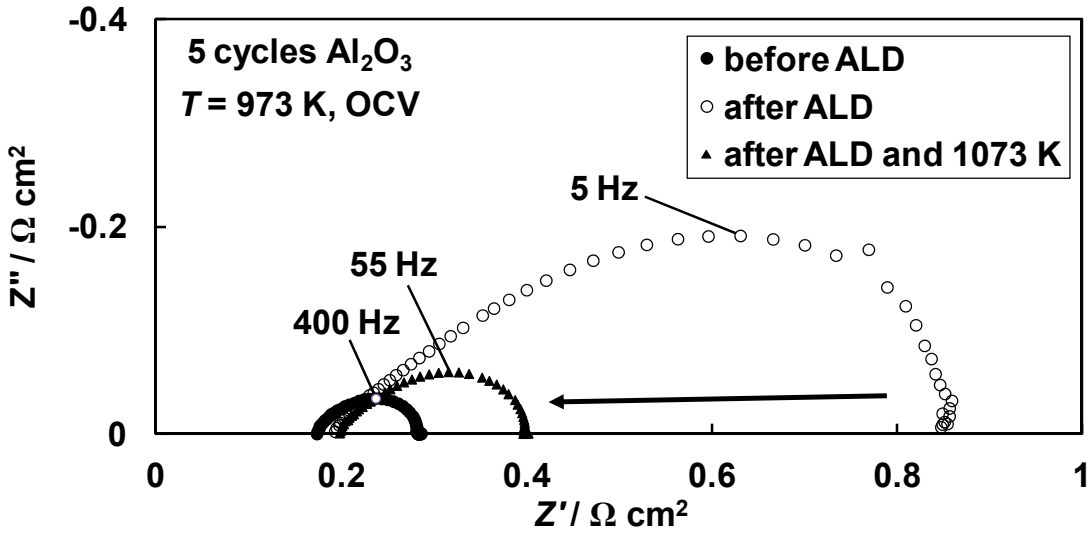

Figure 6.6 Nyquist plots of LSF-YSZ cathode symmetric cells calcined to 1123 K tested at 973 K before and after a 5-cycle Al_2O_3 ALD. Performance is partly restored after the ALD layer disintegrates at 1073 K.

The results obtained after ALD treatment agree well with the oxygen partial pressure experiments, suggesting that surface deactivation of LSF is the main cause of degradation in LSF-YSZ electrodes.

6.5 References

1. H. J. M. Bouwmeester, C. Song, J. Zhu, J. Yi, M. van Sint Annaland, and B. A. Boukamp, A novel pulse isotopic exchange technique for rapid determination of the oxygen surface exchange rate of oxide ion conductors, *Phys. Chem. Chem. Phys.*, **11**, 9640 (2009).
2. E. N. Armstrong, K. L. Duncan, D. J. Oh, J. F. Weaver, and E. D. Wachsman, Determination of surface exchange coefficients of LSM, LSCF, YSZ, GDC constituent materials in composite SOFC cathodes, *J. Electrochem. Soc.*, **158**[5], B492 (2011).
3. S. B. Adler, Mechanism and kinetics of oxygen reduction on porous $La_{1-x}Sr_xCoO_{3-\delta}$ electrodes, *Solid State Ionics*, **111**, 125 (1998).
4. F. Bidrawn, R. Küngas, J. M. Vohs, and R. J. Gorte, Modeling impedance response of SOFC cathodes prepared by infiltration, *J. Electrochem. Soc.*, **158**[5], B514 (2011).
5. M. Mosleh, M. Søgaard, and P. V. Hendriksen, Kinetics and mechanisms of oxygen surface exchange on $La_{0.6}Sr_{0.4}FeO_{3-\delta}$ thin films, *J. Electrochem. Soc.,* **156**[4], B441 (2009).

6. F. Bidrawn, S. Lee, J. M. Vohs, and R. J. Gorte, The effect of Ca, Sr, and Ba doping on the ionic conductivity and cathode performance of $LaFeO_3$, *J. Electrochem. Soc.,* **155**[7], B660 (2008).
7. F. Bidrawn, G. Kim, N. Aramrueang, J. M. Vohs, and R. J. Gorte, Dopants to enhance SOFC cathodes based on Sr-doped $LaFeO_3$ and $LaMnO_3$, *J. Power Sources*, **195**, 720 (2010).
8. Na Ai, S. P. Jiang, Z. Lü, K. Chen, and W. Su, Nanostructured $(Ba,Sr)(Co,Fe)O_{3-\delta}$ impregnated $(La,Sr)MnO_3$ cathode for intermediate-temperature solid oxide fuel cells, *J. Electrochem. Soc.* **157**[7], B1033 (2010).
9. R. Küngas, F. Bidrawn, E. Mahmoud, J. M. Vohs, and R. J. Gorte, *Solid State Ionics*, accepted.
10. T. Z. Sholklapper, C. P. Jacobson, S. J. Visco, and L. C. De Jonghe, Synthesis of dispersed and contiguous nanoparticles in solid oxide fuel cell electrodes, *Fuel Cells,* **8**[5], 303 (2008).
11. C. Knöfel, H.-J. Wang, K. T. S. Thydén, and M. Mogensen, Modifications of interface chemistry of LSM–YSZ composite by ceria nanoparticles, *Solid State Ionics*, **195**, 36 (2011).
12. M. Mogensen, M. Søgaard, P. Blennow, and K. Kammer Hansen, The action of SOFC nano-particles, Proceedings of the 8th European SOFC Forum, Lucerne, Switzerland, 6 p. (2008).

13. Y.-L. Lee, J. Kleis, J. Rossmeisl, and D. Morgan, *Ab initio* energetics of $LaBO_3$(001) (B=Mn, Fe, Co, and Ni) for solid oxide fuel cell cathodes, *Phys. Rev. B*, **80**, 224101 (2009).

14. Y.-L. Lee and D. Morgan, Prediction of surface oxygen vacancy concentrations of $(La_{1-x}Sr_x)MnO_3$, *ECS Trans*., **25** (2) , 2769 (2009).

15. R. A. De Souza, J. Zehnpfennig, M. Martin, and J. Maier, Determining oxygen isotope profiles in oxides with Time-of-Flight SIMS, *Solid State Ionics*, **176**, 1465 (2005).

16. J. M. Vohs and R. J. Gorte, High-performance SOFC cathodes prepared by infiltration, *Adv. Mater*., **21**, 943 (2009).

17. R. Küngas, J.-S. Kim, J. M. Vohs, and R. J. Gorte, Restructuring porous YSZ by treatment in hydrofluoric acid for use in SOFC cathodes, *J. Am. Ceram. Soc*, **94**[7], 2220 (2011).

18. R. A. Wind and S. M. George, Quartz crystal microbalance studies of Al_2O_3 atomic layer deposition using trimethylaluminum and water at 125 °C, *J. Phys. Chem. A*, **114**, 1281 (2010).

19. D. Wang, Y. Kang, V. Doan-Nguyen, J. Chen, R. Küngas, N. Wieder, K. Bakhmutsky, R. J. Gorte, and C. B. Murray, Synthesis and oxygen storage capacity of two-dimensional ceria nanocrystals, *Angew. Chem*., **50** (19) 4378 (2011).

20. W. Wang, M. D. Gross, J. M. Vohs, and R. J. Gorte, The stability of LSF–YSZ electrodes prepared by infiltration, *J. Electrochem. Soc.*, **154**, B439 (2007).

21. L. Adijanto, R. Küngas, F. Bidrawn, R. J. Gorte, and J. M. Vohs, Stability and performance of infiltrated $La_{0.8}Sr_{0.2}Co_xFe_{1-x}O_3$ electrodes with and without $Sm_{0.2}Ce_{0.8}O_{1.9}$ interlayers, *J. Power Sources*, **196**, 5797 (2011).
22. R. Küngas, F. Bidrawn, J. M. Vohs, and R. J. Gorte, Doped-ceria diffusion barriers prepared by infiltration for solid oxide fuel cells, *Electrochem. Solid-State Lett.*, **13**, B87 (2010).
23. R. Küngas, J. M. Vohs, and R. J. Gorte, Effect of ionic conductivity of the electrolyte in composite SOFC cathodes, *J. Electrochem. Soc*, **158**[6], B743 (2011).
24. Additional processes may be present but the characteristic frequencies of these processes are too similar to allow physically meaningful deconvolution.
25. Y. Takeda, R. Kanno, M. Noda, Y. Tomida, and O. Yamamoto, Cathodic polarization phenomena of perovskite oxide electrodes with stabilized zirconia , *J. Electrochem. Soc.*, **134** (11), 2656 (1987).
26. J. Fleig, R. Merkle, and J. Maier, The $p(O_2)$ dependence of oxygen surface coverage and exchange current density of mixed conducting oxide electrodes: model considerations, *Phys. Chem. Chem. Phys*., **9**, 2713 (2007).
27. T. Suntola, Atomic layer epitaxy, *Thin Solid Films*, **216**, 84 (1992).
28. M. Cassir, A. Ringuedé, and L. Niinistö, Input of atomic layer deposition for solid oxide fuel cell applications, *J. Mater. Chem.*, **20**, 8987 (2010).
29. R. L. Puurunen, Surface chemistry of atomic layer deposition: A case study for the trimethylaluminum/water process, *J. Appl. Phys.*, **97**, 121301 (2005).

Chapter 7. Conclusions

In this thesis, the effect of a number of microstructural and materials properties affecting the performance of solid oxide fuel cell (SOFC) composite cathodes was studied in a systematic manner. All studies were conducted on electrodes prepared by infiltration of the perovskite active phase into an ionically conducting porous electrolyte matrix. Compared to traditional cell preparation techniques, the infiltration approach gives superior control over the electrode microstructure, allowing one to study the effect of a single parameter at a time. As a result, the role of some material properties, which had so far remained elusive (due to conflicting reports in the literature), could be determined. Pictorial summary of the factors studied is presented in Figure 7.1.

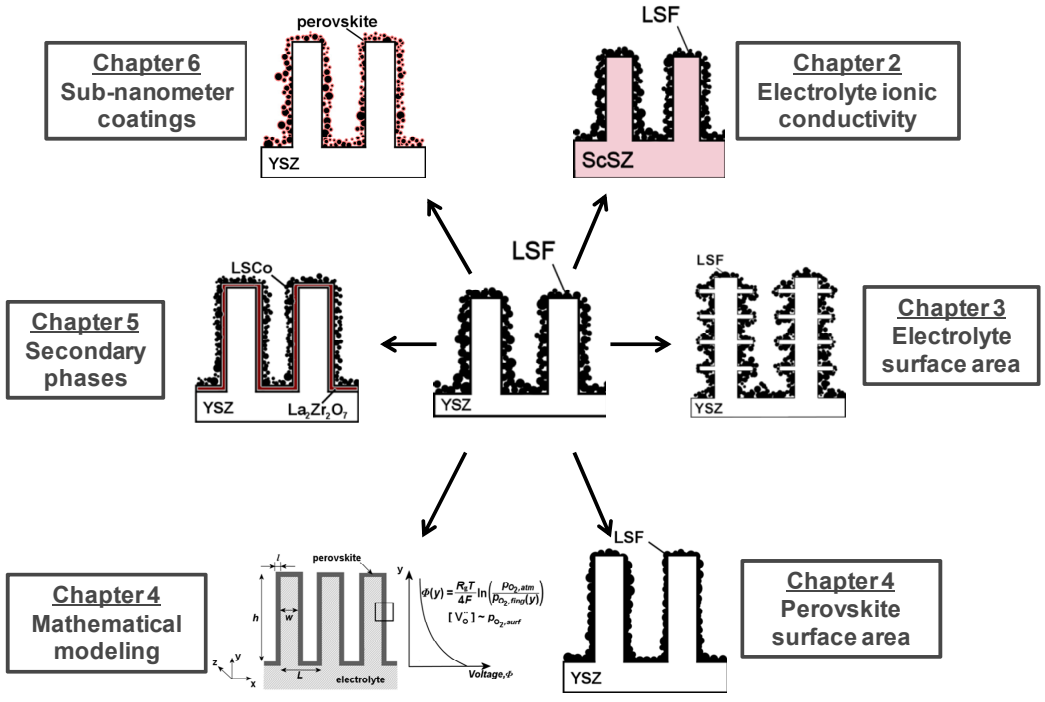

Figure 7.1 Infiltration method as an analytical platform: the microstructural and materials properties studied in this thesis.

In Chapter 2, SOFC cathodes were prepared by infiltration of 35-wt% $La_{0.8}Sr_{0.2}FeO_3$ (LSF) into porous scaffolds of three, zirconia-based electrolytes in order to determine the effect of the ionic conductivity of the electrolyte material on cathode impedances. The electrolyte scaffolds were 10 mol.% Sc_2O_3-stabilized zirconia (ScSZ), 8 mol.% Y_2O_3-stabilized zirconia (YSZ), and 3 mol.% Y_2O_3, 20 mol.% Al_2O_3-codoped zirconia (YAZ), prepared by tape casting with graphite pore formers. The electrode impedances decreased with increasing electrolyte conductivity, with the dependence being between to the power of 0.5 and 1.0, depending on the operating temperature and LSF calcination temperature.

In Chapter 3, the structure of porous YSZ was modified either by infiltration with concentrated hydrofluoric acid or by pore formers of different size. HF treatment resulted in the dissolution and precipitation of the YSZ, resulting in greatly increased surface area of the porous YSZ. Electrodes made by infiltration of 35- wt% LSF into the HF-treated pore structure exhibited significantly lower impedances than untreated electrodes. Additionally, the cathodes with a finer YSZ microstructure were found to be less prone to degradation.

The goal of Chapter 4 was to draw attention to the relationship between the surface area of the perovskite phase in the electrode and the corresponding electrochemical performance. The impedance of cathodes prepared by infiltration of LSF into porous YSZ depended strongly on the surface area of the perovskite phase and was found to be independent of LSF film thickness. The results suggest that the performance of infiltrated, composite electrodes is limited by a slow surface process (O_2 adsorption

and incorporation into the perovskite). Experimental results agreed well with the predictions of a mathematical model, also introduced in Chapter 4.

In Chapter 5, the chemical stability of highly active $La_{0.8}Sr_{0.2}CoO_3$ (LSCo) cathodes was investigated. Undesirable solid-state reactions between LSCo and YSZ could be prevented by application of a dense coating of Sm-doped ceria (SDC), infiltrated into the YSZ pores using aqueous solutions of $Sm(NO_3)_3$ and $Ce(NO_3)_3$, and calcined to 1473 K. LSCo-SDC/YSZ electrodes exhibited very low cathode impedances, ~20 mΩ cm^2 at 973 K, with acceptable degradation after heating to 1373 K.

In the last chapter of the thesis, the impedance of LSF-YSZ electrodes was studied as a function of oxygen partial pressure, $p(O_2)$. Electrodes calcined to 1023 K demonstrated only a weak $p(O_2)$ dependence, with the impedance spectra consisting of a single arc with a polarization resistance of 0.3 Ω cm^2 at 973 K in air. The higher impedance of cells deactivated by calcination to 1373 K could be attributed to an additional low-frequency surface process, which was found to be highly affected by both $p(O_2)$ as well as polarization. The addition of a conformal Al_2O_3 coating of less than 1 nm in thickness using atomic layer deposition (ALD) was also found to deactivate the LSF-YSZ cathode, resulting in increased impedances associated with the low-frequency surface process. At 873 K, the polarization resistance of Al_2O_3-coated cells increased by almost an order of magnitude. This deactivation was reversible; performance could be restored by a heat treatment that caused the conformal oxide coating to disintegrate.